

A parallel-kinetic-perpendicular-moment model for magnetised plasmas

James Juno¹ , Ammar Hakim¹  and Jason M. TenBarge² 

¹Princeton Plasma Physics Laboratory, Princeton, NJ 08543, USA

²Department of Astrophysical Sciences, Princeton University, Princeton, NJ 08544, USA

Corresponding author: James Juno, jjuno@pppl.gov

(Received 4 May 2025; revision received 24 June 2025; accepted 8 July 2025)

We describe a new model for the study of weakly collisional, magnetised plasmas derived from exploiting the separation of the dynamics parallel and perpendicular to the magnetic field. This unique system of equations retains the particle dynamics parallel to the magnetic field while approximating the perpendicular dynamics through a spectral expansion in the perpendicular degrees of freedom, analogous to moment-based fluid approaches. In so doing, a hybrid approach is obtained that is computationally efficient enough to allow for larger-scale modelling of plasma systems while eliminating a source of difficulty in deriving fluid equations applicable to magnetised plasmas. We connect this system of equations to historical asymptotic models and discuss advantages and disadvantages of this approach, including the extension of this parallel-kinetic-perpendicular moment beyond the typical region of validity of these more traditional asymptotic models. This paper forms the first of a multi-part series on this new model, covering the theory and derivation, alongside demonstration benchmarks of this approach that include shocks and magnetic reconnection.

Key words: plasma simulation, astrophysical plasmas, space plasma physics

1. Introduction

Many plasma systems are observed to be in two distinct parameter regimes, which can have profound impacts on the dynamics of these plasmas: weakly collisional and magnetised. In astrophysical systems, plasmas are routinely observed to have plasma densities and temperatures that imply the collisional mean free path is large, while the measured or inferred magnetic field strengths imply the particle gyroradius is small. Across a diverse array of astrophysical environments, such as accretion disks around black holes (Quataert 2001; The Event Horizon Telescope Collaboration *et al.* 2019*a,b*, 2021), plasma-filled pulsar magnetospheres (Philippov & Kramer 2022), the hotter phases of the interstellar (Cox 2005; Humphrey *et al.* 2011), circumgalactic (Tumlinson, Peebles & Werk 2017), intergalactic (Nicastro *et al.* 2005) and intracluster media (Fabian 1994; Peterson & Fabian 2006; Kunz, Jones & Zhuravleva 2022), or the inner (Marsch 2006; Borovsky & Valdivia 2018)

and outer heliosphere (Richardson *et al.* 2022), low collisionality, highly magnetised plasmas can be found. Closer to home, a variety of terrestrial plasmas, such as the plasmas confined by diverse fusion reactor concepts (Spitzer 1958; Furth 1975; Wesson 2011; Imbert-Gerard, Paul & Wright 2020), are constructed to be in this parameter regime in which the effects of particle collisions happen on longer time scales and larger length scales than the dynamics of the particles gyrating around the magnetic field.

When the collisional mean free path is large and the particle gyroradius is small, the plasma will adjust its dynamics such that motion parallel to the magnetic field is uninhibited compared with motion perpendicular to the magnetic field. In effect, the plasma has an easier time transporting momentum and heat parallel to the local magnetic field while the transport perpendicular to the field is more tightly constrained. The particles can traverse large distances before collisions deflect their trajectories off field lines, while the particle motion perpendicular to the field is mostly limited to the combination of cyclotron motion as the particle gyrates about the local magnetic field and a set of bulk, fluid, drifts that arise due to the local geometry of the magnetic field, such as the magnetic field curvature (Northrop 1961, 1963).

This dichotomy between parallel and perpendicular motion has further dramatic impacts on the plasma's dynamics. In general, the plasma can develop different temperatures parallel and perpendicular to the magnetic field as a result of these distinct motions parallel and perpendicular to the magnetic field (Gary *et al.* 2001; Kasper, Lazarus & Gary 2002; Hellinger *et al.* 2006; Schekochihin & Cowley 2006; Bale *et al.* 2009; Chen *et al.* 2016), and a zoo of micro-scale instabilities can be launched that further modify the plasma's dynamics (Schekochihin *et al.* 2008; Rosin *et al.* 2011; Kunz, Schekochihin & Stone 2014), causing viscous stresses (Kunz, Stone & Quataert 2016; Melville, Schekochihin & Kunz 2016; Squire *et al.* 2019; Kempfski *et al.* 2019; St-Onge *et al.* 2020; Squire *et al.* 2023) and limiting thermal conduction (Riquelme, Quataert & Verscharen 2016; Komarov *et al.* 2016; Roberg-Clark *et al.* 2016, 2018; Komarov *et al.* 2018). Thus, a proper accounting of this separation between parallel and perpendicular dynamics is required for an accurate treatment of the transport of momentum and heat in many plasma systems.

On one hand, modelling these weakly collisional, magnetised plasmas can be achieved in a straightforward manner with kinetic models that solve the Boltzmann, or Vlasov, equation for the particle dynamics in a six-dimensional phase space. However, phase-space dynamics are computationally demanding due to both the high-dimensionality of the equation system and the multiscale nature of kinetic plasma dynamics, which often require a computational model to resolve very small length scales and very fast time scales for stability of the scheme. On the other hand, one can attempt to incorporate the modified parallel versus perpendicular dynamics in hydrodynamic models. While extensions of magnetohydrodynamics to include pressure anisotropy and parallel heat conduction are possible (Chew, Goldberger & Low 1956; Braginskii 1965), these approaches suffer from the difficulty all fluid modelling must address: the development of a proper closure that truncates the number of equations being solved and provides an accurate approximation of the dynamics in the higher moments (Grad 1949). An accurate treatment of the feedback of micro-scale instabilities on the pressure anisotropy and parallel heat conduction is particularly challenging, and more rigorous fluid models may be computationally prohibitive in their own right due to approximations of these dynamics leading to 'non-local' models of the fast parallel transport along the magnetic field (Hammett & Perkins 1990; Hammett, Dorland & Perkins 1992; Snyder,

Hammett & Dorland 1997; Ramos 2003, 2005) or require some sort of artificial limiting of the instabilities in their feedback on the plasma (Sharma *et al.* 2006).

It is the purpose of this study to demonstrate an alternative approach to previous modelling efforts that exploits the dichotomy between parallel and perpendicular dynamics to construct a new hybrid system of equations, one which remains kinetic parallel to the magnetic field, while reducing the dynamics perpendicular to the field in a fluid-like hierarchy. This new parallel-kinetic-perpendicular-moment (PKPM) model has natural connections to a variety of historical asymptotic approaches, including Kulsrud's kinetic magnetohydrodynamics (KMHD) (Kulsrud 1964, 1983) and the work of Ramos on finite Larmor radius (FLR) corrections to drift kinetics (Ramos 2008, 2016). But, while the connection to these approaches that leverage the magnetised nature of the plasma will be made apparent, we emphasise now that our model is not an asymptotic one involving an expansion in a small parameter or parameters, and instead shares a similar construction to recent work in spectral decompositions of the kinetic equation (Delzanno 2015; Parker & Dellar 2015; Vencels *et al.* 2016; Roytershteyn & Delzanno 2018; Koshkarov *et al.* 2021; Pagliantini *et al.* 2023; Issan *et al.* 2024), especially approaches that combine spectral expansions in a subset of the velocity degrees of freedom (Schween & Reville 2024; Schween, Schulze & Reville 2025). In particular, the PKPM model performs a spectral expansion of the distribution function in the perpendicular degrees of freedom, reducing the six-dimensional Vlasov equation to a set of four-dimensional equations. The exact number of four-dimensional equations is set by the desired physics fidelity perpendicular to the magnetic field.

This reduction of the dynamics perpendicular to the field from the spectral expansion gives two key benefits. Firstly, in many magnetised plasma environments, the plasma remains mostly gyrotropic as the plasma evolves (see, e.g. Marsch *et al.* 1982; Marsch 2006). If the plasma remains gyrotropic, the distribution function may be well approximated by a small number of spectral coefficients in the perpendicular degrees of freedom, so that significant computational gains can be realised by reducing the six-dimensional Vlasov equation to just a few four-dimensional kinetic equations. Of course, a magnetised plasma can develop a certain amount of agyrotropy due to cyclotron resonances and other FLR effects, but the framework in which a plasma is gyrotropic with agyrotropic corrections is the exact framework in which spectral expansions excel. There have been a number of demonstrations of spectral decompositions achieving high accuracy with coarse resolution in cases when the deviations from, e.g. a Maxwellian using a Hermite expansion, are small (Roytershteyn *et al.* 2019; Vega *et al.* 2023), and spectral decompositions are quickly becoming one of the most efficient ways to solve classic asymptotic models of magnetised plasma dynamics such as gyrokinetics as applied to the tokamak core (Mandell, Dorland & Landreman 2018; Frei *et al.* 2023*a,b*; Hoffmann *et al.* 2023*a,b*; Mandell *et al.* 2024) and edge (Frei *et al.* 2020, 2024).

Secondly, in cases where we expect such spectral expansions to fail, such as the presence of sharp gradients in phase space, we can instead choose a different numerical method designed to handle complex phase-space structures because we have specifically derived the PKPM model to only expand the distribution function in the perpendicular degrees of freedom. In particular, parallel to the magnetic field we can expect the plasma to develop a variety of non-trivial phase-space structures that are typically difficult to represent numerically with a spectral basis such as trapped-passing boundaries, beams and power-law tails, but which can be easily handled with previous developments in discontinuous Galerkin (DG) methods for kinetic

equations (Juno *et al.* 2018; Hakim & Juno 2020; Mandell *et al.* 2020). Of course, these sorts of phase-space structures can arise perpendicular to the magnetic field, such as the loss cone in the perpendicular degrees of freedom of a magnetic mirror, but these kinetic structures are so ubiquitous parallel to the local magnetic field, from field-aligned beams in collisionless shocks to parallel energisation mechanisms in collisionless magnetic reconnection, we are well motivated to take a hybrid approach that can resolve the plasma's evolution in phase space with as few degrees of freedom as possible. Thus, the reduction in resolution requirements perpendicular to the field, combined with a numerical method optimised to handle the plasma's phase-space dynamics parallel to the field, generates a unique, computationally efficient model for describing a diverse array of plasmas in weakly collisional, magnetised regimes.

The rest of the paper is organised as follows. In § 2 we detail the necessary prerequisites for understanding the PKPM derivation, including a discussion of spectral expansions and coordinate transformation, and difficulties typically encountered when constructing spectral expansions that motivate the particular form of the PKPM model. In § 4 we derive the PKPM model through a series of coordinate transformations, first to the local fluid flow frame and then to a coordinate system aligned with the local magnetic field, followed by a spectral expansion in the perpendicular degrees of freedom. We discuss a number of historical connections in § 5 and attempt to contextualise the physics content of the PKPM model in comparison to other models applied to weakly collisional, magnetised plasmas while also drawing attention to unique features of the model compared with asymptotic models and other approaches that leverage spectral expansions of the kinetic equation. Most importantly, the principal goal of § 5 is to give context to the reader for why the PKPM model has been formulated the way it has been: a model that contains the same physics as many of the historical magnetised, collisionless plasma models, but which ameliorates many numerical difficulties that prevented easily solving some of these models with a computer, in addition to other breakthroughs in the spectral expansion formulation, such as the inclusion of the normalisation of the perpendicular spectral coefficients without the need for auxiliary equations. We then give a brief demonstration of the model in § 6 with test cases beyond the regime of applicability for traditional asymptotic, magnetised plasma models, including a parallel, electrostatic collisionless shock and moderate guide-field magnetic reconnection. Finally, we conclude the discussion of the theory of the PKPM model in § 7.

This paper forms the first of a multi-part series, with the principal focus of this paper being the motivation, theory, properties and historical context of this new system of equations. We defer an in-depth description of the numerical discretisation of the PKPM model to a future paper, both to keep focus on the details of the continuous system of equations and its properties, and because of the complexities that arise in the discrete system to maintain the properties of the continuous system of equations.

2. Preliminaries on spectral expansions and coordinate transformations

Consider the non-relativistic Vlasov equation,

$$\frac{\partial f}{\partial t} + \mathbf{v} \cdot \nabla_{\mathbf{x}} f + \frac{q}{m} (\mathbf{E} + \mathbf{v} \times \mathbf{B}) \cdot \nabla_{\mathbf{v}} f = C[f], \quad (2.1)$$

where $f = f(\mathbf{x}, \mathbf{v}, t)$ is the particle distribution function for the plasma species, q and m are the charge and mass of the plasma species, respectively, $\mathbf{E} = \mathbf{E}(\mathbf{x}, t)$ and

$\mathbf{B} = \mathbf{B}(\mathbf{x}, t)$ are the electric and magnetic fields, respectively, and $C[f]$ is a general operator for modelling discrete particle effects, such as inter-particle collisions.¹ Combined with Maxwell's equations, the Vlasov–Maxwell system of equations provides a near first-principles description of the vast majority of plasma systems in the universe. However, this equation system is a formidable nonlinear system of equations in a six-dimensional, position-velocity, phase space, and direct modelling of this equation system not only requires handling the high-dimensional nature of the Vlasov equation, but also the vast array of spatial and temporal scales contained in said equation. Thus, there is a long history of exploring reductions and simplification to the Vlasov equation, both analytically and numerically, to make the study of plasmas more tractable.

One approach to constructing such approximations to the Vlasov equation is to assume that the solutions are a small deviation from some symmetry or near symmetry. For example, in a highly collisional plasma where the effects of $C[f]$ on the right-hand side of the Vlasov equation are dominant, the plasma will be close to thermodynamic equilibrium, and the distribution function will deviate only slightly from a Maxwellian. In this limit, one can use fluid equations to evolve the lower, thermodynamic moments, i.e. number density, momentum and pressure, constructing closure relations to determine the higher moments by asymptotic analysis. This approach leads to the well-known Braginskii equations (Braginskii 1965), in which non-thermodynamic moments are expressed in terms of thermodynamic moments and their gradients, and in the magnetised limit, the direction of the local magnetic field. The Braginskii equations, or forms of them, are implemented in major codes both for astrophysical (Hopkins 2016; Berlok, Pakmor & Pfrommer 2019; Stone *et al.* 2020) and fusion applications (Sovinec *et al.* 2004; Günter *et al.* 2005; Ferraro & Jardin 2006; Günter *et al.* 2007; Breslau, Ferraro & Jardin 2009; Meier, Lukin & Shumlak 2010). The generalisation of this approach beyond the near-equilibrium approximation, in which a larger set of fluid moments is evolved and then some truncation of the fluid approximation is employed, is well-trodden ground (Hakim, Loverich & Shumlak 2006; Hakim 2008; Wang *et al.* 2015; Miller & Shumlak 2016; Allmann-Rahn, Trost & Grauer 2018; Ng, Hakim & Bhattacharjee 2018; Wang *et al.* 2020; Ng *et al.* 2020; Allmann-Rahn *et al.* 2024; Kuldinow *et al.* 2024b) but runs into the classical closure problem of expressing the highest moment in the fluid truncation in terms of the lower fluid moments (Grad 1949). Along these lines of inquiry, there is a rich and growing history of leveraging the connection between spectral representation of the distribution function in Hermite moments and the fluid hierarchy (Holloway 1996; Delzanno 2015; Parker & Dellar 2015; Vencels *et al.* 2016). This approach discretises the Vlasov equation directly with Hermite moments of some order, in effect creating a more general fluid hierarchy that converges to the kinetic description and achieving a computationally efficient approach for problems where only a few Hermite moments are needed to represent the solution.

Alternative asymptotic approaches that seek to directly reduce the kinetic equation instead of expressing the kinetic equation as a hierarchy of fluid moments are also a mature approach to approximating the kinetic dynamics of a plasma. In the limit the plasma is magnetised, one can obtain a variety of kinetic models that reduce the

¹We note that elsewhere in the literature, the inclusion of the collision operator for modelling discrete particle effects changes the name of this equation to the Boltzmann equation or the Vlasov–Fokker–Planck equation depending on the form of the collision operator; see Hénon (1982) for a discussion of this linguistic history.

full six-dimensional phase-space dynamics, such as KMHD (Kulsrud 1964, 1983) and other flavours of drift kinetics (Frieman, Davidson & Langdon 1966; Hinton & Wong 1985; Ramos 2008, 2016), and gyrokinetics (Antonsen & Lane 1980; Catto, Tang & Baldwin 1981; Frieman & Chen 1982; Brizard & Hahm 2007; Cary & Brizard 2009). All of these approaches average over the fast cyclotron motion to produce a five-dimensional kinetic equation, with gyrokinetics specifically considering an ordering in which FLR effects on the fluctuating quantities are retained and, thus, one can think of reducing the evolution of the particular particle motion to the evolution of ‘rings’ of charge.

In particular, gyrokinetic theory and the corresponding numerical discretisations of the gyrokinetic equation are one of the major breakthroughs in plasma physics in the last few decades (Krommes 2012), and this breakthrough forms the backbone of modern research in a variety of contexts, including astrophysical plasmas (Howes *et al.* 2006; Schekochihin *et al.* 2009) and magnetised fusion and turbulence theory (Abel *et al.* 2013). We draw particular attention to the numerical discretisation of gyrokinetics in recent works, which has likewise leveraged the connection between spectral representations of the kinetic equation and fluid hierarchies. For the case of gyrokinetics, a Hermite–Laguerre representation of the kinetic equation is directly connected to the gyrofluid moments of the gyrokinetic equation (Dorland & Hammett 1993). Similar to the works discretising the Vlasov equation directly with Hermite moments, these spectral expansions have created very computationally efficient methods for solving the gyrokinetic equation (Mandell *et al.* 2018; Frei, Jorge & Ricci 2020; Hoffmann *et al.* 2023*b*; Frei *et al.* 2024), as well as other magnetised models of plasma dynamics, such as the kinetic reduced electron heating model (Zocco & Schekochihin 2011; Loureiro, Schekochihin & Zocco 2013; Zocco *et al.* 2015; Loureiro *et al.* 2016) and drift kinetics (Parker *et al.* 2016).

The success of spectral methods along with the perspective afforded by the theoretical foundations of magnetised asymptotic models such as KMHD, drift kinetics and gyrokinetics provides a convenient lens for establishing the basis for the PKPM model. Consider the velocity space coordinate system employed in these magnetised plasma models:

$$\mathbf{v} = v_{\parallel} \mathbf{b}(\mathbf{x}, t) + v_{\perp} \cos \theta \boldsymbol{\tau}_1(\mathbf{x}, t) + v_{\perp} \sin \theta \boldsymbol{\tau}_2(\mathbf{x}, t). \quad (2.2)$$

A cylindrical coordinate system, where the unit vector \mathbf{b} is the axial direction aligned with the local magnetic field, the unit vectors $\boldsymbol{\tau}_1, \boldsymbol{\tau}_2$ define the plane perpendicular to the local magnetic field and θ is the velocity gyroangle. Before proceeding further, we make two important, related, points on nomenclature. The first is that this velocity coordinate system is also employed by magnetised models such as gyrokinetics, but in magnetised models such as gyrokinetics, there is a further configuration space transformation to gyrocentre coordinates. We emphasise that we are not transforming configuration space here and are maintaining the configuration space coordinates to be the particle position.² Furthermore, because we are not transforming configuration space to gyrocentre coordinates, we choose to call the angular coordinate in our cylindrical velocity space coordinates the velocity gyroangle to distinguish from derivations of gyrokinetics in which this angle is the gyrophase of

²Note that by particle position, we mean position in an Eulerian sense; we focus exclusively on distribution function dynamics so the configuration space coordinates correspond to the probability of finding particles at those specific positions, unlike Eulerian approaches to models such as gyrokinetics, which construct a distribution function of gyrocentres and, thus, determine the probability of a particles’ gyrocentre being at a particular position.

the particle along its cyclotron orbit because the configuration space coordinates are at gyrocentres.

In this coordinate system, an exact spectral representation of the distribution function could take the form,

$$f(\mathbf{x}, \mathbf{v}, t) = \sum_{j=0}^{\infty} \sum_{k=0}^{\infty} \sum_{\ell=-\infty}^{\infty} \mathcal{F}_{jk\ell}(\mathbf{x}, t) \exp\left(-\frac{m[v_{\parallel} - u_{\parallel}(\mathbf{x}, t)]^2}{2T_{\parallel}(\mathbf{x}, t)} - \frac{m[v_{\perp} - u_{\perp}(\mathbf{x}, t)]^2}{2T_{\perp}(\mathbf{x}, t)}\right) \\ \times \sqrt{\frac{m}{2\pi T_{\parallel}(\mathbf{x}, t)}} H_j\left(\sqrt{\frac{m}{2T_{\parallel}(\mathbf{x}, t)}}[v_{\parallel} - u_{\parallel}(\mathbf{x}, t)]\right) \\ \times \frac{m}{2\pi T_{\perp}(\mathbf{x}, t)} L_k\left(\frac{m[v_{\perp} - u_{\perp}(\mathbf{x}, t)]^2}{2T_{\perp}(\mathbf{x}, t)}\right) e^{i\ell\theta}, \quad (2.3)$$

where H_j are the physicists' Hermite polynomials,

$$H_m(x) = (-1)^m e^{x^2} \frac{d^m}{dx^m} e^{-x^2}, \quad (2.4)$$

L_k are the Laguerre polynomials,

$$L_m(x) = \frac{e^x}{m!} \frac{d^m}{dx^m} (e^{-x} x^m), \quad (2.5)$$

$e^{i\ell\theta}$ are the Fourier basis and $\mathcal{F}_{jk\ell}(\mathbf{x}, t)$ are the spectral coefficients encoding the representation of the distribution function in this spectral expansion. We have utilised u_{\parallel} , u_{\perp} , T_{\parallel} and T_{\perp} as the notation for a general set of shift and normalisation factors. We emphasise the choice of notation that u_{\parallel} , u_{\perp} , T_{\parallel} and T_{\perp} share symbols with the flow velocities and temperatures parallel and perpendicular to the local magnetic field is deliberate; while these are general shift and normalisation factors in the Hermite–Laguerre expansion, the optimal Hermite–Laguerre expansion – the spectral expansion whose zeroth, first and second velocity moments are the lowest-order fluid equations – is the one in which u_{\parallel} , u_{\perp} , T_{\parallel} and T_{\perp} are the local parallel and perpendicular flow velocities and temperatures.

This basis representation of Hermite in v_{\parallel} , Laguerre in v_{\perp} and Fourier in θ for the distribution function is exact, provided of course that one retains an infinite number of these Hermite, Laguerre and Fourier basis functions. In the discrete limit, a truncation of this series expansion is performed to Hermite polynomials, Laguerre polynomials and Fourier harmonics of some order. As mentioned previously, a particular choice of shift and normalisation factors such that the shifts, u_{\parallel} and u_{\perp} , are the parallel and perpendicular flow velocities and normalisations, T_{\parallel} and T_{\perp} , are the parallel and perpendicular temperatures, gives spectral expansion that can be directly related to the fluid hierarchy. Thus, the spectral expansion is optimised by this choice of shift and normalisation factors in terms of flow velocities and temperatures because we can now guarantee an exact representation of our lowest-order fluid equations by our truncated spectral expansion. We note that this truncation to some order corresponding to a fluid hierarchy of some order is the same irrespective of the details of the spectral expansion so long as the spectral expansion has these optimised shift and normalisation factors. In other words, a complete Hermite decomposition of the Vlasov equation or a Hermite–Laguerre decomposition of the gyrokinetic equation can just as easily be connected to fluid or gyrofluid equations

provided one makes the right choice of shift and normalisation factors. We also note that, in general, a spectral representation need only be applied to a subset of the degrees of freedom, e.g.

$$f(\mathbf{x}, \mathbf{v}, t) = \sum_{k=0}^{\infty} \sum_{\ell=-\infty}^{\infty} \mathcal{F}_{k\ell}(\mathbf{x}, v_{\parallel}, t) \exp\left(-\frac{m[v_{\perp} - u_{\perp}(\mathbf{x}, t)]^2}{2T_{\perp}(\mathbf{x}, t)}\right) \times \frac{m}{2\pi T_{\perp}(\mathbf{x}, t)} L_k\left(\frac{m[v_{\perp} - u_{\perp}(\mathbf{x}, t)]^2}{2T_{\perp}(\mathbf{x}, t)}\right) e^{i\ell\theta} \quad (2.6)$$

for an expansion in only the perpendicular degrees of freedom, v_{\perp} , θ , or

$$f(\mathbf{x}, \mathbf{v}, t) = \sum_{\ell=-\infty}^{\infty} \frac{1}{2\pi} \mathcal{F}_{\ell}(\mathbf{x}, v_{\parallel}, v_{\perp}, t) e^{i\ell\theta} \quad (2.7)$$

for an expansion only in the velocity gyroangle, θ .

Two important points are worth emphasising immediately. Firstly, the success of magnetised models such as drift kinetics and gyrokinetics reveals that with the right coordinate system about the local magnetic field, certain truncations of these spectral expansions already contain a significant amount of the physics of magnetised plasmas. These models, in effect, retain only the $\ell = 0$ Fourier harmonic due to the gyroaveraging and, thus, evolve only the gyrotropic part of the distribution function, or in the case of gyrokinetics the gyrocentre distribution function. In particular, spectral gyrokinetic codes that evolve the gyrotropic component of the gyrocentre distribution function, the $\ell = 0$ Fourier harmonic and a few Laguerre polynomials in v_{\perp} , have been utilised to study a diverse array of laboratory space, and astrophysical plasmas (Frei *et al.* 2023b; Hoffmann *et al.* 2023a; Mandell *et al.* 2024; Hoffmann, Balestri & Ricci 2024; Frei *et al.* 2024).

Secondly, however, the connection between this Hermite–Laguerre–Fourier spectral expansion and the classical fluid hierarchy of Braginskii and Grad is valid only for specific choices of shift and normalisation factors. To properly connect our truncated spectral expansion to the fluid hierarchy, the shift factors must be the bulk flow velocities of the plasma and the normalisation factors must be the temperatures of the plasma. Thus, the optimised shift and normalisation factors must be temporally and spatially dependent. Unsurprisingly, the use of shift and normalisation factors, which themselves depend on space and time, introduces significant complexity in constructing the discrete spectral representation, and the deployment of these methods up to this point has principally focused on constant shift and normalisation factors. Without proper accounting for these factors, the spectral representation will degrade in quality and more spectral coefficients may be required to accurately represent the dynamics of the plasma.

The principal challenge in extending spectral methods to these more general use cases with time-dependent shift and normalisation factors leads us to a necessary prerequisite discussion on coordinate transformations. Discrete spectral representations are constructed from orthogonality conditions, i.e. in one dimension,

$$\int_{-\infty}^{\infty} e^{-x^2} H_m(x) H_n(x) dx = \delta_{mn} \quad (2.8)$$

for Hermite polynomials, or

$$\int_0^{\infty} e^{-x} L_m(x) L_n(x) dx = \delta_{mn} \quad (2.9)$$

for Laguerre polynomials. Utilising these orthogonality conditions, one can derive evolution equations for each coefficient of the spectral expansion up to some desired order.

However, the introduction of time and spatially dependent shift and normalisation factors complicates our ability to utilise these orthogonality relations to construct the discrete spectral expansion. These orthogonality relations only hold for fixed input variables, i.e. two Laguerre polynomials with different shift and normalisation factors are not orthogonal to each other, so one must be careful when the basis expansion itself varies in space and time. But, if we instead consider a transformation to a new variable,

$$\zeta(\mathbf{x}, \mathbf{v}, t) = \mathbf{v} - \mathbf{u}(\mathbf{x}, t), \quad (2.10)$$

along with a careful absorption of the normalisation into the variable of integration, we can rearrange the spectral expansion's orthogonality condition. For example, the Laguerre orthonormality condition for the perpendicular velocity in (2.3) can be rearranged as

$$\begin{aligned} & \int_0^\infty \frac{m}{T_\perp} e^{-m\zeta_\perp^2/2T_\perp} L_m\left(\frac{m\zeta_\perp^2}{2T_\perp}\right) L_n\left(\frac{m\zeta_\perp^2}{2T_\perp}\right) \zeta_\perp d\zeta_\perp \\ &= \int_0^\infty e^{-m\zeta_\perp^2/2T_\perp} L_m\left(\frac{m\zeta_\perp^2}{2T_\perp}\right) L_n\left(\frac{m\zeta_\perp^2}{2T_\perp}\right) d\left(\frac{m\zeta_\perp^2}{2T_\perp}\right) = \delta_{mn}. \end{aligned} \quad (2.11)$$

Note that in this rearrangement, we have utilised the fact that the velocity coordinate transformation in (2.2) modifies the volume element

$$d^3\mathbf{v} = v_\perp dv_\parallel dv_\perp d\theta, \quad (2.12)$$

but this modification allows us to succinctly construct an orthogonality condition for our new spatially and temporally dependent coordinate.

Thus, we are well motivated to seek coordinate transformations that themselves contain the necessary modifications to the spectral basis to optimise the spectral expansion. While the use of spatially and temporally dependent coordinates is itself a non-trivial endeavour, through the careful construction of a particular coordinate system, we can shift the challenge in model discretisation back to the continuum limit and derive the necessary modifications to the Vlasov equation that can be optimally discretised by a spectral expansion. Importantly, we may transform the velocity space coordinates and configuration space coordinates independently of each other in the Vlasov equation, and in fact, we need only transform the velocity space coordinates to optimise our spectral expansions. In general, such a transformation of the velocity coordinate takes the form,

$$\mathbf{v} = \mathbf{v}(\mathbf{v}', \mathbf{x}', t'), \quad (2.13)$$

where $\mathbf{x} = \mathbf{x}(\mathbf{x}') = \mathbf{x}$ and $t = t(t') = t$ remain unchanged by the new coordinate transformation. The time and spatial derivatives then transform as

$$\frac{\partial}{\partial t} = \frac{\partial}{\partial t'} + \frac{\partial \mathbf{v}'}{\partial t} \cdot \nabla_{\mathbf{v}'}, \quad (2.14)$$

$$\nabla_{\mathbf{x}} = \nabla_{\mathbf{x}'} + (\nabla_{\mathbf{x}} \otimes \check{\mathbf{v}}') \cdot \nabla_{\mathbf{v}'}. \quad (2.15)$$

Note that the breve notation indicates with which index the dot product is performed. In Einstein summation notation, for Cartesian tensors, the spatial derivative transformation can be written as

$$\partial_{x_i} = \partial_{x'_i} + \partial_{x_i} v'_j \partial_{v'_j}. \quad (2.16)$$

We emphasise that the expression in (2.16) is only valid for Cartesian coordinates, but the general expressions (2.14) and (2.15) are coordinate independent.

The transformations presented below require careful use of coordinate independent notation to ensure that the derivations and final expressions are applicable in arbitrary coordinate systems. This generality is particularly important, for example, when using field-aligned or other non-orthogonal coordinates, as commonly employed in simulations of fusion reactors or when applying the expressions to plasma problems in non-Cartesian coordinates. Hence, to ensure our expressions remain coordinate independent, we use an extended form of vector and tensor notation throughout the remainder of the paper. For a brief description of our notation, see [Appendix A](#).

3. Coordinate transformations

The following two subsections detail the necessary algebraic steps to manipulate the Vlasov equation into a form with equivalent physical content, but which is amenable to our stated goal of an optimised spectral basis in a subset of the velocity degrees of freedom. These manipulations of our velocity space coordinate system to depend upon space and time are well known and utilised extensively in the derivation of, e.g. Kulsrud's KMHD (Kulsrud 1964, 1983) or Ramos' FLR kinetic theory (Ramos 2008, 2016). Nevertheless, we repeat these derivations within the text in our preferred notation so that the subsequent section on the optimised spectral expansion need not repeat any definitions to clarify our notation. Readers familiar with these kinds of coordinate transformations may comfortably skip to the next section, §4, on the spectral expansions, which produce the final model we discretise.

3.1. Transformation to a moving frame

Consider a velocity space coordinate transformation to a frame moving with velocity \mathbf{u} :

$$\mathbf{v} = \mathbf{v}' + \mathbf{u}(\mathbf{x}, t). \quad (3.1)$$

For this transformation, we have

$$\frac{\partial \mathbf{v}'}{\partial t} = -\frac{\partial \mathbf{u}}{\partial t}, \quad (3.2)$$

$$(\nabla_{\mathbf{x}} \otimes \check{\mathbf{v}}') \cdot \nabla_{\mathbf{v}'} = -(\nabla_{\mathbf{x}} \otimes \check{\mathbf{u}}) \cdot \nabla_{\mathbf{v}'}. \quad (3.3)$$

Using these in the Vlasov equation, we obtain

$$\frac{\partial \bar{f}}{\partial t} - \frac{\partial \mathbf{u}}{\partial t} \cdot \nabla_{\mathbf{v}'} \bar{f} + \nabla_{\mathbf{x}'} \cdot [(\mathbf{v}' + \mathbf{u}) \bar{f}] - [(\nabla_{\mathbf{x}} \otimes \check{\mathbf{u}}) \cdot \nabla_{\mathbf{v}'}] \cdot [(\mathbf{v}' + \mathbf{u}) \bar{f}] + \nabla_{\mathbf{v}'} \cdot (\mathbf{a}' \bar{f}) = 0, \quad (3.4)$$

where $\bar{f} = \bar{f}(\mathbf{x}', \mathbf{v}', t')$ and

$$\mathbf{a}' = \frac{q}{m}(\mathbf{E} + \mathbf{u} \times \mathbf{B}) + \frac{q}{m} \mathbf{v}' \times \mathbf{B}. \quad (3.5)$$

Since $\mathbf{u}(\mathbf{x}, t)$ does not depend on \mathbf{v}' , we can rearrange various terms above to obtain

$$\begin{aligned} \frac{\partial \bar{f}}{\partial t} + \nabla_{\mathbf{x}'} \cdot [(\mathbf{v}' + \mathbf{u}) \bar{f}] \\ + \nabla_{\mathbf{v}'} \cdot \left[\left(-\frac{\partial \mathbf{u}}{\partial t} - \mathbf{u} \cdot \nabla_{\mathbf{x}} \mathbf{u} - \mathbf{v}' \cdot \nabla_{\mathbf{x}} \mathbf{u} + \frac{q}{m} (\mathbf{E} + \mathbf{u} \times \mathbf{B}) + \frac{q}{m} \mathbf{v}' \times \mathbf{B} \right) \bar{f} \right] = 0. \end{aligned} \quad (3.6)$$

We can simplify this system by choosing \mathbf{u} to be the fluid velocity

$$\mathbf{u} = \frac{1}{n} \int \mathbf{v} f \, d^3 v, \quad (3.7)$$

where n is the number density. With this choice, we can use the equations for mass and momentum conservation,

$$\frac{\partial \rho \mathbf{u}}{\partial t} + \nabla_{\mathbf{x}} \cdot [\rho \mathbf{u} \mathbf{u} + \mathbf{P}] = \frac{q}{m} \rho [\mathbf{E} + \mathbf{u} \times \mathbf{B}] \rightarrow \quad (3.8)$$

$$\rho \left[\frac{\partial \mathbf{u}}{\partial t} + \mathbf{u} \cdot \nabla_{\mathbf{x}} \mathbf{u} \right] + \nabla_{\mathbf{x}} \cdot \mathbf{P} + \underbrace{\mathbf{u} \left[\frac{\partial \rho}{\partial t} + \nabla_{\mathbf{x}} \cdot (\rho \mathbf{u}) \right]}_{=0} = \frac{q}{m} \rho [\mathbf{E} + \mathbf{u} \times \mathbf{B}], \quad (3.9)$$

to obtain an equation for the velocity evolution

$$\frac{\partial \mathbf{u}}{\partial t} + \mathbf{u} \cdot \nabla_{\mathbf{x}} \mathbf{u} + \frac{1}{\rho} \nabla_{\mathbf{x}} \cdot \mathbf{P} = \frac{q}{m} (\mathbf{E} + \mathbf{u} \times \mathbf{B}), \quad (3.10)$$

where $\rho = mn$ is the mass density and \mathbf{P} is the pressure tensor defined as

$$\mathbf{P} = m \int (\mathbf{v} - \mathbf{u}) \otimes (\mathbf{v} - \mathbf{u}) f \, d^3 v = m \int \mathbf{v}' \otimes \mathbf{v}' \bar{f} \, d^3 v'. \quad (3.11)$$

We can then substitute (3.10) into (3.6) to simplify our transformed Vlasov equation to

$$\frac{\partial \bar{f}}{\partial t} + \nabla_{\mathbf{x}'} \cdot [(\mathbf{v}' + \mathbf{u}) \bar{f}] + \nabla_{\mathbf{v}'} \cdot \left[\left(\frac{1}{\rho} \nabla_{\mathbf{x}} \cdot \mathbf{P} - \mathbf{v}' \cdot \nabla_{\mathbf{x}} \mathbf{u} + \frac{q}{m} \mathbf{v}' \times \mathbf{B} \right) \bar{f} \right] = 0. \quad (3.12)$$

We note that because the velocity coordinates of (3.12) have been transformed to move with the local fluid velocity, we must have the condition that

$$\int \mathbf{v}' \bar{f} \, d^3 v' = 0. \quad (3.13)$$

Multiplying (3.12) by \mathbf{v}' and integrating over all velocity space shows that if (3.13) is satisfied at $t = 0$ then it will be satisfied for all $t > 0$, showing that this is an initial condition constraint on the distribution function.

In addition to solving the transformed Vlasov equation, to close the system of equations we also need to evolve the equation for the velocity (3.10), or momentum (3.8), with the pressure tensor determined by the the distribution function (3.11).

The transformed Vlasov equation coupled to the momentum/velocity equation has the same physical content as the Vlasov equation in the laboratory frame.

For further reference, we derive the equation for the evolution of the pressure tensor by multiplying (3.12) with $m\mathbf{v}' \otimes \mathbf{v}'$, integrating the velocity term by parts and then using the fact that $\nabla_{\mathbf{v}'} \otimes \mathbf{v}'$ is the metric tensor in velocity space, to find that

$$\begin{aligned} \frac{\partial \mathbf{P}}{\partial t} + \nabla_x \cdot [\mathbf{Q} + \mathbf{P} \otimes \check{\mathbf{u}}] + \nabla_x \cdot [\mathbf{u} \otimes \mathbf{P}(\check{\cdot}, \cdot) + \mathbf{P}(\check{\cdot}, \cdot) \otimes \mathbf{u}] - [\mathbf{u} \otimes (\nabla_x \cdot \mathbf{P}) \\ + (\nabla_x \cdot \mathbf{P}) \otimes \mathbf{u}] = \frac{q}{m} [\mathbf{B} \times \mathbf{P}(\check{\cdot}, \cdot) + \mathbf{B} \times \mathbf{P}(\cdot, \check{\cdot})]. \end{aligned} \quad (3.14)$$

We can take the trace of this equation and note that $\text{Tr}(\mathbf{P}) = 3p$ to derive an equation for the total scalar internal energy, $3p/2$, as

$$\frac{\partial}{\partial t} \frac{3}{2} p + \nabla_{x'} \cdot \left[\mathbf{q} + \frac{3}{2} p \mathbf{u} + \mathbf{u} \cdot \mathbf{P} \right] = \mathbf{u} \cdot [\nabla_x \cdot \mathbf{P}], \quad (3.15)$$

where the heat-flux vector is defined as

$$\mathbf{q} = \int \frac{1}{2} m v' 2 \mathbf{v}' \bar{f} d^3 \mathbf{v}' = \frac{1}{2} \text{Tr}(\mathbf{Q}), \quad (3.16)$$

and the trace is over any two of the three slots of the fully symmetric \mathbf{Q} . Here, \mathbf{Q} is the third-order heat-flux tensor defined as

$$\mathbf{Q} = m \int \mathbf{v}' \otimes \mathbf{v}' \otimes \mathbf{v}' \bar{f} d^3 \mathbf{v}'. \quad (3.17)$$

An alternate form of the pressure evolution equation can be derived by moving the $\nabla_{x'} \cdot [\mathbf{u} \cdot \mathbf{P}]$ term to the right-hand side to write instead

$$\frac{\partial}{\partial t} \frac{3}{2} p + \nabla_{x'} \cdot \left[\mathbf{q} + \frac{3}{2} p \mathbf{u} \right] = -\mathbf{P} : \nabla_{x'} \otimes \mathbf{u}. \quad (3.18)$$

In this form, we now recognise that the second moment of the Vlasov equation in the moving frame (3.12), gives the evolution of the internal energy of the plasma, and the total energy of the plasma can be reconstructed from the appropriate manipulation of the momentum equation (3.8) for the evolution of the total kinetic energy,

$$\begin{aligned} \mathbf{u} \cdot \left[\frac{\partial \rho \mathbf{u}}{\partial t} + \nabla_x \cdot (\rho \mathbf{u} \mathbf{u} + \mathbf{P}) \right] = \mathbf{u} \cdot \left[\frac{q}{m} \rho (\mathbf{E} + \mathbf{u} \times \mathbf{B}) \right] \\ \frac{1}{2} \frac{\partial \rho |\mathbf{u}|^2}{\partial t} + \nabla_x \cdot \left[\frac{1}{2} \rho |\mathbf{u}|^2 \mathbf{u} \right] = -\mathbf{u} \cdot [\nabla_x \cdot \mathbf{P}] + \frac{q}{m} \rho \mathbf{u} \cdot \mathbf{E}, \end{aligned} \quad (3.19)$$

which when summed with (3.15) gives the identical total energy equation obtained from the untransformed Vlasov equation.

3.2. Transformation to CGL frame

We now consider a magnetised plasma. The pressure tensor \mathbf{P} can be split into two parts, i.e.

$$\mathbf{P} = \mathbf{P}^C + \mathbf{\Pi}^a, \quad (3.20)$$

where \mathbf{P}^C is the Chew-Goldberger-Low (CGL) pressure part of the tensor (Chew, Goldberger & Low 1956) given by

$$\mathbf{P}^C = p_{\parallel} \mathbf{b} \otimes \mathbf{b} + p_{\perp} (\mathbf{g} - \mathbf{b} \otimes \mathbf{b}) \quad (3.21)$$

and Π^a is the trace-free, agyrotropic part, with \mathbf{g} the metric tensor in configuration space. We have defined $p_{\parallel} \equiv \mathbf{P} : \mathbf{b} \otimes \mathbf{b} = \mathbf{P}(\mathbf{b}, \mathbf{b})$, and because Π^a is trace free, we have $\text{Tr}(\mathbf{P}) = \text{Tr}(\mathbf{P}^C) = p_{\parallel} + 2p_{\perp} \equiv 3p$, where p is the scalar pressure. Now, for any second-order tensor \mathbf{A} , λ and \mathbf{r} are an eigenvalue/eigenvector pair if $\mathbf{A}(_, \mathbf{r}) = \lambda \mathbf{r}$. For the CGL part of the pressure tensor, it is straightforward to see that $\mathbf{P}^C(_, \mathbf{b}) = p_{\parallel} \mathbf{b}$ and $\mathbf{P}^C(_, \boldsymbol{\tau}) = p_{\perp} \boldsymbol{\tau}$ for all $\mathbf{b} \cdot \boldsymbol{\tau} = 0$. Hence, in a frame with orthonormal unit vectors $(\mathbf{b}, \boldsymbol{\tau}_1, \boldsymbol{\tau}_2)$, where $\boldsymbol{\tau}_{1,2}$ are orthogonal to \mathbf{b} and $\boldsymbol{\tau}_1 \times \boldsymbol{\tau}_2 = \mathbf{b}$, the CGL part of the pressure tensor will be diagonal.³ However, in general, these vectors are not the eigenvectors of the full pressure tensor \mathbf{P} . Nevertheless, we can always utilise this separation into gyrotropic and agyrotropic pressure tensors, and we call the frame in which the CGL part of the pressure tensor is diagonal the CGL frame.

We now transform the velocity coordinates to a local frame aligned with the $(\mathbf{b}, \boldsymbol{\tau}_1, \boldsymbol{\tau}_2)$ basis vectors. In this frame, we can write the transform

$$\begin{aligned} \mathbf{v}' = \mathbf{v}'(\mathbf{v}'', \mathbf{x}'', t'') &= v_{\parallel} \mathbf{b}(\mathbf{x}', t) + \mathbf{v}_{\perp} = v_{\parallel} \mathbf{b}(\mathbf{x}', t) + v_{\perp} \cos \theta \boldsymbol{\tau}_1(\mathbf{x}', t) \\ &\quad + v_{\perp} \sin \theta \boldsymbol{\tau}_2(\mathbf{x}', t), \end{aligned} \quad (3.22)$$

where $(w^1, w^2, w^3) \equiv (v_{\parallel}, v_{\perp}, \theta)$ form cylindrical velocity coordinates in the CGL frame. In general, the basis vectors depend both on position and time. For this transform, we can compute the tangent vectors in velocity space, $\tilde{\mathbf{e}}_i$, as

$$\tilde{\mathbf{e}}_i = \frac{\partial \mathbf{v}'}{\partial w^i}. \quad (3.23)$$

These are $\tilde{\mathbf{e}}_{\parallel} = \mathbf{b}$,

$$\tilde{\mathbf{e}}_{\perp} = \cos \theta \boldsymbol{\tau}_1 + \sin \theta \boldsymbol{\tau}_2, \quad (3.24)$$

$$\tilde{\mathbf{e}}_{\theta} = -v_{\perp} \sin \theta \boldsymbol{\tau}_1 + v_{\perp} \cos \theta \boldsymbol{\tau}_2. \quad (3.25)$$

The dual basis $\tilde{\mathbf{e}}^i$ are $\tilde{\mathbf{e}}^{\parallel} = \tilde{\mathbf{e}}_{\parallel}$, $\tilde{\mathbf{e}}^{\perp} = \tilde{\mathbf{e}}_{\perp}$ and

$$\tilde{\mathbf{e}}^{\theta} = -\frac{1}{v_{\perp}} \sin \theta \boldsymbol{\tau}_1 + \frac{1}{v_{\perp}} \cos \theta \boldsymbol{\tau}_2. \quad (3.26)$$

The Jacobian of the transform is simply $\mathcal{J}_v = v_{\perp}$. In terms of $\tilde{\mathbf{e}}_{\perp}$, we can write $\mathbf{v}_{\perp} = v_{\perp} \tilde{\mathbf{e}}_{\perp}$.

We can again use (2.14) and (2.15) to derive the Vlasov equation in the CGL frame. First note that

$$\nabla_{\mathbf{v}''} \cdot \left(\frac{\partial \mathbf{v}''}{\partial t} \right) = \frac{\partial}{\partial t} (\nabla_{\mathbf{v}''} \cdot \mathbf{v}'') = 0 \quad (3.27)$$

³An example coordinate systems in the case that the field is not uniformly pointing in one direction is given by considering $\boldsymbol{\tau}_1$ aligned with the magnetic curvature, $\mathbf{b} \cdot \nabla_{\mathbf{x}} \mathbf{b}$. Another example: in the case when \mathbf{b} is a constant vector, then one can locally align the z axis with the total magnetic field and take the Cartesian basis vectors as eigenvectors.

and

$$\nabla_{\mathbf{v}''} \cdot [\nabla_{\mathbf{x}'} \otimes \check{\mathbf{v}}''] = \nabla_{\mathbf{x}'} (\nabla_{\mathbf{v}''} \cdot \mathbf{v}'') = 0, \quad (3.28)$$

because $\nabla_{\mathbf{v}''} \cdot \mathbf{v}'' = 3$. With these identities, we can write the Vlasov equation in the CGL frame as

$$\frac{\partial \bar{f}}{\partial t} + \nabla_{\mathbf{x}''} \cdot [(v_{\parallel} \mathbf{b} + \mathbf{v}_{\perp} + \mathbf{u}) \bar{f}] + \frac{1}{v_{\perp}} \frac{\partial}{\partial w^i} (v_{\perp} a^i \bar{f}) = 0, \quad (3.29)$$

where now $\bar{f} = \bar{f}(\mathbf{x}'', v_{\parallel}, v_{\perp}, \theta, t)$ and $a^i = \tilde{\mathbf{e}}^i \cdot \mathbf{a}''$ are the components of the acceleration in the CGL frame

$$\mathbf{a}'' = \frac{\partial \mathbf{v}''}{\partial t} + (\mathbf{v}'' + \mathbf{u}) \cdot \nabla_{\mathbf{x}} \mathbf{v}'' + \frac{1}{\rho} \nabla_{\mathbf{x}} \cdot \mathbf{P} - \mathbf{v}'' \cdot \nabla_{\mathbf{x}} \mathbf{u} + \frac{q}{m} \mathbf{v}'' \times \mathbf{B}, \quad (3.30)$$

and $\mathbf{v}'' = v_{\parallel} \mathbf{b} + \mathbf{v}_{\perp}$.

In the CGL frame, the phase-space incompressibility can be read off from (3.29) as

$$\nabla_{\mathbf{x}''} \cdot [v_{\parallel} \mathbf{b} + \mathbf{v}_{\perp} + \mathbf{u}] + \frac{1}{v_{\perp}} \frac{\partial}{\partial w^i} (v_{\perp} a^i) = 0. \quad (3.31)$$

At this point, the physics content of (3.29) combined with the momentum equation (and Maxwell equations) is the same as the Vlasov–Maxwell system. No information has been lost in the process of the transformations to the local flow and CGL frames.

4. Spectral expansions in gyroangle and perpendicular velocity

With the Vlasov equation now obtained in the velocity coordinate system moving with the flow velocity and aligned with the local magnetic field, we are ready to deploy spectral expansions in velocity gyroangle and perpendicular velocity. As described above, these velocity coordinates are ideal coordinates to perform the expansions: the flow velocity is separated out of the coordinates and the coordinate system is locally aligned with the magnetic field. The combination of these transformations allows arbitrary flows, without any need to split the flow velocity into individual components parallel and perpendicular to the local magnetic field. Furthermore, we can accurately capture streaming along field lines while also allowing for a rapidly converging spectral expansion in the perpendicular degrees of freedom without any need for a time or spatially dependent shift vector.

4.1. Fourier expansion in the CGL frame

We first expand the distribution function in velocity gyroangle using the Fourier series (dropping primes on \mathbf{x})

$$\begin{aligned} \bar{f}(\mathbf{x}, v_{\parallel}, v_{\perp}, \theta, t) &= \bar{f}_0(\mathbf{x}, v_{\parallel}, v_{\perp}, t) \\ &+ \sum_{n=1}^{\infty} [\bar{f}_n^c(\mathbf{x}, v_{\parallel}, v_{\perp}, t) \cos n\theta + \bar{f}_n^s(\mathbf{x}, v_{\parallel}, v_{\perp}, t) \sin n\theta]. \end{aligned} \quad (4.1)$$

Here \bar{f}_0 is the gyrotropic part and $\bar{f}_n^{c,s}$ are the agyrotropic parts of the distribution function. These are given by

$$\bar{f}_0 = \frac{1}{2\pi} \int_0^{2\pi} \bar{f}(\mathbf{x}, v_{\parallel}, v_{\perp}, \theta, t) d\theta \quad (4.2)$$

and

$$\bar{f}_n^c(\mathbf{x}, v_{\parallel}, v_{\perp}, t) = \frac{1}{\pi} \int_0^{2\pi} \bar{f}(\mathbf{x}, v_{\parallel}, v_{\perp}, \theta, t) \cos n\theta \, d\theta, \quad (4.3)$$

$$\bar{f}_n^s(\mathbf{x}, v_{\parallel}, v_{\perp}, t) = \frac{1}{\pi} \int_0^{2\pi} \bar{f}(\mathbf{x}, v_{\parallel}, v_{\perp}, \theta, t) \sin n\theta \, d\theta, \quad (4.4)$$

for $n > 0$.

We can derive equations for each of the Fourier harmonics. However, to illustrate the approach, we focus on the gyrotropic distribution function \bar{f}_0 . We can derive the equation for the zeroth harmonic by integrating (3.29) over gyroangles to get

$$\begin{aligned} \frac{\partial \bar{f}_0}{\partial t} + \nabla_{\mathbf{x}} \cdot [(v_{\parallel} \mathbf{b} + \mathbf{u}) \bar{f}_0] + \nabla_{\mathbf{x}} \cdot \mathbf{M}_{\perp} \\ + \frac{1}{v_{\perp}} \frac{\partial}{\partial v_{\parallel}} \left(v_{\perp} \frac{1}{2\pi} \int_0^{2\pi} a^{\parallel} \bar{f} \, d\theta \right) + \frac{1}{v_{\perp}} \frac{\partial}{\partial v_{\perp}} \left(v_{\perp} \frac{1}{2\pi} \int_0^{2\pi} a^{\perp} \bar{f} \, d\theta \right) = 0. \end{aligned} \quad (4.5)$$

Here,

$$\begin{aligned} \mathbf{M}_{\perp}(\mathbf{x}, v_{\parallel}, v_{\perp}, t) &= \frac{1}{2\pi} \int_0^{2\pi} \mathbf{v}_{\perp} \bar{f}(\mathbf{x}, v_{\parallel}, v_{\perp}, \theta, t) \, d\theta \\ &= \frac{v_{\perp}}{2} [\bar{f}_1^c(\mathbf{x}, v_{\parallel}, v_{\perp}, t) \boldsymbol{\tau}_1 + \bar{f}_1^s(\mathbf{x}, v_{\parallel}, v_{\perp}, t) \boldsymbol{\tau}_2] \end{aligned} \quad (4.6)$$

is the contribution to the streaming term from agyrotropy of the distribution function.

We can compute $a^{\parallel} = \tilde{\mathbf{e}}^{\parallel} \cdot \mathbf{a}'' = \mathbf{b} \cdot \mathbf{a}''$ as

$$a^{\parallel} = \mathbf{v}_{\perp} \cdot \left[\frac{\partial \mathbf{b}}{\partial t} + (v_{\parallel} \mathbf{b} + \mathbf{v}_{\perp} + \mathbf{u}) \cdot \nabla_{\mathbf{x}} \mathbf{b} \right] + \frac{1}{\rho} \mathbf{b} \cdot [\nabla_{\mathbf{x}} \cdot \mathbf{P}] - \mathbf{b} \cdot [(v_{\parallel} \mathbf{b} + \mathbf{v}_{\perp}) \cdot \nabla_{\mathbf{x}} \mathbf{u}], \quad (4.7)$$

from which we find that

$$\begin{aligned} \frac{1}{2\pi} \int_0^{2\pi} a^{\parallel} \bar{f} \, d\theta &= \mathbf{b} \cdot \left[\frac{1}{\rho} \nabla_{\mathbf{x}} \cdot \mathbf{P} - v_{\parallel} \mathbf{b} \cdot \nabla_{\mathbf{x}} \mathbf{u} \right] \bar{f}_0 + \mathbf{M}_{\perp} \cdot \left[\frac{\partial \mathbf{b}}{\partial t} + (v_{\parallel} \mathbf{b} + \mathbf{u}) \cdot \nabla_{\mathbf{x}} \mathbf{b} \right] \\ &\quad - \mathbf{b} \cdot [\mathbf{M}_{\perp} \cdot \nabla_{\mathbf{x}} \mathbf{u}] + \mathbf{F}_{\perp\perp} : \nabla_{\mathbf{x}} \otimes \mathbf{b}, \end{aligned} \quad (4.8)$$

where

$$\mathbf{F}_{\perp\perp}(\mathbf{x}, v_{\parallel}, v_{\perp}, t) \equiv \frac{1}{2\pi} \int_0^{2\pi} (\mathbf{v}_{\perp} \otimes \mathbf{v}_{\perp}) \bar{f}(\mathbf{x}, v_{\parallel}, v_{\perp}, \theta, t) \, d\theta \quad (4.9)$$

is a second-order symmetric tensor. Using the Fourier expansion of the distribution function, we get

$$\begin{aligned} \mathbf{F}_{\perp\perp}(\mathbf{x}, v_{\parallel}, v_{\perp}, t) &= \frac{v_{\perp}^2 \bar{f}_0}{2} (\mathbf{g} - \mathbf{b} \otimes \mathbf{b}) + \frac{v_{\perp}^2 \bar{f}_2^c}{4} (\boldsymbol{\tau}_1 \otimes \boldsymbol{\tau}_1 - \boldsymbol{\tau}_2 \otimes \boldsymbol{\tau}_2) \\ &\quad + \frac{v_{\perp}^2 \bar{f}_2^s}{4} (\boldsymbol{\tau}_1 \otimes \boldsymbol{\tau}_2 + \boldsymbol{\tau}_2 \otimes \boldsymbol{\tau}_1), \end{aligned} \quad (4.10)$$

where we used $\mathbf{g} = \boldsymbol{\tau}_1 \otimes \boldsymbol{\tau}_1 + \boldsymbol{\tau}_2 \otimes \boldsymbol{\tau}_2 + \mathbf{b} \otimes \mathbf{b}$ to rewrite the first term. Using this result, we can compute

$$\begin{aligned} \mathbf{F}_{\perp\perp} : \nabla_x \otimes \mathbf{b} &= \frac{v_\perp^2 \bar{f}_0}{2} \nabla_x \cdot \mathbf{b} - \frac{v_\perp^2 \bar{f}_2^c}{4} \mathbf{b} \cdot (\boldsymbol{\tau}_1 \cdot \nabla \boldsymbol{\tau}_1 - \boldsymbol{\tau}_2 \cdot \nabla \boldsymbol{\tau}_2) \\ &\quad - \frac{v_\perp^2 \bar{f}_2^s}{4} \mathbf{b} \cdot (\boldsymbol{\tau}_1 \cdot \nabla \boldsymbol{\tau}_2 + \boldsymbol{\tau}_2 \cdot \nabla \boldsymbol{\tau}_1). \end{aligned} \quad (4.11)$$

The first term in this expression is the contribution to the parallel acceleration from the gyrotropic part of the distribution function, and the remaining two terms are the contributions from the agyrotropy of the distribution function. An alternate form of the first term can be obtained, since we can replace

$$\nabla_x \cdot \mathbf{b} = \nabla_x \cdot \frac{\mathbf{B}}{B} = \frac{1}{B} \nabla_x \cdot \mathbf{B} + \mathbf{B} \cdot \nabla_x \frac{1}{B} = -\frac{1}{B} \nabla_{\parallel} B, \quad (4.12)$$

where $\nabla_{\parallel} \equiv \mathbf{b} \cdot \nabla_x$.

Similarly, we can compute $a^\perp = \tilde{\mathbf{e}}^\perp \cdot \mathbf{a}''$ as

$$a^\perp = \tilde{\mathbf{e}}^\perp \cdot \left[-v_{\parallel} \frac{\partial \mathbf{b}}{\partial t} - v_{\parallel} (v_{\parallel} \mathbf{b} + \mathbf{v}_{\perp} + \mathbf{u}) \cdot \nabla_x \mathbf{b} + \frac{1}{\rho} \nabla_x \cdot \mathbf{P} - (v_{\parallel} \mathbf{b} + \mathbf{v}_{\perp}) \cdot \nabla_x \mathbf{u} \right]. \quad (4.13)$$

Since $v_{\perp} \tilde{\mathbf{e}}^\perp = \mathbf{v}_{\perp}$, we find that

$$\begin{aligned} v_{\perp} \frac{1}{2\pi} \int_0^{2\pi} a^\perp \bar{f} d\theta &= \mathbf{M}_{\perp} \cdot \left[-v_{\parallel} \frac{\partial \mathbf{b}}{\partial t} - v_{\parallel} (v_{\parallel} \mathbf{b} + \mathbf{u}) \cdot \nabla_x \mathbf{b} + \frac{1}{\rho} \nabla_x \cdot \mathbf{P} - v_{\parallel} \mathbf{b} \cdot \nabla_x \mathbf{u} \right] \\ &\quad - \mathbf{F}_{\perp\perp} : (v_{\parallel} \nabla_x \otimes \mathbf{b} + \nabla_x \otimes \mathbf{u}). \end{aligned} \quad (4.14)$$

Though the first term of the velocity gyroangle integrated perpendicular acceleration has only agyrotropic contributions arising from the coupling to the first Fourier harmonic, \mathbf{M}_{\perp} , the $\mathbf{F}_{\perp\perp}$ term in a^\perp does have a gyrotropic contribution as well – see (4.10) and the term proportional to \bar{f}_0 . Putting all these expressions together, we finally obtain the equation for the gyrotropic distribution function:

$$\begin{aligned} \frac{\partial \bar{f}_0}{\partial t} + \nabla_x \cdot [(v_{\parallel} \mathbf{b} + \mathbf{u}) \bar{f}_0] &+ \frac{\partial}{\partial v_{\parallel}} \left[\mathbf{b} \cdot \left(\frac{1}{\rho} \nabla_x \cdot \mathbf{P} - v_{\parallel} \mathbf{b} \cdot \nabla_x \mathbf{u} \right) \bar{f}_0 + \frac{v_\perp^2}{2} \nabla_x \cdot \mathbf{b} \bar{f}_0 \right] \\ &+ \frac{1}{v_{\perp}} \frac{\partial}{\partial v_{\perp}} \left[\frac{v_\perp^2}{2} (\mathbf{b} \cdot \{\mathbf{b} \cdot \nabla_x \mathbf{u}\} - \nabla_x \cdot \{v_{\parallel} \mathbf{b} + \mathbf{u}\}) \bar{f}_0 \right] + \text{AG} = 0. \end{aligned} \quad (4.15)$$

Here AG are the agyrotropic terms, which involve the first and second Fourier harmonics of the distribution function. The expressions for these terms are given in Appendix C. We note that to determine the coupling of \bar{f}_0 to the agyrotropic terms, further equations would be needed; for example, evolution equations for \mathbf{M}_{\perp} and $\mathbf{F}_{\perp\perp}$ can be derived by multiplying the Vlasov equation in our transformed coordinates, (3.29), by \mathbf{v}_{\perp} and $\mathbf{v}_{\perp} \otimes \mathbf{v}_{\perp}$ and integrating over the velocity gyroangle. In fact, this procedure of determining equations for, e.g. \mathbf{M}_{\perp} and $\mathbf{F}_{\perp\perp}$, provides a natural procedure for the determination of higher Fourier harmonics, at least

through the second Fourier harmonic, because the coupling to the $f_{1,2}^{c,s}$ coefficients of the Fourier expansion appears only through these vector and tensor combinations of Fourier coefficients and plane perpendicular to the magnetic field, $\boldsymbol{\tau}_{1,2}$.

In terms of the Fourier expansion, various velocity moments can be determined through integration over v_{\parallel} and v_{\perp} . For example, the number density is

$$n = 2\pi \int_0^{\infty} v_{\perp} dv_{\perp} \int_{-\infty}^{\infty} dv_{\parallel} \bar{f}_0, \quad (4.16)$$

and the CGL pressure tensor components can be computed as

$$p_{\parallel} = 2\pi \int_0^{\infty} v_{\perp} dv_{\perp} \int_{-\infty}^{\infty} dv_{\parallel} m v_{\parallel}^2 \bar{f}_0, \quad (4.17)$$

$$p_{\perp} = 2\pi \int_0^{\infty} v_{\perp} dv_{\perp} \int_{-\infty}^{\infty} dv_{\parallel} \frac{1}{2} m v_{\perp}^2 \bar{f}_0. \quad (4.18)$$

Thus, the gyrotropic part of the distribution function contains the total density and total internal energy. The agyrotropic part of the pressure tensor is

$$\begin{aligned} \boldsymbol{\Pi}^a = 2\pi m \int_0^{\infty} v_{\perp} dv_{\perp} \int_{-\infty}^{\infty} dv_{\parallel} \times & \left[v_{\parallel} (\mathbf{b} \otimes \mathbf{M}_{\perp} + \mathbf{M}_{\perp} \otimes \mathbf{b}) \right. \\ & \left. + \frac{v_{\perp}^2 \bar{f}_2^c}{4} (\boldsymbol{\tau}_1 \otimes \boldsymbol{\tau}_1 - \boldsymbol{\tau}_2 \otimes \boldsymbol{\tau}_2) + \frac{v_{\perp}^2 \bar{f}_2^s}{4} (\boldsymbol{\tau}_1 \otimes \boldsymbol{\tau}_2 + \boldsymbol{\tau}_2 \otimes \boldsymbol{\tau}_1) \right]. \end{aligned} \quad (4.19)$$

Clearly, both the first and second Fourier harmonics contribute to $\boldsymbol{\Pi}^a$. In the gyrotropic limit, it follows that we must have $\boldsymbol{\Pi}^a = 0$.

The heat-flux vector defined in (3.16) is

$$\mathbf{q} = (q_{\parallel} + q_{\perp}) \mathbf{b} + 2\pi \int_0^{\infty} v_{\perp} dv_{\perp} \int_{-\infty}^{\infty} dv_{\parallel} \frac{1}{2} m (v_{\parallel}^2 + v_{\perp}^2) \mathbf{M}_{\perp}, \quad (4.20)$$

where

$$q_{\parallel} = 2\pi \int_0^{\infty} v_{\perp} dv_{\perp} \int_{-\infty}^{\infty} dv_{\parallel} \frac{1}{2} m v_{\parallel}^3 \bar{f}_0, \quad (4.21)$$

$$q_{\perp} = 2\pi \int_0^{\infty} v_{\perp} dv_{\perp} \int_{-\infty}^{\infty} dv_{\parallel} \frac{1}{2} m v_{\parallel} v_{\perp}^2 \bar{f}_0 \quad (4.22)$$

are the parallel components of the parallel and perpendicular heat fluxes, respectively. These components are determined fully from the gyrotropic distribution function. On the other hand, the components of the heat-flux vector perpendicular to the magnetic field are determined from the first Fourier harmonic.

The characteristic velocities for the evolution of the gyrotropic distribution function can be read off from (4.15) with AG = 0 as

$$\dot{\mathbf{x}} = v_{\parallel} \mathbf{b} + \mathbf{u}, \quad (4.23)$$

$$\dot{v}_{\parallel} = \mathbf{b} \cdot \left(\frac{1}{\rho} \nabla_x \cdot \mathbf{P} - v_{\parallel} \mathbf{b} \cdot \nabla_x \mathbf{u} \right) + \frac{v_{\perp}^2}{2} \nabla_x \cdot \mathbf{b}, \quad (4.24)$$

$$\dot{v}_{\perp} = \frac{v_{\perp}}{2} [\mathbf{b} \cdot \{\mathbf{b} \cdot \nabla_x \mathbf{u}\} - \nabla_x \cdot \{v_{\parallel} \mathbf{b} + \mathbf{u}\}]. \quad (4.25)$$

Furthermore, integrating the phase-space incompressibility condition (3.31) over all angles gives

$$\nabla_{\mathbf{x}} \cdot \dot{\mathbf{x}} + \frac{\partial \dot{v}_{\parallel}}{\partial v_{\parallel}} + \frac{1}{v_{\perp}} \frac{\partial}{\partial v_{\perp}} (v_{\perp} \dot{v}_{\perp}) = 0. \quad (4.26)$$

Hence, in the gyrotropic limit, the evolution of the gyrotropic distribution function does not violate phase-space incompressibility. For reference, the portion of the parallel acceleration coming from the pressure tensor can be rewritten in a more familiar form as

$$\begin{aligned} \frac{1}{\rho} \mathbf{b} \cdot [\nabla_{\mathbf{x}} \cdot \mathbf{P}] &= \frac{1}{\rho} \mathbf{b} \cdot \nabla_{\mathbf{x}} p_{\parallel} + \frac{(p_{\parallel} - p_{\perp})}{\rho} \nabla_{\mathbf{x}} \cdot \mathbf{b} + \frac{1}{\rho} \mathbf{b} \cdot [\nabla_{\mathbf{x}} \cdot \mathbf{\Pi}^a], \\ &= \frac{1}{\rho} [\nabla_{\mathbf{x}} \cdot (p_{\parallel} \mathbf{b}) - p_{\perp} \nabla_{\mathbf{x}} \cdot \mathbf{b}] + \frac{1}{\rho} \mathbf{b} \cdot [\nabla_{\mathbf{x}} \cdot \mathbf{\Pi}^a]. \end{aligned} \quad (4.27)$$

4.2. Reduction to the parallel-kinetic-perpendicular-moment system

We now expand the gyrotropic distribution function in a Laguerre series in v_{\perp} as

$$\bar{f}_0(\mathbf{x}, v_{\parallel}, v_{\perp}, t) = \sum_{n=0}^{\infty} F_n(\mathbf{x}, v_{\parallel}, t) G_M(v_{\perp}, T_{\perp}) L_n \left(\frac{m v_{\perp}^2}{2 T_{\perp}} \right), \quad (4.28)$$

where $L_n(x)$ are Laguerre polynomials of order n and

$$G_M(v_{\perp}, T_{\perp}) = \frac{m}{2\pi T_{\perp}} e^{-m v_{\perp}^2 / 2 T_{\perp}}. \quad (4.29)$$

In these expressions, $T_{\perp} = T_{\perp}(\mathbf{x}, t)$ is the perpendicular temperature, in terms of which the perpendicular pressure is $p_{\perp} = n T_{\perp}$. The derivation of the equations for the Laguerre coefficients F_k is complicated by the fact that T_{\perp} depends on position as well as time. Typically, in this expansion, T_{\perp} would need to be determined from another equation, such as an equation for the perpendicular pressure.

The $F_k(\mathbf{x}, v_{\parallel}, t)$ coefficient of this series is

$$F_k(\mathbf{x}, v_{\parallel}, t) = 2\pi \int_0^{\infty} v_{\perp} dv_{\perp} L_k \left(\frac{m v_{\perp}^2}{2 T_{\perp}} \right) \bar{f}_0(\mathbf{x}, v_{\parallel}, v_{\perp}, t). \quad (4.30)$$

The number density and the parallel pressure (see (4.16) and (4.17)) are completely determined from the zeroth Laguerre coefficient of the gyrotropic distribution function:

$$n = \int_{-\infty}^{\infty} F_0 dv_{\parallel}, \quad (4.31)$$

$$p_{\parallel} = \int_{-\infty}^{\infty} m v_{\parallel}^2 F_0 dv_{\parallel}. \quad (4.32)$$

The parallel components of the heat flux are

$$q_{\parallel} = \int_{-\infty}^{\infty} \frac{1}{2} m v_{\parallel}^3 F_0 dv_{\parallel}, \quad (4.33)$$

$$q_{\perp} = T_{\perp} \int_{-\infty}^{\infty} v_{\parallel} (F_0 - F_1) dv_{\parallel}, \quad (4.34)$$

which are determined from just the first two Laguerre coefficients of the gyrotropic distribution function. Finally, the constraint (3.13) on the \mathbf{v}' moment of the distribution function shows that we must have

$$\int_{-\infty}^{\infty} v_{\parallel} F_0 \, dv_{\parallel} = 0, \quad (4.35)$$

$$\int_0^{\infty} v_{\perp} \, dv_{\perp} \int_{-\infty}^{\infty} dv_{\parallel} \mathbf{M}_{\perp} = 0. \quad (4.36)$$

4.2.1. Some preliminaries

To derive the equations for F_k for $k > 0$ (recall that $L_0 = 1$), we need to account for the fact that T_{\perp} depends both on space and time. To do this derivation then, we write

$$L_k \left(\frac{mv_{\perp}^2}{2T_{\perp}} \right) \frac{\partial \bar{f}_0}{\partial t} = \frac{\partial}{\partial t} \left[L_k \left(\frac{mv_{\perp}^2}{2T_{\perp}} \right) \bar{f}_0 \right] - \bar{f}_0 \frac{\partial}{\partial t} \left[L_k \left(\frac{mv_{\perp}^2}{2T_{\perp}} \right) \right]. \quad (4.37)$$

Now, using (B.5) we get

$$\frac{\partial}{\partial t} L_k \left(\frac{mv_{\perp}^2}{2T_{\perp}} \right) = -\frac{1}{T_{\perp}} \frac{\partial T_{\perp}}{\partial t} \left[k L_k \left(\frac{mv_{\perp}^2}{2T_{\perp}} \right) - k L_{k-1} \left(\frac{mv_{\perp}^2}{2T_{\perp}} \right) \right]. \quad (4.38)$$

Also,

$$\begin{aligned} L_k \left(\frac{mv_{\perp}^2}{2T_{\perp}} \right) \nabla_{\mathbf{x}} \cdot [(v_{\parallel} \mathbf{b} + \mathbf{u}) \bar{f}_0] &= \nabla_{\mathbf{x}} \cdot \left[(v_{\parallel} \mathbf{b} + \mathbf{u}) L_k \left(\frac{mv_{\perp}^2}{2T_{\perp}} \right) \bar{f}_0 \right] \\ &\quad - \bar{f}_0 \left\{ (v_{\parallel} \mathbf{b} + \mathbf{u}) \cdot \nabla_{\mathbf{x}} \left[L_k \left(\frac{mv_{\perp}^2}{2T_{\perp}} \right) \right] \right\}, \end{aligned} \quad (4.39)$$

where, as above, we can write

$$\nabla_{\mathbf{x}} \left[L_k \left(\frac{mv_{\perp}^2}{2T_{\perp}} \right) \right] = -\frac{1}{T_{\perp}} \nabla_{\mathbf{x}} T_{\perp} \left[k L_k \left(\frac{mv_{\perp}^2}{2T_{\perp}} \right) - k L_{k-1} \left(\frac{mv_{\perp}^2}{2T_{\perp}} \right) \right]. \quad (4.40)$$

4.2.2. The equation for F_k

We can multiply (4.15) by $L_k(mv_{\perp}^2/2T_{\perp})$ and integrate over all v_{\perp} to obtain

$$\begin{aligned} \frac{\partial F_k}{\partial t} + \nabla_{\mathbf{x}} \cdot [(v_{\parallel} \mathbf{b} + \mathbf{u}) F_k] + \frac{\partial}{\partial v_{\parallel}} \left[\mathbf{b} \cdot \left(\frac{1}{\rho} \nabla_{\mathbf{x}} \cdot \mathbf{P} - v_{\parallel} \mathbf{b} \cdot \nabla_{\mathbf{x}} \mathbf{u} \right) F_k \right. \\ \left. + [(2k+1)F_k - kF_{k-1} - (k+1)F_{k+1}] \frac{T_{\perp}}{m} \nabla_{\mathbf{x}} \cdot \mathbf{b} \right] \\ = S_k^T(\mathbf{x}, v_{\parallel}) + S_k(\mathbf{x}, v_{\parallel}). \end{aligned} \quad (4.41)$$

The source S_k^T appears because T_{\perp} depends both on space and time. Using the expressions derived in the previous section, we can write this source term as

$$S_k^T(\mathbf{x}, v_{\parallel}) = -\frac{1}{T_{\perp}} \left[\frac{\partial T_{\perp}}{\partial t} + (v_{\parallel} \mathbf{b} + \mathbf{u}) \cdot \nabla_{\mathbf{x}} T_{\perp} \right] (kF_k - kF_{k-1}). \quad (4.42)$$

The source S_k results from the integration by parts of the perpendicular velocity derivative. Calculating this term, we get

$$S_k(\mathbf{x}, v_{\parallel}) = [\mathbf{b} \cdot (\mathbf{b} \cdot \nabla_{\mathbf{x}} \mathbf{u}) - \nabla_{\mathbf{x}} \cdot (v_{\parallel} \mathbf{b} + \mathbf{u})] (kF_k - kF_{k-1}). \quad (4.43)$$

At this point we have all the equations we need to evolve the Laguerre coefficients of the gyrotropic distribution function. The number of Laguerre coefficients one will need will depend on the structure of the distribution function in the perpendicular coordinate. One yet undetermined quantity in these equations is T_{\perp} . We can derive an explicit equation for this quantity; however, we can also pursue an alternate approach that will completely eliminate the need for an auxiliary equation for T_{\perp} .

4.3. The first two Laguerre coefficients and perpendicular temperature

The evolution of the first two Laguerre coefficients of the gyrotropic distribution can be determined by first setting $k = 0$ in (4.41). This substitution gives

$$\begin{aligned} \frac{\partial F_0}{\partial t} + \nabla_{\mathbf{x}} \cdot [(v_{\parallel} \mathbf{b} + \mathbf{u}) F_0] \\ + \frac{\partial}{\partial v_{\parallel}} \left[\mathbf{b} \cdot \left(\frac{1}{\rho} \nabla_{\mathbf{x}} \cdot \mathbf{P} - v_{\parallel} \mathbf{b} \cdot \nabla_{\mathbf{x}} \mathbf{u} \right) F_0 + \mathcal{G} \nabla_{\mathbf{x}} \cdot \mathbf{b} \right] = 0, \end{aligned} \quad (4.44)$$

where we have defined

$$\mathcal{G} \equiv \frac{T_{\perp}}{m} (F_0 - F_1). \quad (4.45)$$

Furthermore, setting $k = 1$ in (4.41) gives

$$\begin{aligned} \frac{\partial F_1}{\partial t} + \nabla_{\mathbf{x}} \cdot [(v_{\parallel} \mathbf{b} + \mathbf{u}) F_1] \\ + \frac{\partial}{\partial v_{\parallel}} \left[\mathbf{b} \cdot \left(\frac{1}{\rho} \nabla_{\mathbf{x}} \cdot \mathbf{P} - v_{\parallel} \mathbf{b} \cdot \nabla_{\mathbf{x}} \mathbf{u} \right) F_1 + (3F_1 - F_0 - 2F_2) \frac{T_{\perp}}{m} \nabla_{\mathbf{x}} \cdot \mathbf{b} \right] \\ = -\frac{1}{T_{\perp}} \left[\frac{\partial T_{\perp}}{\partial t} + (v_{\parallel} \mathbf{b} + \mathbf{u}) \cdot \nabla_{\mathbf{x}} T_{\perp} \right] (F_1 - F_0) + S_1(\mathbf{x}, v_{\parallel}). \end{aligned} \quad (4.46)$$

Subtracting the second equation from the first, and multiplying throughout by T_{\perp}/m , we get

$$\begin{aligned} \frac{\partial \mathcal{G}}{\partial t} + \nabla_{\mathbf{x}} \cdot [(v_{\parallel} \mathbf{b} + \mathbf{u}) \mathcal{G}] \\ + \frac{\partial}{\partial v_{\parallel}} \left[\mathbf{b} \cdot \left(\frac{1}{\rho} \nabla_{\mathbf{x}} \cdot \mathbf{P} - v_{\parallel} \mathbf{b} \cdot \nabla_{\mathbf{x}} \mathbf{u} \right) \mathcal{G} + \left(4\mathcal{G} + \frac{2T_{\perp}}{m} \{F_2 - F_0\} \right) \frac{T_{\perp}}{m} \nabla_{\mathbf{x}} \cdot \mathbf{b} \right] \\ = [\mathbf{b} \cdot (\mathbf{b} \cdot \nabla_{\mathbf{x}} \mathbf{u}) - \nabla_{\mathbf{x}} \cdot (v_{\parallel} \mathbf{b} + \mathbf{u})] \mathcal{G}. \end{aligned} \quad (4.47)$$

Instead of solving the equation for F_1 , we can solve this equation for \mathcal{G} . The advantage of this approach is that the source $S_1^T(\mathbf{x}, v_{\parallel})$ due to the temporal and spatial variation of T_{\perp} does not appear, avoiding the need to compute the time and spatial derivatives of T_{\perp} . Furthermore, we claim that

$$p_{\perp} = nT_{\perp} = T_{\perp} \int_{-\infty}^{\infty} F_0 dv_{\parallel} = \int_{-\infty}^{\infty} T_{\perp} (F_0 - F_1) dv_{\parallel} = m \int_{-\infty}^{\infty} \mathcal{G} dv_{\parallel}, \quad (4.48)$$

thus eliminating the need to evolve an explicit equation for the perpendicular temperature.

As a consistency check, we integrate (4.47) over all velocities to obtain

$$\frac{\partial p_{\perp}}{\partial t} + \nabla_x \cdot [q_{\perp} \mathbf{b} + p_{\perp} \mathbf{u}] = p_{\perp} \mathbf{b} \cdot [\mathbf{b} \cdot \nabla_x \mathbf{u}] - q_{\perp} \nabla_x \cdot \mathbf{b} - p_{\perp} \nabla_x \cdot \mathbf{u}. \quad (4.49)$$

Likewise, multiplying (4.44) by $1/2 m v_{\parallel}^2$ and integrating over all velocities we get an evolution equation for the parallel pressure:

$$\frac{1}{2} \frac{\partial p_{\parallel}}{\partial t} + \nabla_x \cdot \left[q_{\parallel} \mathbf{b} + \frac{1}{2} p_{\parallel} \mathbf{u} \right] = -p_{\parallel} \mathbf{b} \cdot [\mathbf{b} \cdot \nabla_x \mathbf{u}] + q_{\parallel} \nabla_x \cdot \mathbf{b}. \quad (4.50)$$

If we add (4.49) and (4.50), we obtain

$$\begin{aligned} \frac{\partial}{\partial t} \left(\frac{1}{2} p_{\parallel} + p_{\perp} \right) + \nabla_x \cdot \left[(q_{\parallel} + q_{\perp}) \mathbf{b} + \left(\frac{1}{2} p_{\parallel} + p_{\perp} \right) \mathbf{u} \right] \\ = (p_{\perp} - p_{\parallel}) \mathbf{b} \cdot [\mathbf{b} \cdot \nabla_x \mathbf{u}] - p_{\perp} \nabla_x \cdot \mathbf{u}. \end{aligned} \quad (4.51)$$

Recall that in the gyrotropic limit,

$$\mathbf{P} = \mathbf{P}^C = p_{\parallel} \mathbf{b} \otimes \mathbf{b} + p_{\perp} (\mathbf{g} - \mathbf{b} \otimes \mathbf{b}), \quad (4.52)$$

which implies that

$$(p_{\perp} - p_{\parallel}) \mathbf{b} \cdot [\mathbf{b} \cdot \nabla_x \mathbf{u}] - p_{\perp} \nabla_x \cdot \mathbf{u} = -\mathbf{P} : \nabla_x \otimes \mathbf{u}. \quad (4.53)$$

Thus, utilising the fact that $3p/2 = p_{\parallel}/2 + p_{\perp}$, we obtain the gyrotropic limit of (3.18) from the second moment of the F_0 equation and the zeroth moment of the \mathcal{G} equation.

The statement that we evolve the perpendicular pressure p_{\perp} by evolving \mathcal{G} is non-trivial. In effect, we have absorbed the T_{\perp} normalisation of the Laguerre expansion that appears in our fundamental ansatz (4.28) into the evolution of \mathcal{G} , even though this normalisation must typically be determined independently and not depend on Laguerre coefficients. Thus, our spectral expansion in Laguerres can fully leverage the optimised spatially and temporarily dependent T_{\perp} normalisation without the need for auxiliary equations. Note this formulation of the equation for \mathcal{G} indicates that we must have the constraint

$$\int_{-\infty}^{\infty} F_1 dv_{\parallel} = 0. \quad (4.54)$$

From (4.46), can show that this is an initial-value constraint: that we must ensure (4.46) is true at $t = 0$ for it to be satisfied for all $t > 0$.

4.4. The lowest-order PKPM system of equations

We define the lowest-order PKPM system as the zeroth Fourier harmonic and the first two Laguerre coefficients, with the truncation that all higher Fourier harmonics and all higher Laguerre coefficients are zero. With these approximations, we are left with the following two coupled four-dimensional kinetic equations:

$$\begin{aligned} \frac{\partial F_0}{\partial t} + \nabla_x \cdot [(v_{\parallel} \mathbf{b} + \mathbf{u}) F_0] \\ + \frac{\partial}{\partial v_{\parallel}} \left[\mathbf{b} \cdot \left(\frac{1}{\rho} \nabla_x \cdot \mathbf{P} - v_{\parallel} \mathbf{b} \cdot \nabla_x \mathbf{u} \right) F_0 + \mathcal{G} \nabla_x \cdot \mathbf{b} \right] = 0, \end{aligned} \quad (4.55)$$

$$\begin{aligned}
& \frac{\partial \mathcal{G}}{\partial t} + \nabla_x \cdot [(v_{\parallel} \mathbf{b} + \mathbf{u}) \mathcal{G}] \\
& + \frac{\partial}{\partial v_{\parallel}} \left[\mathbf{b} \cdot \left(\frac{1}{\rho} \nabla_x \cdot \mathbf{P} - v_{\parallel} \mathbf{b} \cdot \nabla_x \mathbf{u} \right) \mathcal{G} + \left[4\mathcal{G} - 2 \frac{T_{\perp}}{m} F_0 \right] \frac{T_{\perp}}{m} \nabla_x \cdot \mathbf{b} \right] \\
& = [\mathbf{b} \cdot (\mathbf{b} \cdot \nabla_x \mathbf{u}) - \nabla_x \cdot (v_{\parallel} \mathbf{b} + \mathbf{u})] \mathcal{G}.
\end{aligned} \tag{4.56}$$

The system is closed via the solution of an equation for the flow velocity, \mathbf{u} , which comes from conservation of momentum,

$$\frac{\partial \rho \mathbf{u}}{\partial t} + \nabla_x \cdot [\rho \mathbf{u} \otimes \mathbf{u} + \mathbf{P}] = \rho \frac{q}{m} [\mathbf{E} + \mathbf{u} \times \mathbf{B}], \tag{4.57}$$

$$\mathbf{P} = p_{\parallel} \mathbf{b} \otimes \mathbf{b} + p_{\perp} (\mathbf{g} - \mathbf{b} \otimes \mathbf{b}), \tag{4.58}$$

$$p_{\parallel} = m \int v_{\parallel}^2 F_0 \, dv_{\parallel}, \tag{4.59}$$

$$p_{\perp} = m \int \mathcal{G} \, dv_{\parallel}, \tag{4.60}$$

plus Maxwell's equations for the evolution of the electromagnetic fields,

$$\frac{\partial \mathbf{B}}{\partial t} + \nabla_x \times \mathbf{E} = 0, \tag{4.61}$$

$$\epsilon_0 \mu_0 \frac{\partial \mathbf{E}}{\partial t} - \nabla_x \times \mathbf{B} = -\mu_0 \mathbf{J}, \tag{4.62}$$

$$\nabla_x \cdot \mathbf{E} = \frac{\rho_c}{\epsilon_0}, \tag{4.63}$$

$$\nabla_x \cdot \mathbf{B} = 0, \tag{4.64}$$

with the coupling to the electromagnetic fields arising directly from the momentum equation through the plasma currents,

$$\mathbf{J} = \sum_s \frac{q_s}{m_s} \rho_s \mathbf{u}_s. \tag{4.65}$$

5. An interlude on historical context

Having derived the PKPM model utilising velocity coordinate transformations to the local flow frame and frame aligned with the local magnetic field, followed by the spectral expansions in both velocity gyroangle and perpendicular velocity, it is worthwhile to place this system of equations in the larger historical context, with a focus on the lowest-order PKPM system of equations consisting of the zeroth Fourier harmonic and the first two Laguerre coefficients. Our principal goal throughout this discussion is two-fold: connect the physical content of the PKPM model to equation systems a reader may be more familiar with and simultaneously describe numerical difficulties that are ameliorated with the approach in the PKPM model. The discussion of numerical difficulties in certain asymptotic models is the principal motivation for this section, as our central ambition of the PKPM model is to leverage the same intuition that informed this long history of developing models

for magnetised, collisionless plasmas, but with an eye towards avoiding the difficulties that have prevented some of these analytical breakthroughs from being easily numerically integrable and, thus, leveraged for efficient modelling of these systems.

5.1. Connection to Kulsrud's KMHD and Ramos' FLR kinetic theory

One of the most foundational models in the theory of magnetised plasmas is KMHD, often referred to as Kulsrud's KMHD (Kulsrud 1964, 1983). Kinetic magnetohydrodynamics is a hybrid fluid-kinetic model that transforms the kinetic equation in an identical fashion as the PKPM derivation outlined here, first transforming velocity coordinates to a bulk fluid frame, specifically the $\mathbf{E} \times \mathbf{B}$ frame, and then transforming the velocity coordinates to a field-aligned coordinate system (v_{\parallel} , v_{\perp} , θ). However, following these transformations, an asymptotic expansion is performed with small parameter $\epsilon = m/e$ or simply $\epsilon = 1/e$, where m is the species mass and e is the elementary charge. Because the bulk fluid flow being utilised is only the $\mathbf{E} \times \mathbf{B}$ velocity, this asymptotic expansion yields an immediate dynamical consequence: the parallel electric field is also $\mathcal{O}(\epsilon)$ smaller than the perpendicular electric field, and to lowest order the distribution function is gyrotropic.

In this limit, the gyrotropic distribution function evolves as

$$\begin{aligned} \frac{\partial \bar{f}_0}{\partial t} + \nabla_{\mathbf{x}} \cdot [(v_{\parallel} \mathbf{b} + \mathbf{U}_E) \bar{f}_0] \\ + \frac{\partial}{\partial v_{\parallel}} \left[\left(-\mathbf{b} \cdot \frac{\partial \mathbf{U}_e}{\partial t} - \mathbf{b} \cdot \{\mathbf{U}_e \cdot \nabla_{\mathbf{x}} \mathbf{U}_e\} + \frac{q_s}{m_s} E_{\parallel} \right. \right. \\ \left. \left. - \mathbf{b} \cdot \{v_{\parallel} \mathbf{b} \cdot \nabla_{\mathbf{x}} \mathbf{U}_e\} + \frac{v_{\perp}^2}{2} \nabla_{\mathbf{x}} \cdot \mathbf{b} \right) \bar{f}_0 \right] \\ + \frac{\partial}{\partial v_{\perp}^2/2} \left[\frac{v_{\perp}^2}{2} (\mathbf{b} \cdot \{\mathbf{b} \cdot \nabla_{\mathbf{x}} \mathbf{U}_e\} - \nabla_{\mathbf{x}} \cdot \{v_{\parallel} \mathbf{b} + \mathbf{U}_e\}) \bar{f}_0 \right] = 0, \end{aligned} \quad (5.1)$$

where

$$\mathbf{U}_E = \frac{\mathbf{E} \times \mathbf{B}}{|\mathbf{B}|^2} \quad (5.2)$$

is the $\mathbf{E} \times \mathbf{B}$ velocity, and we have transformed the perpendicular velocity derivative from $1/v_{\perp} \partial_{v_{\perp}}$ to a derivative on the variable $v_{\perp}^2/2$ for convenience since everywhere the perpendicular velocity appears in this equation it appears as $v_{\perp}^2/2$. Note that typically, a further coordinate transformation is performed from $v_{\perp}^2/2$ to the magnetic moment $\mu = v_{\perp}^2/(2B)$, where $B = |\mathbf{B}|$ is the magnitude of the magnetic field, to further simplify the kinetic equation by eliminating the derivative in $v_{\perp}^2/2$ since the magnetic moment is conserved by the dynamics of this equation. Irrespective of whether one utilises v_{\perp} , $v_{\perp}^2/2$ or μ as a velocity coordinate, (5.1) is often referred to as the drift-kinetic equation (Frieman *et al.* 1966; Hinton & Wong 1985).

At first glance, it would seem that the only difference between this approach and the PKPM approach, at least when keeping only the zeroth Fourier harmonic, i.e. the gyrotropic component of the distribution function, is which particular hydrodynamic velocity is utilised for the initial velocity coordinate transformation. The characteristics of the particles in all the dimensions are identical save for a variable

substitution of $\mathbf{U}_E \rightarrow \mathbf{u}$ and a subsequent manipulation of the parallel forces to utilise conservation of momentum,

$$-\mathbf{b} \cdot \frac{\partial \mathbf{u}}{\partial t} - \mathbf{b} \cdot [\mathbf{u} \cdot \nabla_x \mathbf{u}] + \frac{q}{m} E_{\parallel} = \mathbf{b} \cdot \left[\frac{1}{\rho} \nabla_x \cdot \mathbf{P} \right]. \quad (5.3)$$

Indeed, we expect on scales larger than the gyroradius and in plasmas where the bulk velocity is dominated by the $\mathbf{E} \times \mathbf{B}$ velocity that the PKPM model contains all the physics of KMHD.

The differences between the PKPM approach and the classical approach of Kulsrud are made more salient when considering how the system is closed. To close the KMHD system, the kinetic equation in (5.1), for each species, is coupled to a set of bulk fluid equations for the evolution of the total mass density and total momentum,

$$\frac{\partial \rho}{\partial t} + \nabla_x \cdot [\rho \mathbf{U}] = 0, \quad (5.4)$$

$$\frac{\partial \rho \mathbf{U}}{\partial t} + \nabla_x \cdot \left[\rho \mathbf{U} \otimes \mathbf{U} + \sum_s \mathcal{P}_s \right] = \mathbf{J} \times \mathbf{B}, \quad (5.5)$$

where ρ is the total mass density, often approximated as simply the ion mass density, and \mathbf{U} is the centre-of-mass velocity, often approximated as simply the ion bulk velocity. Here, \mathcal{P}_s is the pressure tensor of species s ,

$$\mathcal{P}_s = p_{\parallel s} \mathbf{b} \otimes \mathbf{b} + p_{\perp s} (\mathbf{g} - \mathbf{b} \otimes \mathbf{b}), \quad (5.6)$$

$$p_{\parallel s} = \int m_s (v_{\parallel} - u_{\parallel s})^2 f_s dv_{\parallel} d \left(\frac{v_{\perp}^2}{2} \right), \quad (5.7)$$

$$p_{\perp s} = \int m_s \frac{v_{\perp}^2}{2} f_s dv_{\parallel} d \left(\frac{v_{\perp}^2}{2} \right), \quad (5.8)$$

where we have reintroduced the species index to the mass, parallel velocity and distribution function for clarity. We can see that \mathcal{P}_s is the same gyrotropic pressure tensor we defined earlier for the lowest-order PKPM system, but with a different means of computing the parallel pressure and assuming the only bulk perpendicular velocity is $\mathbf{E} \times \mathbf{B}$; in other words, there is an implicit ordering that the remaining guiding centre drifts, such as $\nabla_x \mathbf{B}$ and curvature drifts, are all smaller than $\mathbf{E} \times \mathbf{B}$. The forces on the bulk motion after summing over all species only require \mathbf{J} , the current density of the plasma, usually given simply by

$$\mathbf{J} = \frac{1}{\mu_0} \nabla_x \times \mathbf{B}, \quad (5.9)$$

if one also assumes non-relativistic flows, though generalisations of the KMHD approach to relativity are possible via the relativistic generalisations of guiding centre theory (Vandervoort 1960; Ripperda *et al.* 2018; Bacchini *et al.* 2020; Trent *et al.* 2023, 2024). Finally, the time evolution of the magnetic field is given by Faraday's equation

$$\frac{\partial \mathbf{B}}{\partial t} = -\nabla_x \times \mathbf{E}, \quad (5.10)$$

and in the commonly employed non-relativistic limit an Ohm's law for the electric field gives the electric field

$$\mathbf{E} = \mathbf{U} \times \mathbf{B}. \quad (5.11)$$

So, up to the coupling to the pressure tensor of each evolved species, the fluid equations, Faraday's law and the Ohm's law for the electric field are exactly the same equations as those of ideal MHD. It is only the closure – how the pressure is determined for the evolution of the momentum – that is affected by the kinetic response of the plasma.

Immediately we note two subtleties to the evolution of the KMHD system: the total momentum equation permits the development of perpendicular motions that are not $\mathbf{E} \times \mathbf{B}$, but these bulk motions do not explicitly feedback on the kinetic response of the plasma, and the parallel electric field is as yet unspecified by the Ohm's law. Firstly, the bulk motions drive perpendicular currents such as

$$\begin{aligned} \mathbf{J}_{\perp \mathcal{P}} &= -\frac{1}{|\mathbf{B}|^2} \left[\nabla_x \cdot \left(\sum_s \mathcal{P}_s \right) \times \mathbf{B} \right] \\ &= -\underbrace{\frac{\nabla_x \cdot (\sum_s p_{\perp s}) \times \mathbf{B}}{|\mathbf{B}|^2}}_{\text{diamagnetic}} - \underbrace{\sum_s (p_{\perp s} - p_{\parallel s}) \frac{(\mathbf{b} \cdot \nabla_x \mathbf{b}) \times \mathbf{B}}{|\mathbf{B}|^2}}_{\text{curvature}}, \end{aligned} \quad (5.12)$$

which we have labelled as the diamagnetic and curvature-driven perpendicular currents, respectively. However, as we noted earlier, the form of the kinetic equation in KMHD assumes that there are no further contributions of perpendicular bulk flows to the computation of the perpendicular pressure. Thus, for example, any diamagnetic currents that should modify the equilibrium pressure profile are not correctly captured by KMHD in its current form, at least dynamically, because the response of the kinetic equation does not include how the particles react to the presence of other perpendicular flows. These perpendicular currents do implicitly modify the local magnetic field, which itself may modify the plasma pressure through, e.g. adiabatic heating and cooling, but the interplay between the development of perpendicular flows and heating of the plasma is not contained in the KMHD system as written. Importantly, these sorts of time-dependent interplays between different components of the system, while subdominant in the asymptotics, may be a critical component of well-behaved numerical discretisations of time-dependent partial differential equations, as including the interplay allows the system to relax to the desired equilibrium instead of trying to satisfy potentially stiff constraint equations.

Furthermore, to obtain an equation for the parallel electric field, we must go to higher order in our expansion to find the parallel force balance equation from the evolution of the electron momentum

$$E_{\parallel} = -\frac{m_e}{en_e} \mathbf{b} \cdot \left[\frac{\partial n_e \mathbf{u}_e}{\partial t} + \nabla_x \cdot (n_e \mathbf{u}_e \otimes \mathbf{u}_e) + \frac{1}{m_e} \nabla_x \cdot \mathcal{P}_e \right] \approx -\frac{1}{en_e} \mathbf{b} \cdot \nabla_x \cdot \mathcal{P}_e, \quad (5.13)$$

assuming that the electron mass is small and, thus, the electron inertia is ignorable. Unfortunately, (5.13) is only a steady-state equation, and thus, its application to solving a time-dependent partial differential equation poses a non-trivial numerical

difficulty. It need not be the case that (5.13) holds instantaneously, and enforcing that it does may be impossible without some sort of numerical operator that diffuses spurious fluctuations in the parallel electric field.

Similar to the feedback of perpendicular currents on the particle dynamics, while the equilibrium is contained at the desired order in the derivation of the equation system, the relaxation to this equilibrium is not. In the case of solving this constraint equation for the parallel electric field, in the physical system there will be the development of parallel currents due to a parallel electric field, which then must relax to a state of $J_{\parallel} \approx 0$ and a parallel electric field supported by the parallel pressure force. But then in a time-dependent partial differential equation, we may develop spurious fluctuations in the parallel electric field caused by non-zero parallel currents since this equation system contains a kinetic equation for every evolved species. We are thus not guaranteed to satisfy the identity $J_{\parallel} = 0$ and (5.13) instantaneously in time as each species independently develops parallel flows.

These two subtleties, the lack of feedback of the other guiding centre drifts on the kinetic response of the plasma and the parallel electric field equation only arising due to a steady-state parallel force balance equation, were principal motivations for the work of Ramos (2008) and Ramos (2016) and the derivation of what Ramos (2008) referred to as FLR kinetic theory. By transforming to the total bulk flow frame, irrespective of the make up of that bulk flow, whether large parallel flows exist or all the guiding centre drifts are comparable in magnitude, all of the benefits of the KMHD formalism can be realised while eliminating the ambiguities of how to couple the fluid-kinetic system of equations. Not only the perpendicular electric field, but the parallel electric field too, are both eliminated from the kinetic equation via conservation of momentum. Furthermore, with a Fourier expansion in the velocity gyroangle, we can clearly identify both the evolution of the gyrotopic component of the distribution function and how the gyrotopic component couples to each subsequent Fourier harmonic as well as the impact of FLR effects on the plasma's evolution.

In this regard, the PKPM formalism is the realisation of the formalism outlined in Ramos (2008) to transform the velocity coordinates to the total flow frame but, to our knowledge, never numerically implemented anywhere. By transforming the velocity coordinates of each distribution function to their particular bulk flow frame and determining that bulk flow from conservation of momentum of that particular plasma species, the difficulties in handling the macroscopic parallel electric fields, parallel currents and the evolution of the equilibrium magnetic field due to, e.g. diamagnetic effects, are all self-consistently captured by the interplay and coupling of Maxwell's equations with each species' momentum equations. Where the PKPM approach diverges from the approach outlined in Ramos (2008) is the avoidance of any asymptotic ordering of our transformed Vlasov equation, and we instead reduce the number of velocity degrees of freedom compared with the full Vlasov–Maxwell system through the spectral expansions in velocity gyroangle and perpendicular velocity. In lieu of expanding the transformed Vlasov equation in powers of $\epsilon = \rho_s/L$, where ρ_s is the plasma species' gyroradius and L is the gradient scale length, to include FLR effects to some order in ϵ , the PKPM model can simply add Fourier harmonics to some desired order, and we consider it likely that even the first Fourier harmonic is thus a super-set of the physics contained in the approach outlined in Ramos (2008). This argument is not to say that the PKPM model cannot benefit from asymptotic reductions; for example, if desired and appropriate, further numerical savings can be straightforwardly attained by employing reductions

of Maxwell's equations, such as the Darwin approximation to eliminate the speed of light as the fastest time scale in the problem (Schmitz & Grauer 2006; Pezzi *et al.* 2019), because the field-particle couplings are entirely contained within the momentum equation.

The fact that the PKPM model as constructed can handle the interplay between all of the guiding centre drifts and develop macroscopic parallel electric fields from the self-consistent evolution of the kinetic equation and corresponding momentum equation can be contrasted with other KMHD-like models in the literature. For example, KMHD-like models such as the `kglobal` model (Arnold *et al.* 2019; Drake *et al.* 2019) avoid the numerical difficulties associated with the macroscopic parallel electric field by leveraging physics intuition about how the system attempts to restore parallel pressure balance and zero net parallel current, introducing a 'cold' electron fluid to instantaneously maintain quasi-neutrality and provide the expected return current that balances the local parallel flow of the 'hot', kinetic electrons. A total parallel pressure balance equation can then be defined to give the instantaneous parallel electric field similar to an Ohm's law prescription for the perpendicular electric field. In reality of course, because one is solving a kinetic equation this return current should be self-consistently contained as a sub-population of electrons in the electron distribution function. So, while `kglobal` does successfully apply the KMHD formalism, this formalism is leveraged only under a prescribed model for how the system maintains net zero parallel current.

The approach in models like `kglobal` has been highly successful (Arnold *et al.* 2021, 2022), a clear demonstration for why it has arguably been frustrating historically that KMHD resisted such easy discretisation. We thus argue the PKPM formalism presents a step forward in applying the same intuition that guided Kulsrud (1964) and later Ramos (2008) to a diverse array of plasma systems. The dynamical interplay of the guiding centre drifts with the kinetic response of the plasma, the evolution of the macroscopic electromagnetic fields including macroscopic parallel electric fields, and the self-consistent treatment of the distinct particle populations that may arise to, e.g. drive the parallel currents to zero, are all handled by the PKPM formalism at reduced computational cost compared with solving the Vlasov equation in full generality.

5.2. Comparison to other (hybrid) spectral method approaches

Given the widespread popularity of spectral methods for velocity space discretisations of kinetic equations, from fully kinetic (Holloway 1996; Delzanno 2015; Parker & Dellar 2015; Vencels *et al.* 2016; Roytershteyn & Delzanno 2018; Koshkarov *et al.* 2021; Pagliantini *et al.* 2023; Issan *et al.* 2024; Schween & Reville 2024; Schween *et al.* 2025) to gyrokinetics (Mandell *et al.* 2018; Frei *et al.* 2020; Hoffmann *et al.* 2023b; Frei *et al.* 2024) to drift kinetics (Parker *et al.* 2016) and other reduced kinetic models (Zocco & Schekochihin 2011; Loureiro *et al.* 2013; Zocco *et al.* 2015; Loureiro *et al.* 2016), it is worth discussing how the PKPM approach compares to these other techniques for discretising velocity space. The key differences are three-fold: the direct optimisation of the spectral basis with our coordinate transformations that avoids the difficulty in handling time and spatially dependent shift and normalisation factors, the hybrid nature of the PKPM approach, which does not perform a spectral expansion in all the velocity degrees of freedom, and the lack of transformation of configuration space coordinates that distinguishes the gyroangle Fourier harmonic expansion from the gyroaveraging procedure in spectral gyrokinetic codes. All of these differences arise due to specific goals of the PKPM model;

for example, as discussed in the beginning, we anticipate a spectral basis in v_{\parallel} can perform quite poorly on the phase-space structures that typically arise in magnetised plasma dynamics, such as field-aligned beams or trapped particle distributions.

Likewise, we focused in § 2 on why we pursued a path of transforming the velocity coordinates of the Vlasov equation to optimise the spectral basis. We reiterate that not only do we avoid any assumptions on the temporal or spatial variation of the flow velocity with our coordinate transformation to move with the local flow velocity, but that the linear combination of Laguerre coefficients to produce the second kinetic equation for \mathcal{G} , (4.47), in § 4 eliminates the need for an auxiliary equation for the time and spatially dependent Laguerre normalisation. Thus, we avoid the restriction in other spectral approaches that commonly assume a fixed and/or uniform shift and normalisation in the spectral expansion (Vencels *et al.* 2016; Koshkarov *et al.* 2021; Frei *et al.* 2023b, 2024).⁴ Furthermore, we show in § 6 test cases that illustrate the utility of not performing the spectral expansion in v_{\parallel} due to the non-trivial structure that can arise in a variety of magnetised systems, such as magnetic reconnection, similar to other groups use of a hybrid approach mixing spherical harmonics with finite element methods to optimise their simulations of cosmic ray transport (Schween & Reville 2024; Schween *et al.* 2025).

We thus use this section to draw a particular contrast between the spectral gyrokinetic approach and the PKPM model for the handling of the Laguerre expansion. There is an important consequence from the transformation from particle position to gyrocentre position in spectral velocity representations of the gyrokinetic equation: the Laguerre representation of the Bessel function utilised to perform the gyroaveraging of various quantities, such as in the electrostatic potential, requires a sum over Laguerres (Zocco *et al.* 2015):

$$J_0(k_{\perp}\rho_i v_{\perp}) = e^{-\frac{1}{4}k_{\perp}^2\rho_i^2} \sum_{n=0}^{\infty} \frac{(k_{\perp}^2\rho_i^2/4)^n}{n!} L_n(v_{\perp}^2). \quad (5.14)$$

Here, J_0 is the zeroth-order Bessel function of the first kind, k_{\perp} is the wavenumber perpendicular to the magnetic field and ρ_i is the ion gyroradius. An accurate treatment of gyroaveraging for large $k_{\perp}\rho_i$ thus requires an increasing number of Laguerre coefficients; see Appendix B of Mandell *et al.* (2018). While accuracy improvements for low Laguerres have been utilised in the gyrofluid approach (Dorland & Hammett 1993), and a number of nonlinear calculations have shown reasonable results in the fusion context, with works such as Hoffmann *et al.* (2023a) and Mandell *et al.* (2024) utilising as few as 3–4 Laguerres, in other cases such as the unstable entropy mode in Hoffmann *et al.* (2023b), more Laguerre resolution is needed to properly account for the FLR effects impact on the transport.

No such coupling of Laguerres occurs in the PKPM model because we have kept the configuration space coordinates untransformed; we obtain the distribution function at the particle position, not the gyrocentre position. In the PKPM formalism, each successive Fourier harmonic in velocity gyroangle will have its own Laguerre expansion. We can thus identify the physics of each Fourier harmonic Laguerre coefficient by Laguerre coefficient. For example, the first Fourier harmonic gives

⁴We draw a distinction here between spectral methods utilised in δf equations, such as those used to discretise the δf gyrokinetic equation (Mandell *et al.* 2018; Hoffmann *et al.* 2023b) compared with ‘full’ f discretisations of either the Vlasov equation or gyrokinetic equation since in a δf approach it is very natural to assume a fixed shift and normalisation to the spectral basis either in both space and time or just time.

the evolution of \mathbf{M}_\perp and the zeroth Laguerre coefficient of \mathbf{M}_\perp can be utilised to obtain the component of the agyrotropic pressure tensor proportional to \mathbf{M}_\perp in (4.19). Likewise, the first Laguerre coefficient of \mathbf{M}_\perp can be utilised to obtain the heat flux of the perpendicular temperature perpendicular to the magnetic field in (4.20), the $v_\perp^2 \mathbf{M}_\perp$ term. We defer a systematic comparison of the accuracy of FLR effects in the PKPM approach compared with a spectral gyrokinetic code to a future publication, but we note for now that because the PKPM model does not transform configuration space coordinates to gyrocentre coordinates or perform any gyroaveraging, the Laguerre couplings remain local at every k_\perp , and thus, there is no obvious need for large Laguerre resolution at large k_\perp in the PKPM approach. What specific impact this representation of the distribution function in perpendicular velocity and gyroangle, instead of gyrocentre, perpendicular velocity and gyrophase, has on the physics of, e.g. the entropy cascade (Schekochihin *et al.* 2009; Tatsuno *et al.* 2009) is as yet undetermined, but at an initial glance the couplings that can require high Laguerre resolution are not present in the PKPM approach.

6. A brief demonstration of the model

We now seek to demonstrate the new PKPM model in a handful of non-trivial nonlinear problems that clearly show the utility of the approach. We emphasise here that the following benchmarks are merely meant to exhibit the successful numerical implementation of the model, and we defer a systematic comparison to theory and fully kinetic simulations to the second paper in this two-part series. Nevertheless, it is the goal of this section to illustrate that the significant reduction in the number of degrees of freedom yields a cost-effective model for understanding plasma systems that are inaccessible with traditional asymptotic approaches. The PKPM model is implemented within the `Gkeyll` simulation framework utilising a DG finite element method (Reed & Hill 1973; Cockburn & Shu 1998, 2001; Hesthaven & Warburton 2007) for the spatial discretisation of all components of the system: the kinetic equations for the F_0 and \mathcal{G} distribution functions, (4.55) and (4.56), the conservation of momentum equation coupled to the pressure tensor computed from these kinetic equations, (4.57)–(4.60), and Maxwell's equation. Time integration is handled with an explicit strong stability preserving third-order Runge–Kutta method (Shu 2002). These choices of spatial discretisation and time integration follow exactly the same procedures as other `Gkeyll` kinetic equation implementations (Juno *et al.* 2018; Hakim & Juno 2020; Mandell *et al.* 2020). All the simulations performed in these demonstrations of the model also utilise the same DG method for a conservative Lenard–Bernstein operator for self-collisions – the extension of the Lenard–Bernstein collision operator for the PKPM model is given here in Appendix D, and the numerical details of discretising the collision operator can be found in Hakim *et al.* (2020).

6.1. Parallel electrostatic shock

Shock waves, specifically collisionless shock waves, are omnipresent in our universe. In astrophysical systems where the collisional mean free path is large, the dynamics of the nonlinear wave steepening and rapid conversion of bulk kinetic energy into other forms of energy such as particle acceleration and heating in these shock waves are not mediated by collisions, but a myriad of collisionless processes such as wave–particle interactions and kinetic instabilities. To demonstrate the PKPM model, we consider the case of a parallel shock, where the incoming

supersonic flow is aligned with the local magnetic field. In this shock geometry, on short time scales, there is the potential for electrostatic shocks driven by nonlinear steepening of ion acoustic modes, but only up to a critical Mach number (Forslund & Shonk 1970; Sorasio *et al.* 2006). If the incoming flows are sufficiently large, there will be no slow down of the supersonic flow, and the fast plasma can propagate freely, smoothly transitioning around obstacles or interpenetrating the ambient medium through which the plasma is propagating.

To demonstrate that the PKPM model reproduces this transition from shocked flows to interpenetrating flows and, thus, contains a complete description of the collisionless physics of electrostatic shocks, we perform two simulations of colliding plasma flows, similar to previous studies of electrostatic shocks. We initialise an electron–proton plasma in a box of length $L_x = 3584\lambda_D$, where $\lambda_D = v_{the}/\omega_{pe}$ is the electron Debye length, $v_{the} = \sqrt{T_e/m_e}$ is the electron thermal velocity and $\omega_{pe} = \sqrt{e^2 n_0 / \epsilon_0 m_e}$ is the electron plasma frequency. Here, T_e is the electron temperature, m_e is the electron mass, e is the elementary charge, n_0 is the reference electron density and ϵ_0 is the permittivity of free space. For the purposes of these simulations, all of these quantities are normalised to values of 1.0 so that all length scales are normalised with respect to the electron Debye length, all velocities are normalised with respect to the electron thermal velocity, and all time scales are normalised with respect to the inverse electron plasma frequency. This electron–proton plasma is initialised with Maxwellian distributions and a supersonic flow for both species in the negative x direction towards a reflecting wall at $x = 0$, which leads to a shock wave or interpenetrating plasma propagating in the positive x direction. A continuous supply of plasma is provided with a copy boundary condition at $x = L_x$ ⁵ in exact analogy to the ‘reflecting wall’ set-up commonly employed in particle-in-cell simulations of collisionless shocks and identical to the initial conditions of previous continuum simulations of collisionless shocks.

Specific shock parameters are as follows: we utilise the real proton–electron mass ratio $m_p/m_e = 1836$, a proton–electron temperature ratio $T_p/T_e = 0.25$, a reference magnetic field strength $\mathbf{B} = B_0 \hat{\mathbf{x}} = \hat{\mathbf{x}}$ so the magnetic field points in the x direction the entirety of the simulation on the time scale of the electrostatic dynamics, and an electron–electron collisionality $\nu_{ee} = 10^{-6}\omega_{pe}$, with the ion–ion collisionality commensurately decreased by the square root of the mass ratio and temperature ratio to the 3/2 power. We consider two Mach numbers, one below and one above the critical Mach number, where $M_s = u_{x_0}/c_s$ is the Mach number, u_{x_0} is the magnitude of the upstream flow velocity and $c_s = \sqrt{T_e/m_p}$ is the sound speed. The two simulations have upstream Mach numbers of $M_s = 3.0$ and $M_s = 5.0$. We choose to utilise a colder proton population to reduce the ion acoustic damping and, thus, generate stronger shock waves in the cases when the plasma produces a shock. The critical Mach number is $M_s \sim 3.0$, but we note that this critical Mach number was determined for plasmas with only one-velocity dimension (Forslund & Shonk 1970), and the PKPM model is constructed to be three dimensional in velocity space. As such, we expect with this definition of the sound speed, without any additional $\mathcal{O}(1)$ factors for the adiabatic index of the plasma, that the $M_s = 3.0$ simulation will shock, while

⁵Within Gkeyll, this boundary condition corresponds to copying all quantities: both PKPM distribution functions F_0 and \mathcal{G} and momentum $\rho\mathbf{u}$ for both species, as well as the electromagnetic fields, in the grid cell just abutting the boundary, the ‘skin’ cell, into the ghost or halo layer of cells. In this case, because the momentum is initialised in the negative x direction, we then have a continuous injection of plasma from the boundary at $x = L_x$.

the $M_s = 5.0$ simulation will not shock.⁶ This subtlety of the conditions under which a one-velocity dimensional plasma shocks compared with a three-velocity dimensional plasma has already been proven to be a use case for the PKPM model, as an early version of the PKPM model was utilised to understand measurements of shock formation, and lack of shock formation compared with fluid model predictions, in the plasma-Jet driven magneto-inertial fusion experiment (Cagas *et al.* 2023).

The final input file specifications are our velocity space extents, grid resolutions and polynomial orders for the DG finite element method we utilise. The velocity grid extents are $[-8v_{the}, 8v_{the}]$ for the electrons and $[-64v_{thp}, 64v_{thp}]$ for the protons for the $M_s = 3.0$ simulation and $[-128v_{thp}, 128v_{thp}]$ for the protons for the $M_s = 5.0$ simulation.⁷ We utilise $N_x = 1792$ grid points in configuration space, $\Delta x = 2\lambda_D$, with linear polynomials in configuration space, and $\Delta v_{\parallel} = 0.0625v_{the}$ for both species with quadratic polynomials in velocity space, so that the electrons have $N_{v_{\parallel}} = 256$ and the protons have $N_{v_{\parallel}} = 2048$ and $N_{v_{\parallel}} = 4096$ velocity grid points for the $M_s = 3.0$ and $M_s = 5.0$ simulations, respectively. These simulations utilised 32 56-core compute nodes on the Frontera cluster at the Texas Advanced Computing Center; the $M_s = 3.0$ ran for half an hour for a total of 16 node hours, while the $M_s = 5.0$ used an hour of computing time for a total of 32 node hours.

Currently we utilise large velocity space extents for the protons in shock simulations due to the significant transient generated by the large $\partial u_x / \partial x$ at early times, since with this reflecting wall set-up $\partial u_x / \partial x$ is infinite at $t = 0, x = 0$. The result of this large $\partial u_x / \partial x$ is the generation of a small amount of reflected particles at very high velocity in the hydrodynamic frame that propagate upstream and have no bearing on the evolution of the plasma. Once the transient has relaxed, the vast majority of the plasma is contained in a velocity space volume a quarter to an eighth in size, and we consider it worthwhile future work to explore an optimised initial set-up of shock simulations in this model to reduce the need to resolve this transient high velocity reflection. Nevertheless, we wish to emphasise that the fact that this numerical implementation can successfully evolve this transient stably is evidence of the robustness of this implementation, and thus, suggests that the PKPM model is not by any means a numerically brittle model despite its complexity.

We show in figure 1 the evolution of the fluid moments at $t = 1500\omega_{pe}^{-1}$ for the two upstream Mach numbers. All fluid moments are normalised to their upstream values to facilitate cross-comparison between the $M_s = 3.0$ and $M_s = 5.0$ simulation since the upstream flows and energies are different for these two simulations. We note the key features of the $M_s = 3.0$ indicative of a shock: a sudden density pile-up, a sharp stagnation of the flow in conjunction with this density pile-up, rapid electron heating with the electron parallel pressure increasing by nearly a factor of 15 compared with the density increasing by a factor of 3, and a commensurate decrease in the total ion energy and ion pressure corresponding to the conversion of ion energy into electron heating and electromagnetic energy. In contrast, the $M_s = 5.0$ simulation

⁶For a plasma with three-velocity dimensions, the sound speed in the cold ion limit is formally $c_s = \sqrt{\gamma_e T_e / m_p}$, where $\gamma_e = 5/3$. With this definition of the sound, our two simulations have upstream Mach numbers of $M_s = 3.0/\sqrt{5/3} \sim 2.32$ and $M_s = 5.0/\sqrt{5/3} \sim 3.87$. Because our protons are colder than the electrons, even if we include the contribution to the sound speed from the ion temperature, $c_s = \sqrt{(\gamma_e T_e + \gamma_i T_i) / m_p} = \sqrt{25/12} \sqrt{T_e / m_p}$, the $M_s = 3.0/\sqrt{25/12} \sim 2.04$ and $M_s = 5.0/\sqrt{25/12} \sim 3.46$, we still satisfy the conditions for the two simulations being below and above the critical Mach number.

⁷Note that because this simulation is electrostatic and the only coupling between the plasma and electromagnetic fields is Ampere's law in one dimension where $\nabla_{\mathbf{x}} \times \mathbf{B} = 0$, we do not need to specify v_{the}/c for how non-relativistic the simulation is, as there are no light waves in this simulation.

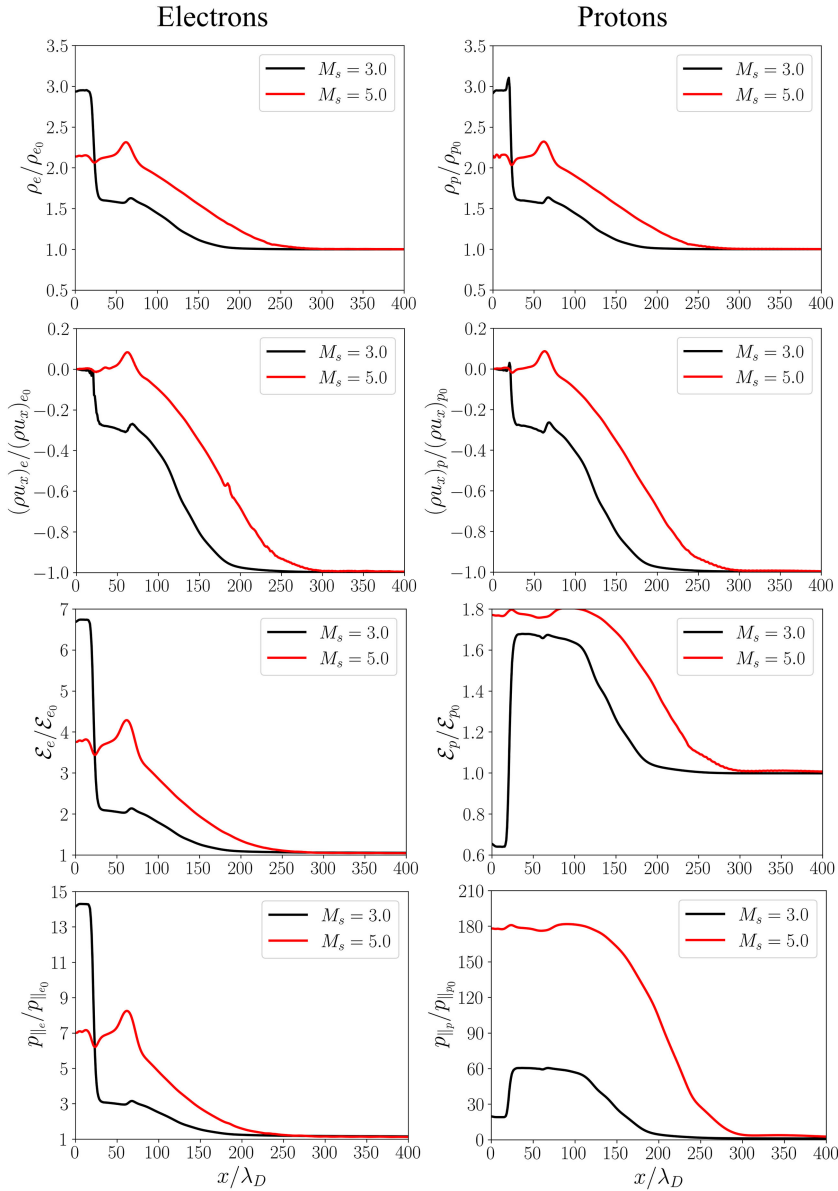


FIGURE 1. Electron (left column) and proton (right column) mass density (top row), momentum density (middle top row), total energy density (middle bottom row) and parallel pressure (bottom row) at $t = 1500\omega_{pe}^{-1}$ for upstream Mach numbers $M_s = 3.0$ (black) and $M_s = 5.0$ (red). All quantities are normalised to their upstream values for ease of comparison between the $M_s = 3.0$ and $M_s = 5.0$ cases since their upstream flows and energies are different. The characteristics of a shock wave are clearly identifiable in the $M_s = 3.0$ simulation: a sharp pile-up of the density, a rapid stagnation of the flow, significant electron heating over the same length scale and a decrease in the ion energy from the rapid conversion of ion energy into both electron heating and electromagnetic energy. On the other hand, the $M_s = 5.0$ case exhibits no such sharp transitions, with a smooth gradient up to a total mass density $\rho \sim 2$ and total momentum $\rho u_x \sim 0.0$ for both the electrons and protons, corresponding to two interpenetrating beams of plasma.

shows a smoother transition to the downstream region that is more characteristic of two interpenetrating beams of plasma: the mass density and ion energy density downstream are $\rho_s \sim 2$, $\mathcal{E}_p \sim 2$, and so the two colliding plasma beams are simply adding their density and energy.

We can see further evidence of the shocked versus unshocked flows examining the distribution functions for these two upstream Mach numbers, specifically the F_0 coefficient corresponding to integrating the distribution function over both v_\perp and θ . We plot in [figure 2](#) the electron and proton F_0 distribution functions in both the local fluid flow frame provided by the numerical solution of the PKPM model, and in the lab frame as would traditionally be obtained from the solution of the Vlasov–Maxwell system of equations; see, for example, [Juno *et al.* \(2018\)](#) for simulations of electrostatic shocks with Gkeyll’s Vlasov–Maxwell solver. Note that these distribution function plots are normalised to their respective maximum values on the grid, e.g. $F_{0s} = F_{0s} / \max(F_{0s})$. For the $M_s = 3.0$ simulation, we can more clearly identify the characteristics of a shock, specifically the trapping of both electrons and protons in the downstream region around $x \sim 25\lambda_D$. On the other hand, the $M_s = 5.0$ simulation shows no significant broadening of the electron distribution function. Furthermore, the proton distribution function in the $M_s = 5.0$ simulation is simply two interpenetrating beams of protons at close to the upstream flow velocity of $u_{x_0} = 10v_{thp}$. We draw particular attention to the local fluid flow frame distribution functions for the protons as evidence of the successful non-trivial numerical implementation of this model. We observe that as the reflected population propagates upstream, the fluid flow frame distribution function naturally adjusts due to the pressure forces to produce an approximately even distribution function with only high odd moments, such as heat fluxes. The first moment of the F_0 distribution function thus remains 0 as we expect.

This initial electrostatic evolution only couples the F_0 and \mathcal{G} kinetic equations through the collision operator; and in both of these simulations, but especially the $M_s = 3.0$ case where a true shock develops, a significant temperature anisotropy develops, with $T_\parallel > T_\perp$. Therefore, as the shock propagates, electromagnetic instabilities can be excited that will generate large transverse fluctuations and change the shock from being a purely parallel shock to a quasi-parallel, or even locally quasi-perpendicular, shock. The fastest growing modes in this case, such as the electron firehose and Alfvén ion cyclotron instabilities, require FLR effects to properly capture their growth and saturation, and thus, only retaining the zeroth Fourier harmonic is inadequate for accurately simulating the transition from an electrostatic to an electromagnetic parallel shock ([Gary *et al.* 2001](#)). Nevertheless, recent work using extended fluid models to model the proton parallel firehose instability suggests that accounting for the agyrotropic components of the pressure tensor provides an accurate model for these temperature anisotropy-driven instabilities via the FLR effects approximated by evolving the full pressure tensor ([Walters *et al.* 2024](#)). Thus, adding one, or at most two, Fourier harmonics will be sufficient to capture the necessary FLR effects to simulate both where in wavenumber space the fastest growing modes exist and their overall saturation due to the generated magnetic field structure, making the PKPM approach a potentially powerful tool for modelling of collisionless shocks in these particular parameter regimes.

We note that at higher Mach numbers where significant particle acceleration occurs due to processes such as shock-drift acceleration ([Paschmann *et al.* 1982](#); [Sckopke *et al.* 1983](#); [Anagnostopoulos & Kaliabetsos 1994](#); [Anagnostopoulos *et al.* 1998](#); [Ball & Melrose 2001](#); [Anagnostopoulos, Tenentes & Vassiliadis 2009](#)) and

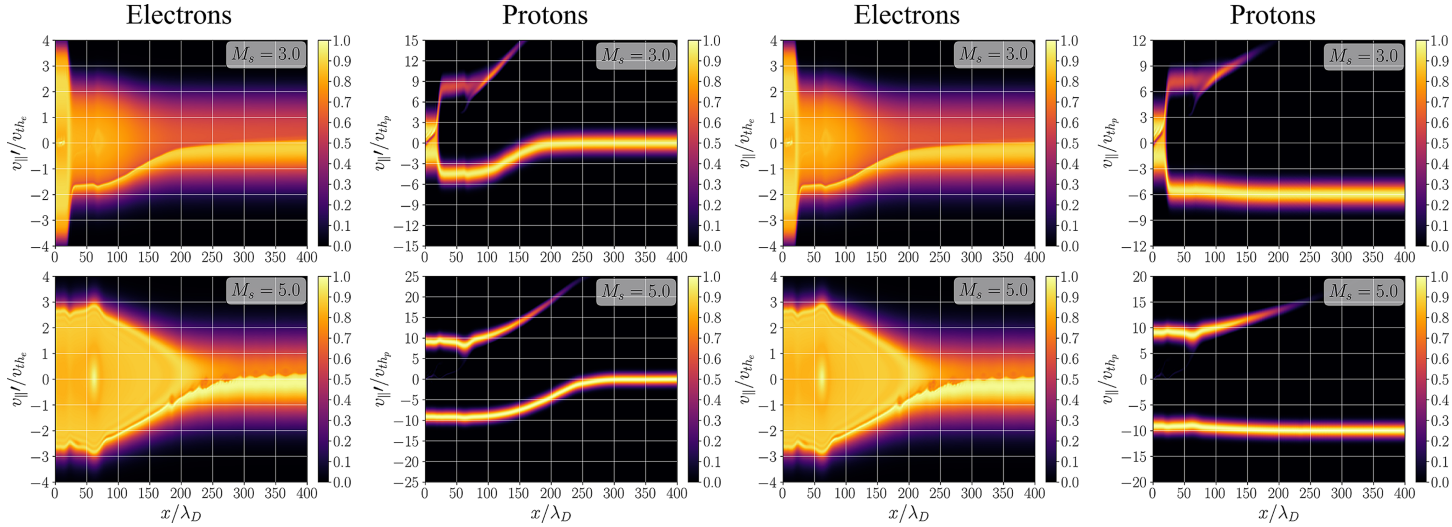


FIGURE 2. The F_0 distribution function in the local fluid flow frame for the electrons (left column) and protons (left middle column), and the F_0 distribution function in the lab frame for the electrons (right middle column) and protons (right column) for the $M_s = 3.0$ (top row) and $M_s = 5.0$ (bottom row) simulations. In the lab frame, the incoming proton beam is centred at the upstream velocity, $u_{x0} = 6.0v_{th_i}$ and $u_{x0} = 10.0$, as we expect, and the characteristics of the shock with the trapped electron and ion populations are identifiable in the $M_s = 3.0$ simulation, while the $M_s = 5.0$ simulation shows only two distinct ion beams propagating through each other. We also draw attention to the form of the proton distribution function in the local fluid flow frame and emphasise that these are the distribution functions that are directly solved for by the numerical method. As expected, the distribution function adjusts in the local fluid flow frame to preserve the identity that the first moment is zero. Note that these distribution function plots are normalised to their respective maximum values on the grid, e.g. $F_{0s} = F_{0s} / \max(F_{0s})$.

diffusive shock acceleration (Fermi 1949, 1954; Blandford & Ostriker 1978; Ellison 1983; Blandford & Eichler 1987; Decker 1988; Malkov & Drury 2001), the PKPM model is likely to be inefficient for representing the kinetic response of the plasma. The particle distribution functions that result from these shock acceleration processes are typically highly agyrotropic, and would thus necessitate a large number of Fourier harmonics and Laguerre coefficients to resolve. But, we emphasise that in the case considered here, at relatively low Mach number, the relative inexpensiveness of these simulations means that, once the necessary FLR effects are included for correctly modelling the saturation of the excited temperature anisotropy instabilities, the multiscale nature of these subcritical, collisionless shocks that transition from electrostatic to electromagnetic shocks will be possible with the PKPM model. Furthermore, because the PKPM model is ultimately defined per species, with the transformation of the velocity coordinates to move with the local flow velocity employing that particular species flow velocity, we can imagine unique hybrid modelling approaches where a fully kinetic proton treatment could be coupled to a PKPM electron treatment, thus reducing the computational expense of modelling electrons at modest Mach numbers where the electrons stay magnetised through the shock.

6.2. Moderate guide-field magnetic reconnection

Equally ubiquitous to collisionless shocks as a mechanism by which plasma's rearrange their energy budget is the phenomenon of magnetic reconnection, whereby magnetic fields change their topology to a lower energy state and transfer this excess energy to the plasma. In collisionless plasma systems where the resistivity is very small, the onset of magnetic reconnection is considered to be a fundamentally kinetic process. The plasma can only break field lines at microscopic length scales where the plasma demagnetises and the plasma particles are no longer constrained to follow the magnetic field.

Importantly though, magnetic reconnection is commonly observed componentwise; many plasma systems are undergoing what is referred to as 'guide-field' reconnection. In the geometry of these systems, we can divide the dynamical fields into a set of planar reconnecting components and a component perpendicular to the plane known as the guide field that the plasma particles will still try to 'stick' to even as the in-plane reconnecting components vanish at the point of magnetic reconnection where the magnetic field is changing its topology. We can thus ask: even with retaining only the zeroth Fourier harmonic and thus constraining the plasma to be gyrotropic, how well does the PKPM model capture guide-field reconnection?

A number of studies have shown gyrokinetic models of reconnection compare favourably to fully kinetic simulations in the limit that the guide field is strong (TenBarge *et al.* 2014; Muñoz *et al.* 2015), $B_g \gg B_0$, where B_g is the magnitude of the guide field and B_0 is the magnitude of the reconnecting field. Alternatively, one can think of this limit as the $\delta B/B \ll 1$ limit – a natural limit for standard derivations of gyrokinetics that assume a strong background field and only weak perturbations. But, we have continually emphasised that the PKPM approach is not an asymptotic one, and thus, we need not restrict ourselves to a strong guide-field limit. So long as there is a guide field of at least modest strength, do the plasma particles stay magnetised through the layer? The answer to this question is yes: a number of studies (Swisdak *et al.* 2005; Le *et al.* 2013; Egedal, Le & Daughton 2013) have shown that even at $B_g \approx 0.1\text{--}0.2B_0$, or $\delta B/B \sim 5\text{--}10$, the electrons are still magnetised through the reconnection layer, provided the electrons are sufficiently light and a realistic proton–electron mass ratio is utilised.

We consider two moderate guide-field cases: $B_g = B_0$ and $B_g = 0.5B_0$, or $\delta B/B_g = 1$ and $\delta B/B_g = 2$. We initialise a force-free current sheet in $2X1V$, (x, y, v_{\parallel}) , geometry of the form

$$J_{x_e} = -\frac{B_0}{w_0} \frac{\tanh(y/w_0) \operatorname{sech}^2(y/w_0)}{\sqrt{(B_g/B_0)^2 + \operatorname{sech}^2(y/w_0)}}, \quad (6.1)$$

$$J_{z_e} = \frac{B_0}{w_0} \operatorname{sech}^2\left(\frac{y}{w_0}\right), \quad (6.2)$$

$$B_x = -B_0 \tanh\left(\frac{y}{w_0}\right), \quad (6.3)$$

$$B_z = B_0 \sqrt{\left(\frac{B_g}{B_0}\right)^2 + \operatorname{sech}^2\left(\frac{y}{w_0}\right)}, \quad (6.4)$$

where current is given entirely to the electrons to satisfy Ampere's law. A $\sim 1\%$ Geospace Environmental Modelling (GEM)-like perturbation is utilised (Birn *et al.* 2001), along with perturbations to the first 20 wave modes with $\sim 1\%$ noise in B_x , B_y , and J_z to break the symmetry of the GEM-like perturbation and accelerate the development of the reconnection, similar to TenBarge *et al.* (2014). These simulations utilise the standard GEM reconnection challenge proton–electron temperature ratio $T_p/T_e = 5$, a realistic proton–electron mass ratio, $m_p/m_e = 1836$, and a similar box size as the original GEM reconnection challenge: $L_x = 8\pi d_p$, $L_y = 4\pi d_p$, where $d_p = c/\omega_{pp}$ is the proton inertial length and $\omega_{pp} = \sqrt{e^2 n_0 / \epsilon_0 m_p}$ is the proton plasma frequency.

Other parameters are as follows: $\beta_e = 2\mu n_0 T_e / B_0^2 = 1/6$ defined in terms of the upstream in-plane magnetic field, velocity space extents $[-8v_{th_s}, 8v_{th_s}]$ for both the electrons and protons, $v_{the}/c = 1/16$, $v_{ee} = 10^{-2} \Omega_{cp}$, where $\Omega_{cp} = eB_0/m_p$ is the proton cyclotron frequency defined in terms of the upstream in-plane magnetic field strength. v_{pp} is commensurately smaller by the square root of the mass ratio.⁸ We show the results of three different simulations, $B_g = B_0$ and $B_g = 0.5B_0$ both with $N_x \times N_y \times N_{v_{\parallel}} = 896 \times 448 \times 32$ corresponding to $\Delta x \sim 1.2d_e$, $\Delta v_{\parallel} = 0.5v_{th_s}$, and one higher resolution simulation with $B_g = 0.5B_0$ and $N_x \times N_y \times N_{v_{\parallel}} = 1792 \times 896 \times 32$, corresponding to $\Delta x \sim 0.6d_e$. We utilise periodic boundary conditions in x , a reflecting wall for the plasma and conducting walls for the electromagnetic fields in y , and zero-flux boundary conditions in v_{\parallel} . Like the parallel electrostatic shock simulations, these simulations also utilise linear polynomials in configuration space and quadratic polynomials in velocity space. We employ a small amount of hyperdiffusion in the momentum equation on scales comparable to the electron inertial length, $\nu_{Hyp} = 10^{-2} d_e^4$ for the lower resolution simulations and $\nu_{Hyp} = 10^{-3} d_e^4$ for the higher resolution simulation. The total cost of these simulations is relatively modest; the 896×448 resolution simulations required 24 hours on 128 56-core nodes on the Frontera cluster at the Texas Advanced Computing Center, ~ 3000 node hours in

⁸Note that the proton–proton collision frequency should also formally be $(T_e/T_p)^{(3/2)}$ smaller, but these collisionalities are chosen principally to provide some velocity space regularisation for finite velocity space resolution without modifying the collisionless dynamics and so this additional factor is ignored.

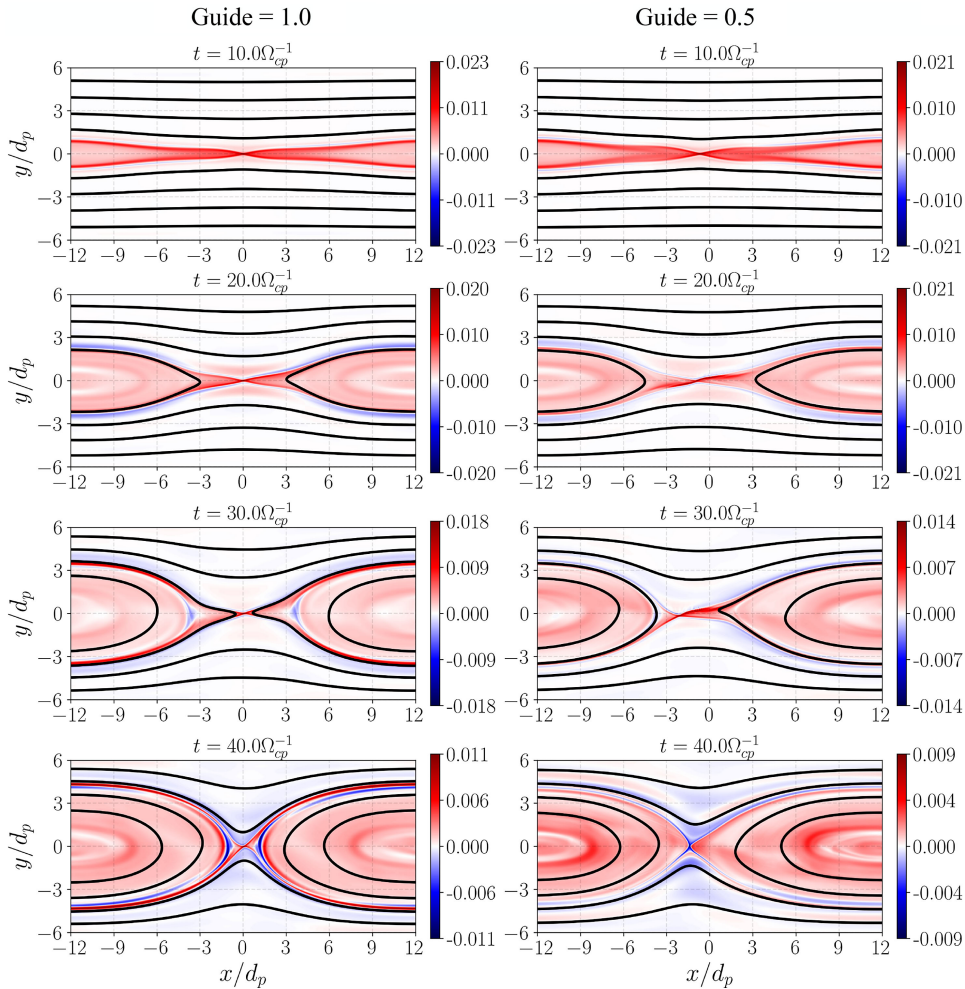


FIGURE 3. Evolution of the out-of-plane current density, J_z , with contours of the in-plane magnetic field superimposed by computing A_z , the out-of-plane vector potential, from the in-plane B_x and B_y for the $B_g = B_0$ (left) and $B_g = 0.5B_0$ (right) lower resolution simulations. We observe morphologies of the current layer consistent with Le *et al.* (2013), which found at lower electron β_e a transition from a regime at a lower guide field in which an extended current layer forms from the magnetised electrons developing strong anisotropy and driving a perpendicular current across field lines, to a regime in which the magnetic tension in the guide field causes the current and density to peak near the diagonally opposed separator field lines and negate the impact of the electron anisotropy on the magnetic field's overall tension (see figure 5). This contrast is especially clear at $t = 20\Omega_{ci}^{-1}$ and $30\Omega_{ci}^{-1}$ as the reconnection rate reaches its peak values (see figure 7) and we can see a more concentrated current layer in the $B_g = B_0$ simulation compared with the extended current layer in the $B_g = 0.5B_0$ simulation.

total, and the higher resolution simulation cost the expected $\sim 25\,000$ Frontera node hours from the doubling of the resolution and halving of the size of the time step.

We show in figure 3 the evolution of the out-of-plane current density J_z with contours of the in-plane magnetic field superimposed by computing A_z , the out-of-plane vector potential, from the in-plane B_x and B_y for the lower resolution

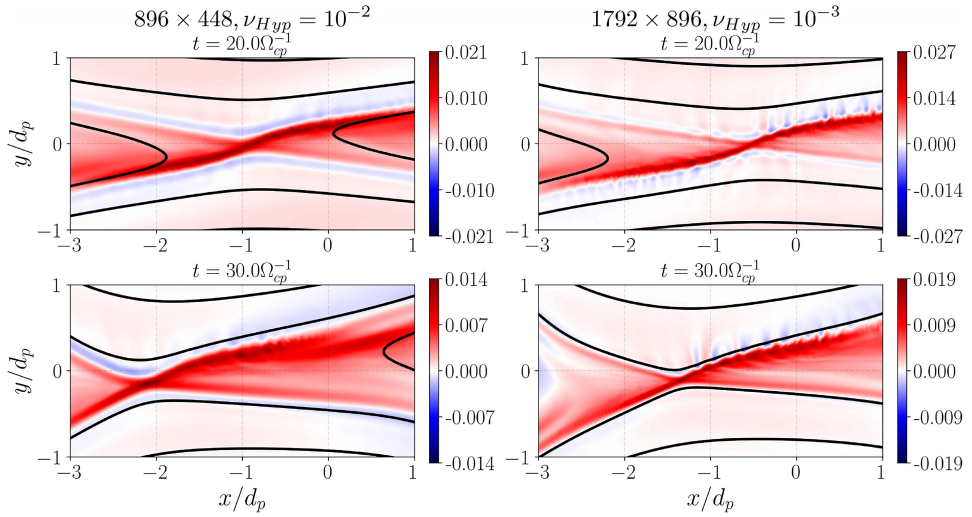


FIGURE 4. Zoom in of the $B_g = 0.5B_0$ simulation with lower resolution and larger hyperdiffusion (left), and higher resolution and smaller hyperdiffusion (right). While the mode is identifiable in the lower resolution simulation, the secondary instability is especially prominent at increased resolution.

896 \times 448 simulations for the two guide fields. Irrespective of the guide field, we observe the typical reconnection morphology from the thinning of the current layer: the magnetic field lines pinch towards a centrally located X point where the field is reconnecting, and the lower energy state of the field's rearranged topology leads to an acceleration of the plasma on either side of the X point. In fact, the $B_g = 0.5B_0$ simulation also seems to be developing a secondary instability in the current sheet, and we plot in figure 4 a zoom in of the current sheet at both the lower resolution, 896 \times 448, larger hyperdiffusion simulation and the higher resolution, 1792 \times 896, smaller hyperdiffusion simulation.

We draw particular attention to details of the reconnection morphology in figures 3 and 4, which are consistent with previous fully kinetic simulations of guide-field reconnection at realistic mass ratio: at a lower guide field the current layer is extended into the exhaust (Le *et al.* 2013). The explanation for this extended exhaust in the $B_g = 0.5B_0$ simulation compared with the more peaked current density in the $B_g = B_0$ simulation is identical to the physics of the fully kinetic simulations in Le *et al.* (2013), as we show in figure 5. While both simulations self-consistently develop a reasonably large temperature anisotropy in the layer, the temperature anisotropy in the lower guide field, $B_g = 0.5B_0$, simulation is large enough that, combined with the lower magnitude guide field, the magnetic tension at the X point is reduced, driving a large perpendicular current that broadens the layer into the exhaust, $\mathbf{J}_\perp \sim (p_\perp - p_\parallel) \nabla_\parallel \mathbf{b} \times \mathbf{B} / |\mathbf{B}|^2$, where $\nabla_\parallel = \mathbf{b} \cdot \nabla_x$. We observe that the electron parallel firehose criterion (Li & Habbal 2000)

$$\Lambda_{firehose} = 1 + \frac{\beta_{\parallel e}}{2} \left(\frac{T_{\perp e}}{T_{\parallel e}} - 1 \right), \quad (6.5)$$

where $\beta_{\parallel e} = 2\mu_0 n_e T_{\parallel e} / |\mathbf{B}|^2 = 2\mu_0 p_{\parallel e} / |\mathbf{B}|^2$ is the electron parallel plasma β , is much closer to marginal stability, $\Lambda_{firehose} \sim 0$ in the $B_g = 0.5B_0$ simulation. On the other

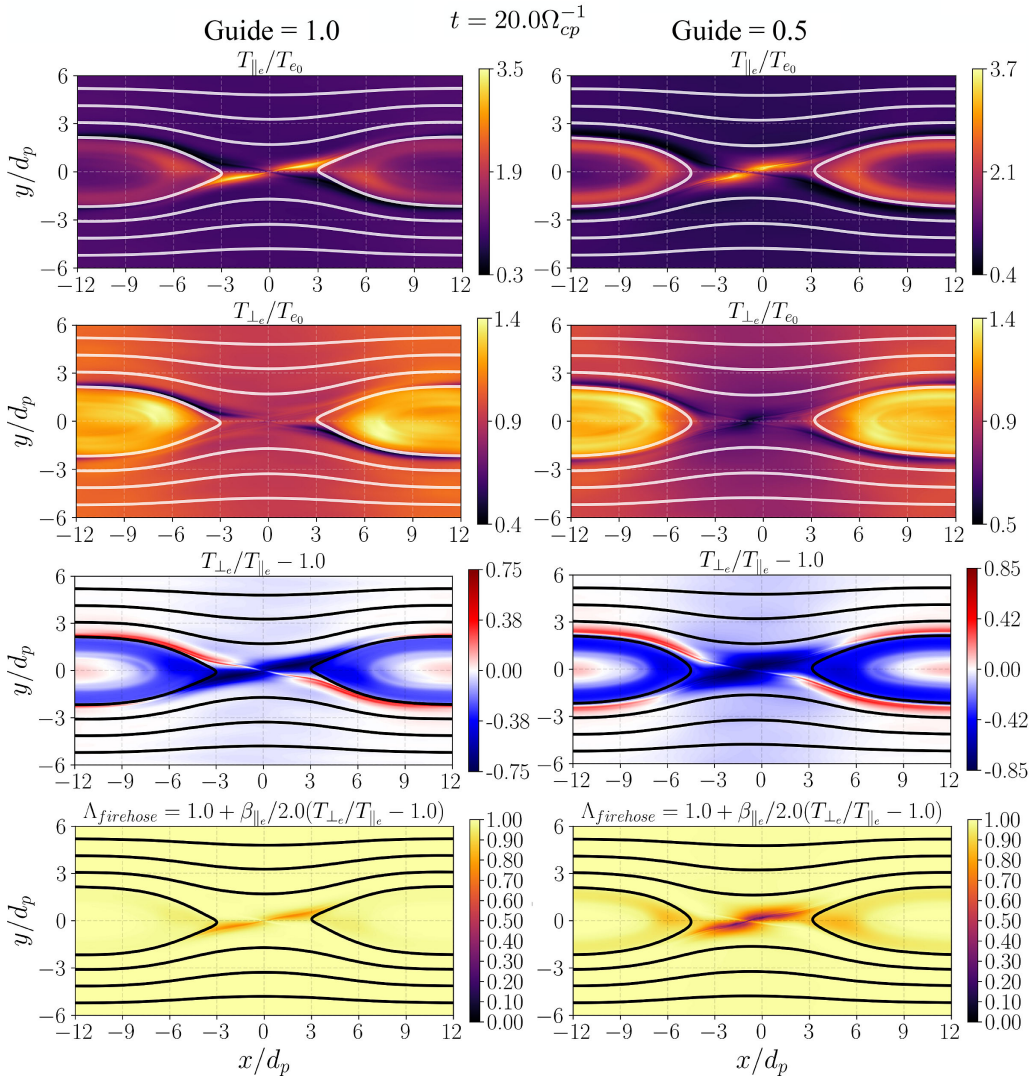


FIGURE 5. Comparison of the electron parallel temperature normalised to the initial electron temperature (top), electron perpendicular temperature normalised to the initial electron temperature (middle top), electron temperature anisotropy (middle bottom) and electron firehose criteria (bottom) at $t = 20\Omega_{ci}^{-1}$ for the $B_g = B_0$ simulation (left) and $B_g = 0.5B_0$ simulation (right). In both cases, a significant electron anisotropy from an excess of parallel pressure develops in the current layer, but a depletion of electron perpendicular pressure in the $B_g = 0.5B_0$ simulation further increases the electron anisotropy in the layer. Combined with the lower guide field and, thus, a weaker magnetic field at the X point, the electron firehose criteria is much closer to marginal stability $\Lambda_{firehose} \sim 0$ for the $B_g = 0.5B_0$ simulation. Thus, the electrons more significantly modify the tension in the magnetic field at the reconnecting X point compared with the higher guide-field simulation, driving a perpendicular current that spreads the current layer into the exhaust.

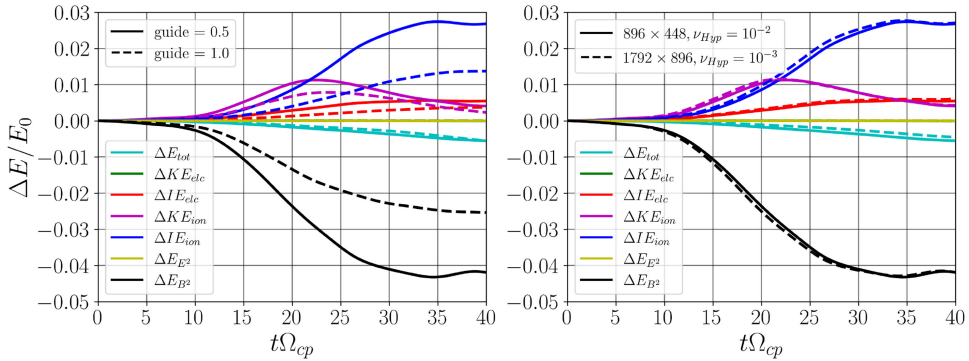


FIGURE 6. Evolution of the different components of the energy normalised to the total energy at $t = 0$ including the total kinetic energy, $\rho_s |\mathbf{u}_s|^2/2$, for the electrons and protons, the total internal energy, $3p_s/2 = p_{\parallel s}/2 + p_{\perp s}$, for the electrons and protons, the electric field energy, $\epsilon_0 |\mathbf{E}|^2/2$, and the magnetic field energy, $|\mathbf{B}|^2/2\mu_0$, comparing both different guide fields (left) and different resolutions for the $B_g = 0.5B_0$ simulation (right). We observe a conversion of magnetic energy into initially proton kinetic energy at the onset of magnetic reconnection, followed by heating of the plasma as both the electron and proton internal energies increase. Consistent with Shay *et al.* (2014), we observe that the overall electron internal energy increase is relatively insensitive to the guide-field strength, and consistent with Rowan *et al.* (2019), we observe that the relative heating of the protons versus the electrons is reduced at a larger guide field, as less magnetic energy is converted to plasma energisation in a stronger guide field for the moderate plasma β case considered here.

hand, the modest values observed in the $B_g = B_0$ simulation correspond to only minor modifications of the magnetic tension due to the electron anisotropy; the larger guide field is able to maintain the overall tension in the field in the exhaust.

The exact transition to this extended current layer when the firehose criterion becomes sufficiently small, but not necessarily unstable, is consistent with other studies that have examined the impact of proton pressure anisotropy on the overall magnetic field tension and the propagation of Alfvén waves in anisotropic plasmas (Bott *et al.* 2021, 2025). In these studies, an effective Alfvén speed must be defined, which decreases with increasing pressure anisotropy, corresponding to a reduced capability of the magnetic field to regulate the motion of a magnetised plasma and enhanced perpendicular transport, usually modelled as a Braginskii-like viscous stress (Squire *et al.* 2017b). In fact, at a lower guide field, we would likely observe an analogous phenomena to the nonlinear interruption of Alfvén waves (Squire, Quataert & Schekochihin 2016, 2017a), but from the electrons destabilising themselves due to the enhanced anisotropy in the extended layer. Such simulations could potentially extend the results of previous studies that have found the firehose criterion to be a constraint on the outflows in fully kinetic simulations of low guide-field reconnection (Haggerty *et al.* 2018) into regimes of even moderate guide field where, as we find, the electrons are still magnetised through the current layer. We emphasise though that, as with the results of the parallel electrostatic shock, at least the first Fourier harmonic would be required to approximate the FLR effects that govern the saturation of firehose modes.

We next examine the macroscopic evolution of these simulations, plotting the overall energy evolution and reconnection rate in figures 6 and 7, respectively, for different guide fields and resolutions. The energy evolution of these moderate

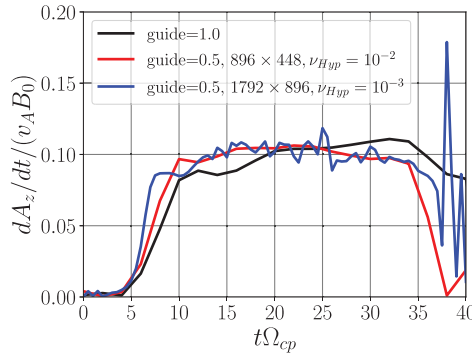


FIGURE 7. Reconnection rate as a function of time computed from the time rate of change of the out-of-plane vector potential, dA_z/dt , at the location of maximum parallel electric field, $E_{\parallel} = \mathbf{E} \cdot \mathbf{b}$. Regardless of resolution or guide field, we observe a steady peak value of ~ 0.1 in the standard normalised units dividing dA_z/dt by the initial, upstream in-plane magnetic field strength multiplied by the initial, upstream in-plane Alfvén speed (Shay *et al.* 1999; Liu *et al.* 2017; Cassak *et al.* 2017; Liu *et al.* 2022).

guide-field simulations is consistent with previous fully kinetic simulations: the overall heating of the electrons has only a weak dependence on guide-field strength (Shay *et al.* 2014), and as the guide-field strength increases, the amount of energy that the protons receive relative to the electrons decreases (Rowan, Sironi & Narayan 2019). The reconnection rate, computed as the time rate of change of the out-of-plane vector potential, dA_z/dt , at the location of the maximum parallel electric field, $E_{\parallel} = \mathbf{E} \cdot \mathbf{b}$, peaks at the expected normalised value of ~ 0.1 (Shay *et al.* 1999; Liu *et al.* 2017; Cassak, Liu & Shay 2017; Liu *et al.* 2022), where the normalisation is defined in the standard way to the initial upstream, in-plane magnetic field strength multiplied by the initial upstream, in-plane Alfvén velocity. Additionally, outside of a slightly faster reconnection onset in the higher resolution $B_g = 0.5B_0$ simulation, we find no sensitivity to our results with increasing resolution and lowering of the hyperdiffusion, suggesting that the kinetic response of the plasma is not modified by the hyperdiffusion model and the macroscopic dynamics of the reconnection are insensitive to this hyperdiffusion.

To further determine how accurately the PKPM model captures the kinetic response of the plasma at the X point, we can determine the physics of the out-of-plane electric field that governs the reconnection dynamics by rearranging the electron momentum equation:

$$E_z = \frac{m_e}{q_e} \left(\underbrace{\frac{\partial u_{ze}}{\partial t} + u_{xe} \frac{\partial u_{ze}}{\partial x} + u_{ye} \frac{\partial u_{ze}}{\partial y}}_{\text{Inertia}} + \frac{1}{\rho_e} \left[\frac{\partial P_{xze}}{\partial x} + \frac{\partial P_{yze}}{\partial y} \right] \right) - \underbrace{(u_{xe} B_y - u_{ye} B_x)}_{\text{Hall}}. \quad (6.6)$$

Here, we have labelled components of this generalised Ohm's law that correspond to the electron inertia and Hall terms (Vasyliunas 1975). Note that because the reconnection is fairly steady at $t = 20\Omega_{cp}^{-1}$ (see figure 7) we will ignore $\partial u_{ze}/\partial t$ in our analysis, as we expect this term to be small if the reconnection rate is relatively constant. We confirm in figures 8 and 9 the expected behaviour for this generalised

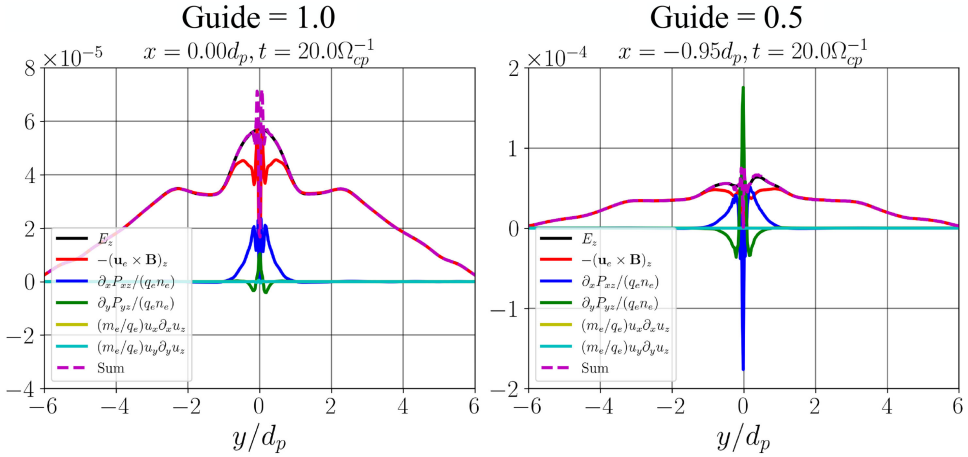


FIGURE 8. Comparison of the reconnecting electric field, E_z , and the individual components of the generalised Ohm's law (6.6) for the $B_g = B_0$ (left) and $B_g = 0.5B_0$ (right) simulations at $t = 20\Omega_{cp}^{-1}$ at a cut in x through the current sheet approximately where the current density peaks in figure 3. As expected, the Hall term supports the electric field away from the current sheet, but the Hall term goes to zero neat the X point where both u_{x_e} and u_{y_e} go to zero from the stagnation of the flow. The reconnecting electric field's dynamics is then governed by derivatives of the off-diagonal pressure tensor, which in this case is the gyrotropic electron pressure tensor. The combination of electron pressure anisotropy and the changing magnetic field geometry drive perpendicular currents that break the frozen-in condition as the electrons are no longer advecting with the magnetic field, thus allowing for the conversion of magnetic energy to plasma energy.

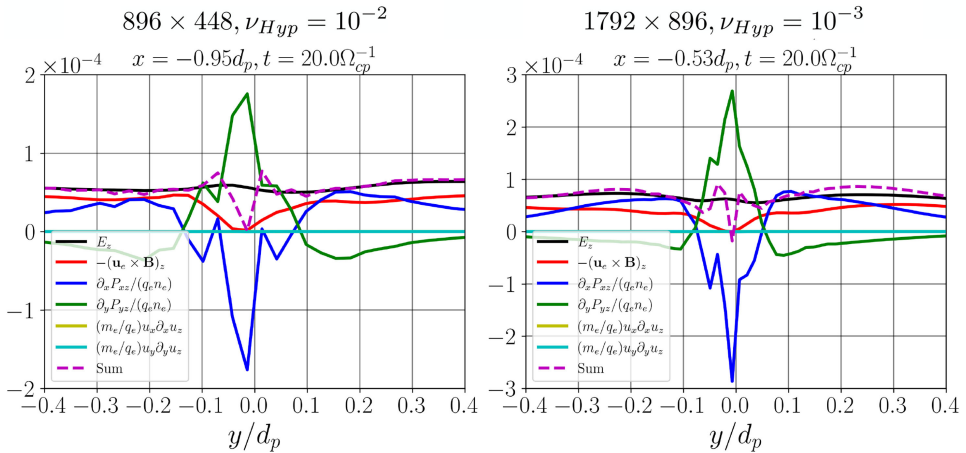


FIGURE 9. A zoom in of the $B_g = 0.5B_0$ simulations with lower resolution and larger hyperdiffusion (left), and higher resolution and lower hyperdiffusion (right). We note that the overall layer width is only marginally affected by resolution and hyperdiffusion, $\Delta \sim 0.2d_p \sim 8.5d_e$, where the proton and electron inertial lengths are defined with respect to the initial uniform density. The physics of the reconnecting electric field is completely unchanged qualitatively; the competition between $\partial_x P_{xz}$ and $\partial_y P_{yz}$ ultimately governs the reconnecting electric field evolution.

Ohm's law following the results of previous guide-field reconnection studies (Swisdak *et al.* 2005; Le *et al.* 2013; Egedal *et al.* 2013).

The electrons stay magnetised through the layer and, thus, provide the necessary support for the reconnection electric field through the electron's off-diagonal pressure tensor components, $P_{xz} = (p_{\parallel} - p_{\perp})b_x b_z$ and $P_{yz} = (p_{\parallel} - p_{\perp})b_y b_z$. In this case, the off-diagonal pressure tensor components that have historically been found to be the important components do not come from complex particle orbits but simply from the changing magnetic geometry and anisotropy of the electrons that develops as they stay magnetised through the layer.⁹ Instead of the fundamental agyrotropy that develops in the zero or low guide-field case (Hesse *et al.* 2018), it is the gyrotopic electron pressure tensor that can break the frozen-in condition (Egedal 2002). In other words, the electrons no longer simply advect with the magnetic field, but directly change the magnetic field due the perpendicular currents driven by the gyrotopic electron pressure tensor. We note that this change in the field driven by perpendicular currents is not necessarily true field line 'breaking'. [figure 9](#) shows that while the overall current sheet width is relatively insensitive to resolution and hyperdiffusion, there is a region in which the sum of these various components of Ohm's law and the reconnecting electric field diverge that does become smaller with increasing resolution. Thus, there is a region inside the current layer where the final field line topology changes, $b_x = b_y = 0$, which is not captured in the lowest-order PKPM model with no Fourier harmonics.

Importantly, while a number of fluid models have been developed to exploit this fact that electron anisotropy can break the frozen-in condition and determine the current sheet morphology (Le *et al.* 2009; Ohia *et al.* 2012; Cassak *et al.* 2015), we reiterate that this PKPM model employed here is fundamentally kinetic. The results of, e.g. how the electron anisotropy develops and affects the current sheet morphology are handled self-consistently without the need for any artificial limiters on the electron firehose condition (Ohia *et al.* 2015), and recent studies such as Walters *et al.* (2024) suggest that with only one or two Fourier harmonics, a self-consistent saturation of firehose modes can be included with this approach. As it is, we can clearly identify the impact of the kinetic physics by examining higher velocity moments than typically included in fluid models, such as the total parallel heat flux plotted in [figure 10](#) for electrons and protons, normalised to the initial thermal streaming values $\rho_s v_{ths}^3$, for the higher resolution, 1792×896 , $B_g = 0.5 B_0$ simulation at $t = 20\Omega_{cp}^{-1}$.

These heat fluxes are plotted componentwise so that we can separate the flow of T_{\parallel} due to q_{\parallel} and T_{\perp} due to q_{\perp} in the x versus y direction. These heat fluxes are not small compared with thermally streaming particles, especially q_{\parallel} for both the electrons and ions. In other words, these collisionless heat fluxes are likely strongly influencing the dynamical evolution of T_{\parallel} for each species. More importantly, $q_{\parallel e}$ and $q_{\perp e}$ are the opposite signs, towards the X point and away from the X point, respectively, in the extended current layer of this $B_g = 0.5 B_0$ simulation. These oppositely directed heat fluxes, in addition to the conservation of magnetic moment $\mu_e \propto T_{\perp e}/B$ in the layer where the electrons are magnetised, further explain why there is a cooling in $T_{\perp e}$ observed in [figure 5](#) and that this cooling is more pronounced in the lower guide-field case where the magnetic field strength decreases more at the X point. Thus, the

⁹We refer readers to Liu *et al.* (2025) for a recent review of Ohm's law analysis in simulations, laboratory experiments and spacecraft observations.

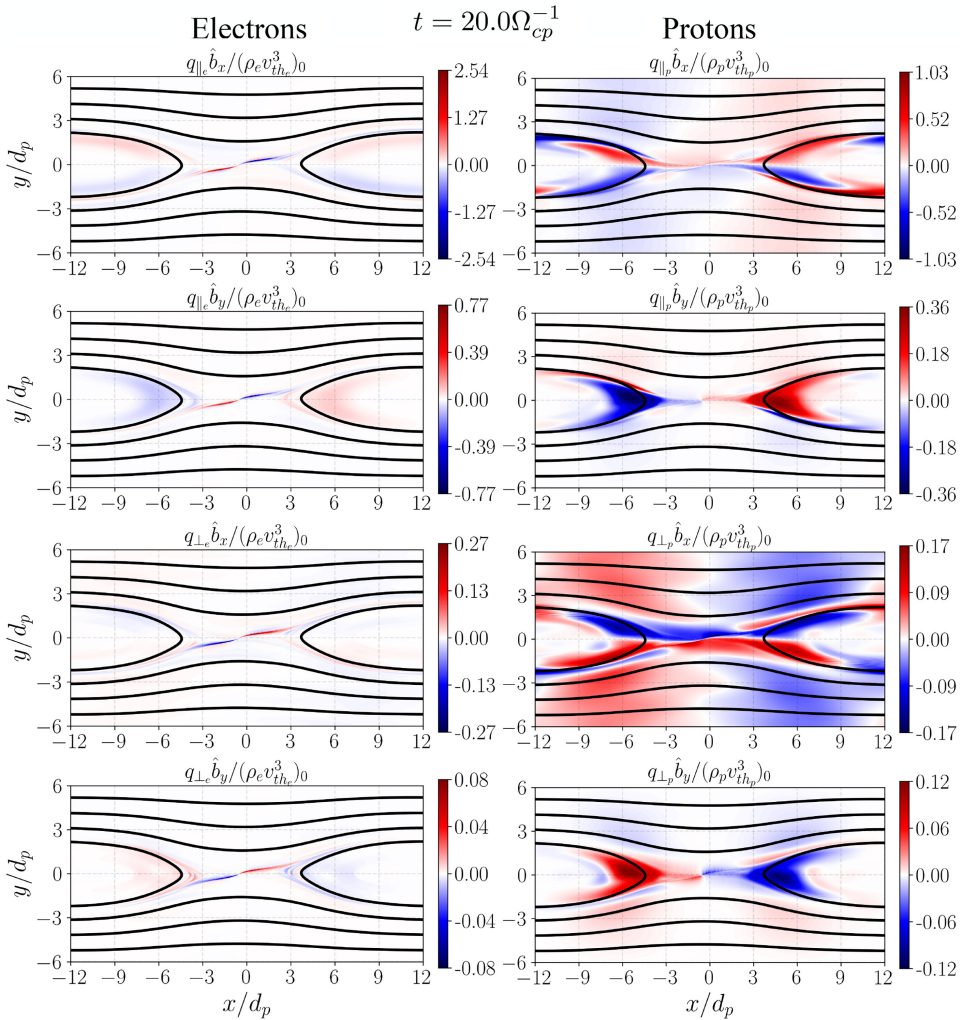


FIGURE 10. Comparison of the different components of the parallel heat flux normalised to the initial values of a thermally streaming plasma, $\rho_e v_{the}^3$, for both the electrons (left) and protons (right). We multiply both heat fluxes by the individual components of the magnetic field unit vector to separate the flow of T_{\parallel} due to q_{\parallel} and T_{\perp} due to q_{\perp} in the x versus y direction. We draw particular attention to how large the values of $q_{\parallel e}$ are, suggesting that the exact evolution of $T_{\parallel e}$ is strongly influenced by collisionless heat fluxes, and the fact that $q_{\parallel e}$ and $q_{\perp e}$ are the opposite sign in the current layer, which further explains the heightened temperature anisotropy in the $B_g = 0.5 B_0$ simulation. Furthermore, as large as the electron heat fluxes are, the ion heat fluxes compared with thermal streaming are not small either, with significant energy fluxes in the exhaust as the ions mix and heat in the outflows.

collisionless heat fluxes are enhancing the very temperature anisotropy in the layer that is modifying the tension in the magnetic field and driving the extended current layer.

In addition, at this same time of $t = 20 \Omega_{cp}^{-1}$, we plot in figure 11 the zoom in of the out-of-plane current density, now with superimposed vectors denoting the direction of the in-plane flow, to examine the secondary instability that we observed to be

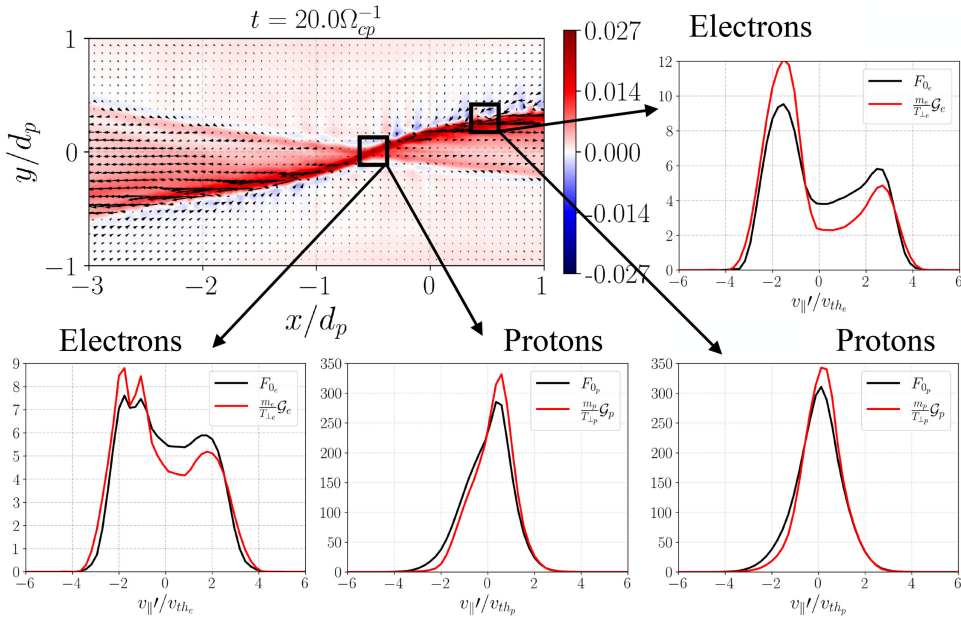


FIGURE 11. Zoomed-in out-of-plane current density for the $B_g = 0.5B_0$ simulation with superimposed vectors denoting the direction of the in-plane flow direction and corresponding plots of the electron and proton distribution functions at the peak of the current density and inside one of the excited fluctuations from the secondary instability in the extended current sheet. Note that the distribution functions are plotted in their respective flow frames, so the F_0 distribution functions have a zero first moment, and any skewness or multi-modality to the F_0 distribution functions are manifestations of heat fluxes or counter-streaming field-aligned flows. While we need the sign of the magnetic field unit vector to determine which direction the vector heat flux points, we can clearly identify from the overall structure of the electron's F_0 and \mathcal{G} distribution functions that $q_{||e}$ and $q_{\perp e}$ point in opposite directions, consistent with figure 10. In both cases, for the electrons, there is a depletion of F_0 relative to \mathcal{G} for negative $v'_{||}$ particles and an excess of F_0 relative to \mathcal{G} for positive $v'_{||}$ particles. Likewise, in the location of the excited secondary instability we have counter-streaming super-thermal beams along the field line, in addition to vortical structures in the in-plane flow velocity, which suggests that the electrons are unstable to a shearing instability. We identify this instability as the electron Kelvin–Helmholtz mode from its wavelength $kd_e \sim 1$ and its similarity to previous reconnection studies that excited secondary Kelvin–Helmholtz instabilities in the layer (Fermo *et al.* 2012).

developing in the extended current sheet in figure 4. We also show in figure 11 one-dimensional plots of the velocity distribution function within both the peak current density and one of the fluctuations of the secondary instability in the extended current layer. We identify this secondary instability now from its wavelength, $kd_e \sim 1$, the vortical structure present in the in-plane velocity, and the counter-streaming superthermal electron beams as the electron Kelvin–Helmholtz instability. This instability has been previously measured in fully kinetic simulations at a larger guide field, $B_g = 2B_0$, and lower proton–electron mass ratio, $m_p/m_e = 25$ (Fermo, Drake & Swisdak 2012). The exact conditions under which this Kelvin–Helmholtz instability can be excited are likely a consequence of both mass ratio and guide field, as the excitement of this secondary instability seems most prevalent in these extended

magnetised current layers and did not show up in the $B_g = B_0$ simulation with our chosen realistic proton–electron mass ratio.

The distribution function structure observed in this $B_g = 0.5B_0$ simulation includes a number of other interesting features. While we need the sign of the magnetic field unit vector to obtain the sign of the vector heat flux, the depletion of negative velocity particles in F_0 compared with \mathcal{G} , and likewise the excess of positive velocity particles in F_0 compared with \mathcal{G} , easily explains the fact that $q_{\parallel e}$ and $q_{\perp e}$ have the opposite sign in [figure 10](#). Furthermore, the broadened electron distribution function at the X point is consistent with trapped electron distribution functions in past studies of electron energisation in guide-field reconnection (Egedal *et al.* 2013). Finally, the proton distribution functions also show clearly how the protons develop non-trivial heat fluxes, even if these heat fluxes are appreciably smaller than the electron heat fluxes.

Thus, even with a moderate guide field, because the electrons stay magnetised through the layer, the PKPM model provides a powerful cost-effective tool for kinetic simulations of magnetic reconnection. Self-consistent temperature anisotropies and parallel heat fluxes can develop that modify the current layer morphology in agreement with previous fully kinetic simulations. Secondary instabilities that may be excited via field-aligned beams are likewise included in this approach. Given the sensitivity of the kinetic evolution of the electrons to the proton–electron mass ratio, the PKPM model may provide a breakthrough in understanding the dynamics of guide-field reconnection, even in regimes beyond which magnetised models such as gyrokinetics can be applied.

7. Summary

In this paper we have derived a novel approach to modelling kinetic plasmas based on classical intuition about collisionless, magnetised plasma dynamics. This PKPM model separates the parallel and perpendicular motion to the local magnetic field through the combination of coordinate transformations and optimised spectral expansions in these transformed coordinates. Via velocity space coordinate transformations to the Vlasov equation, first to velocity coordinates moving with the local flow and then to field-aligned velocity coordinates, we can reduce the number of degrees of freedom needed to model magnetised plasma with a truncated Laguerre–Fourier spectral expansion in the perpendicular velocity coordinates, both v_{\perp} and velocity gyroangle, θ . In this regard, the six-dimensional Vlasov–Maxwell dynamics were reduced to some number of four-dimensional equations for spectral coefficients in x, y, z configuration space and the remaining v_{\parallel} velocity coordinate, where the exact number of equations solved dictates the amount of perpendicular velocity space resolution one expects to need for the problem of interest.

The final equations, even in their simplest form where two kinetic equations for the zeroth Fourier harmonic and zeroth and first Laguerre coefficient are retained, contain a multitude of physics. While this lowest-order PKPM system only evolves the gyrotropic component of the distribution function, by virtue of how we constructed our Laguerre basis, we have significantly more flexibility than other spectral approaches to kinetic equations that discretise the untransformed Vlasov equation. Indeed, there are no assumptions made on the strength of the flow velocity or the variation of the perpendicular temperature; the PKPM model as implemented handles supersonic flows and large, $\mathcal{O}(1)$ variations in the perpendicular temperature as well as the resulting temperature anisotropies that develop self-consistently from

this perpendicular temperature variation. By transforming the velocity coordinates to the local flow frame, the restriction of a general shift vector in a spectral expansion is avoided, and we do not need to assume spatially or temporally independent background flows. By defining the second kinetic equation in terms of a linear combination of Laguerre coefficients, we can absorb the Laguerre normalisation into the second kinetic equation and avoid the need for an auxiliary equation for the perpendicular temperature.

We have demonstrated this flexibility and the underlying physics fidelity of the simplest PKPM model on two non-trivial, nonlinear problems: a parallel electrostatic collisionless shock and moderate guide-field reconnection. The PKPM model handles the transition between shocked and unshocked flows when the inflowing plasma sonic Mach number is sufficiently large that no nonlinear steepening of ion acoustic waves occurs to trap electrons. Likewise, the PKPM model correctly accounts for the impact of magnetised electrons in moderate guide-field reconnection, where electron pressure anisotropy can break the frozen-in condition for the electrons and convert the stored magnetic energy into plasma energy, both kinetic and internal. The uniqueness of the PKPM model is thus immediately apparent: to the authors' knowledge there are no implementations in any codes of asymptotic, magnetised, kinetic models that can handle supersonic flows or $\delta B/B \sim 1$ fluctuations. Yet the PKPM model is leveraging the same physics intuition that has informed these historical asymptotic models. For example, it is because the electrons continue to follow field lines, even if there is $\mathcal{O}(1)$ variation in the magnetic field, that the PKPM model compares favourably with past fully kinetic simulations of moderate guide-field reconnection, including the self-consistent generation of extended current layers due to the electrons reducing the field line tension via temperature anisotropy and driving macroscopic perpendicular currents.

We reiterate that this paper is but the first part of a multi-part series, as we have not yet discussed how we discretise even the simplest PKPM model with a DG finite element method. Preserving the properties of the continuous PKPM system, most especially minimising errors in the conservation of energy from the coupling of the bulk kinetic energy from the momentum equation with the evolution of the internal energy given by the kinetic equations, are non-trivial endeavours, and for maximum clarity of the narrative, we have elected to separate the theoretical and numerical discussions. Still, we emphasise the demonstration of the PKPM model in § 6 is not only meant to communicate the physics fidelity of the PKPM model, but the successful numerical implementation of this unique hybrid discretisation strategy mixing a Laguerre–Fourier spectral expansion with DG. Indeed, while philosophically similar hybrid discretisations using a combination of spherical harmonics and DG in ‘test-fluid’ approaches that do not feedback on the flow velocity and magnetic field evolution have been derived and implemented (Schween & Reville 2024; Schween *et al.* 2025), the demonstration of the PKPM model is the first use of this kind of hybrid discretisation utilising an optimised Laguerre–Fourier spectral basis for magnetised plasma dynamics.

The successful numerical implementation and demonstration of the PKPM model here is also in one respect the culmination of the theoretical work that inspired the PKPM approach, but has resisted easy numerical discretisation. Kinetic magneto-hydrodynamics (Kulsrud 1964, 1983) and FLR kinetic theory (Ramos 2008, 2016) both transform the velocity coordinates of the Vlasov equation to velocity coordinates that are both field aligned and moving at a local flow velocity, the $\mathbf{E} \times \mathbf{B}$ velocity in the case of KMHD and the total flow velocity in the case of FLR kinetic

theory. However, the stiff constraint equations that these models derive, such as the E_{\parallel} equation in KMHD, may not be satisfied at any given instant in time if one evolves kinetic equations for each individual plasma species that thus generate non-zero parallel currents. Therefore, while there have been recent successes in KMHD-like approaches that leverage physics intuition and add fluid equations that instantaneously satisfy equilibrium relations, such as cold electron return currents that balance the currents driven by the kinetic species (Drake *et al.* 2019; Arnold *et al.* 2019, 2021, 2022), the PKPM model self-consistently handles the relaxation to these constraint equations by dynamically evolving, e.g. parallel currents. As a result, in simulations of phenomena such as magnetic reconnection, the distribution functions naturally develop distinct particle populations that can then evolve to states predicted by these asymptotic models, or on the other hand, drive secondary instabilities from these counter-streaming kinetic populations.

We emphasise at this stage that this paper constitutes only the beginning of a larger program of research with this PKPM model. A systematic convergence study in Laguerre resolution of subcritical collisionless shocks, guide-field reconnection or other phenomenon such as turbulence and transport in laboratory and astrophysical plasmas, is of immediate interest. For example, how accurately this optimised Laguerre basis in v_{\perp} resolves the loss cone of a magnetic mirror across a range of mirror force strengths will inform rules of thumb of how many Laguerre spectral coefficients are needed for a variety of applications. Furthermore, there will likely be cases in which the amount of Laguerre resolution needed for the physics of interest is different in different regions of configuration space, and may even be different per-species. We can thus imagine further optimisation of this approach to refine our perpendicular resolution only where we need it. And in cases where one plasma species may be poorly modelled by the PKPM approach, such as in a high-Mach-number collisionless shock where we often observe the protons to be highly agyrotropic due to reflection off the compressed magnetic field while we observe that the electrons stay mostly gyrotropic through the shock, significant computational gains could still be realised by a flexible coupling of the full Vlasov model in Gkeyll (Juno *et al.* 2018; Hakim & Juno 2020) to the PKPM model presented here.

Perhaps most important for examining the physics fidelity of the PKPM model as more perpendicular moments are added is the impact of the Fourier harmonics on the model. As we showed in § 4 with (4.19) and discussed in § 6, the first two Fourier harmonics give the self-consistent evolution of the remaining off-diagonal pressure tensor components, in addition to other higher moments such as the heat fluxes perpendicular to the field. Indeed, the fact that adding only one or two Fourier harmonics confers this increased physics is a direct consequence of the fact that this approach does not transform to gyrocentre coordinates and instead keeps the configuration space coordinates at the particle position. Adding a few Fourier harmonics thus allows the PKPM model to directly connect to the success of multi-fluid models that include the full pressure tensor (Wang *et al.* 2015; Ng *et al.* 2015; Wang *et al.* 2018; Dong *et al.* 2019; Ng *et al.* 2019; TenBarge *et al.* 2019; Allmann-Rahn *et al.* 2021; Walters *et al.* 2024; Kuldinow *et al.* 2024a). With just a few more equations, we would obtain a hybrid fluid-kinetic approach with all of the higher-order fluid effects of the cutting edge of extended fluid modelling for the dynamics perpendicular to the local magnetic field, with a complete kinetic description parallel to the field capable of handling a myriad of kinetic phenomena: parallel heat fluxes, field-aligned beams, trapped particles and more.

In fact, we consider it likely that the inclusion of the first one or two Fourier harmonics to be not just a sweet spot in terms of the physics fidelity of this reduced approach, but optimal computationally as well. The evolution of the first two Fourier harmonics can be encoded in the evolution of the vector \mathbf{M}_\perp and tensor $\mathbf{F}_{\perp\perp}$, given by (4.6) and (4.10), respectively, and the evolution of these quantities can be determined by multiplying the Vlasov equation in our transformed coordinates, (3.29), by \mathbf{v}_\perp and $\mathbf{v}_\perp \otimes \mathbf{v}_\perp$ and integrating over the velocity gyroangle. These evolution equations for \mathbf{M}_\perp and tensor $\mathbf{F}_{\perp\perp}$ could then be expanded in our Laguerre basis in v_\perp . So, for example, a ‘lowest-order’ approach that was extended to the first Fourier harmonic through the \mathbf{M}_\perp equation would go from solving kinetic equations for F_0 and \mathcal{G} to include $\mathbf{M}_{\perp 0}$ and $\mathcal{N}_\perp = T_\perp/m(\mathbf{M}_{\perp 0} - \mathbf{M}_{\perp 1})$, where $\mathbf{M}_{\perp 0,1}$ are the zeroth and first Laguerre coefficients of \mathbf{M}_\perp , respectively, and \mathcal{N}_\perp is the linear combination of the first and zeroth Laguerre coefficients that would appear similar to the \mathcal{G} term in our PKPM expansion – a modest increase from two total kinetic equations to eight total kinetic equations. Higher Fourier harmonics could become burdensome to represent as tensors of increasing rank, especially in combination with the Laguerre expansion in v_\perp , and we defer a careful examination of computational efficiency and physics fidelity with increasing Fourier harmonics and Laguerre coefficients to future work.

Even still, the utility of the PKPM approach has already been demonstrated in studies as diverse as the feasibility of novel fusion configurations that require collisionless shock generation to compress the target fuel (Cagas *et al.* 2023), to novel energisation studies of electromagnetic waves that utilise the PKPM perspective to understand how different kinetic populations of particles ultimately lead to heating via ‘pressure work’ (Conley *et al.* 2024). Furthermore, the success of the PKPM model in modelling moderate guide-field reconnection with a realistic proton–electron mass ratio suggests it is an ideal model for kinetic studies of new reconnection regimes, such as shear-flow suppression of the tearing mode (Mallet *et al.* 2025*b,a*). With the necessary modifications to the PKPM model to solve the equations in curvilinear coordinates, further direct modelling of fusion reactor geometries could be performed as well. Given recent discoveries in the importance of kinetic effects as reactor-relevant temperatures are simulated (Shukla *et al.* 2025), we may yet find benefit in transport and macrostability modelling with this approach for self-consistent simulations all the way to the plasma-material interface, where the fact that this model includes the physics of the plasma sheath will allow for more detailed analysis of the heat deposition on the plasma-facing components. We conclude that the PKPM model derived in this paper has widespread applicability and its cost effectiveness in even its simplest form presents unique opportunities for modelling diverse weakly collisional, magnetised plasma systems.

Acknowledgements

The authors thank the Gkeyll team for useful discussions and wish to especially thank P. Cagas for assistance in plotting distribution functions from PKPM data. J. Juno acknowledges A. Philippov for insights from relativistic plasmas that motivated the PKPM approach, J. Chan for helpful conversations on discretising fluid equations with DG methods, and A. Hoffmann for useful discussions on spectral gyrokinetic solvers and Laguerre resolution. This research is part of the Frontera computing project at the Texas Advanced Computing Center. Frontera is made possible by National Science Foundation (NSF) Award OAC-1818253.

Editor Thierry Passot thanks the referees for their advice in evaluating this article.

Data availability

The input files for the Gkeyll simulations presented here are available in the following GitHub repository, <https://github.com/ammarrhakim/gkyl-paper-inp>. All plots in this paper utilise the postgkyl package <https://github.com/ammarrhakim/postgkyl>.

Funding

J. Juno, A. Hakim, J. M. TenBarge and the development of Gkeyll were partly funded by the NSF-CSSI program, Award No. 2209471. J. Juno and A. Hakim were also supported by the U.S. Department of Energy under Contract No. DE-AC02-09CH1146 via LDRD grants. J. M. TenBarge was also supported by NASA grant 80NSSC23K0099.

Declaration of interests

The authors report no conflict of interests.

Appendix A. Coordinate-free tensor notation

Throughout this paper we have used a coordinate-free notation based on an extended form of the notation adopted in Thorne & Blanford (2017). In this appendix we present an overview of our notation for ease of following the derivations in the main text of the paper.

We work in flat three-dimensional space and denote the vector space as \mathcal{V} . Given two or more vectors in \mathcal{V} , we denote their tensor product with the \otimes symbol. For example, given $\mathbf{u}, \mathbf{v} \in \mathcal{V}$, we can write their tensor product as $\mathbf{u} \otimes \mathbf{v}$. The tensor product creates a multilinear mapping from n vectors, where n is the number of vectors in the product, to a real number. Given $\mathbf{u} \otimes \mathbf{v}$, the mapping is $\mathbf{u} \otimes \mathbf{v} : \mathcal{V} \times \mathcal{V} \rightarrow \mathbb{R}$, and we can evaluate it for the vectors \mathbf{a} and \mathbf{b} as

$$(\mathbf{u} \otimes \mathbf{v})(\mathbf{a}, \mathbf{b}) = (\mathbf{u} \cdot \mathbf{a})(\mathbf{v} \cdot \mathbf{b}). \quad (\text{A.1})$$

A tensor of rank n is a multilinear function that takes n vectors and maps them to a real number. For example, a second-order tensor $\mathbf{T}(\mathbf{a}, \mathbf{b})$ will take two input vectors (\mathbf{a} and \mathbf{b} in this case) and produce a single scalar. As the mapping is multilinear, we have

$$\mathbf{T}(\alpha \mathbf{a} + \delta \mathbf{d}, \mathbf{b}) = \alpha \mathbf{T}(\mathbf{a}, \mathbf{b}) + \delta \mathbf{T}(\mathbf{d}, \mathbf{b}). \quad (\text{A.2})$$

In this sense, a scalar is a rank-0 tensor, that simply evaluates to itself. A vector \mathbf{u} is a rank-1 tensor mapping an input vector \mathbf{a} to

$$\mathbf{u}(\mathbf{a}) = \mathbf{u} \cdot \mathbf{a}. \quad (\text{A.3})$$

Defined in this manner, rank- n tensors (including vectors) are geometric quantities, hence, independent of the basis vectors used to represent them.

We can introduce a set of basis vectors \mathbf{e}_i , $i = 1, 2, 3$, for \mathcal{V} . These basis vectors need not be orthogonal (or even unit) vectors. Given these basis vectors, we can construct a set of dual basis \mathbf{e}^i defined such that $\mathbf{e}_i \cdot \mathbf{e}^j = \delta_i^j$. In flat space we can always introduce a set of orthonormal basis $\boldsymbol{\sigma}_i$, with $i = 1, 2, 3$. These orthonormal basis are their own duals.

Now, if we feed a vector with one of the basis \mathbf{e}_i or \mathbf{e}^i , we get

$$\mathbf{u}(\mathbf{e}_i) = \mathbf{u} \cdot \mathbf{e}_i \equiv u_i, \quad (\text{A.4})$$

$$\mathbf{u}(\mathbf{e}^i) = \mathbf{u} \cdot \mathbf{e}^i \equiv u^i. \quad (\text{A.5})$$

Hence, with the basis as an input, the vector mapping produces the component of the vector along that basis. Analogously, we define the components of a higher rank tensor as the real numbers produced when the input vectors are the basis. So

$$T_{ij} \equiv \mathbf{T}(\mathbf{e}_i, \mathbf{e}_j), \quad (\text{A.6})$$

$$T^{ij} \equiv \mathbf{T}(\mathbf{e}^i, \mathbf{e}^j). \quad (\text{A.7})$$

Since tensors are multilinear mappings, in a specific basis, we can write them as linear combinations of the tensor products of the selected basis. For example,

$$\mathbf{T} = T^{ij} \mathbf{e}_i \otimes \mathbf{e}_j = \mathbf{T}(\mathbf{e}^i, \mathbf{e}^j) \mathbf{e}_i \otimes \mathbf{e}_j = T_{ij} \mathbf{e}^i \otimes \mathbf{e}^j = \mathbf{T}(\mathbf{e}_i, \mathbf{e}_j) \mathbf{e}^i \otimes \mathbf{e}^j. \quad (\text{A.8})$$

Hence, using the components, we can write an explicit formula for the evaluation of the multilinear form in terms of its components as

$$\mathbf{T}(\mathbf{a}, \mathbf{b}) = T^{ij} (\mathbf{a} \cdot \mathbf{e}_i) (\mathbf{b} \cdot \mathbf{e}_j) = T^{ij} a_i b_j = T_{ij} (\mathbf{a} \cdot \mathbf{e}^i) (\mathbf{b} \cdot \mathbf{e}^j) = T_{ij} a^i b^j. \quad (\text{A.9})$$

Note that throughout we are using the Einstein summation convention: repeated upstairs/downstairs indices are to be summed.

We can also compute the partial evaluation of the tensor by filling up one or more of its slots with vectors. The resulting function (taking fewer input parameters) is also a tensor, but a lower rank tensor. For example $\mathbf{T}(\mathbf{a}, _)$ results in a vector (rank-1 tensor). In a specific representation,

$$\mathbf{T}(\mathbf{a}, _) = T^{ij} \mathbf{a} \cdot (\breve{\mathbf{e}}_i \otimes \mathbf{e}_j) = T^{ij} (\mathbf{a} \cdot \mathbf{e}_i) \mathbf{e}_j, \quad (\text{A.10})$$

where we have used the ‘breve’ marker on the \mathbf{e}_i to indicate with which of the vectors making up the tensor product the dot product must be taken. Similarly,

$$\mathbf{T}(_, \mathbf{a}) = T^{ij} \mathbf{a} \cdot (\mathbf{e}_i \otimes \breve{\mathbf{e}}_j) = T^{ij} \mathbf{e}_i (\mathbf{a} \cdot \mathbf{e}_j). \quad (\text{A.11})$$

Of course, we do not need to use the tangent or their reciprocals to represent tensors. As they are geometric objects, any basis will do, for example, the normalised tangent vectors. Once the components are known in one set of basis, we can simply compute them in another basis by evaluating, for example,

$$\mathbf{T}(\hat{\mathbf{e}}_i, \hat{\mathbf{e}}_j) \equiv \hat{T}_{ij} = T_{mn} (\hat{\mathbf{e}}_i \cdot \mathbf{e}^m) (\hat{\mathbf{e}}_j \cdot \mathbf{e}^n). \quad (\text{A.12})$$

The trace of a tensor product is a linear operator defined as, for example,

$$\text{Tr}(\mathbf{u} \otimes \mathbf{v}) \equiv \mathbf{u} \cdot \mathbf{v}. \quad (\text{A.13})$$

For products with more than two vectors, we need to indicate the pair of vectors on which the trace operator acts. For example,

$$\text{Tr}(\breve{\mathbf{u}} \otimes \mathbf{v} \otimes \breve{\mathbf{w}}) = (\mathbf{u} \cdot \mathbf{w}) \mathbf{v}. \quad (\text{A.14})$$

Here, we used the ‘breve’ marker on the vectors we wish to participate in the trace. Just like partial evaluation, the trace operator is also a rank reducing operation: the resulting object has two ranks lower than the original tensor.

The dot-product operator can be extended to act on a pair of tensors. To define this operation, consider we want to compute the dot product between a vector \mathbf{u} and a second-order tensor \mathbf{T} . We first need to select the slot of the tensor with which we wish to take the product. For example, we denote the dot product with the first slot as $\mathbf{u} \cdot \mathbf{T}(_, _)$ and define this to be just the partial evaluation $\mathbf{T}(\mathbf{u}, _)$. Similarly, $\mathbf{u} \cdot \mathbf{T}(_, _) = \mathbf{T}(_, \mathbf{u})$.

The metric tensor is a special bilinear mapping

$$\mathbf{g}(\mathbf{a}, \mathbf{b}) = \mathbf{a} \cdot \mathbf{b}. \quad (\text{A.15})$$

From this definition, we see that the partial evaluation of the metric tensor is particularly simple:

$$\mathbf{a} \cdot \mathbf{g}(_, _) = \mathbf{g}(\mathbf{a}, _) = \mathbf{a}. \quad (\text{A.16})$$

We can compute the components of the metric tensor as

$$\mathbf{g}(\mathbf{e}_i, \mathbf{e}_j) = \mathbf{e}_i \cdot \mathbf{e}_j \equiv g_{ij}, \quad (\text{A.17})$$

$$\mathbf{g}(\mathbf{e}^i, \mathbf{e}^j) = \mathbf{e}^i \cdot \mathbf{e}^j \equiv g^{ij}. \quad (\text{A.18})$$

There are two useful alternative expressions for the metric tensor: first in terms of the basis and their duals as

$$\mathbf{g} = \mathbf{e}_i \otimes \mathbf{e}^i = \mathbf{e}^i \otimes \mathbf{e}_i; \quad (\text{A.19})$$

and the second useful expression is

$$\mathbf{g} = \nabla \otimes \mathbf{x}, \quad (\text{A.20})$$

where ∇ is the vector derivative operator and \mathbf{x} is the position vector in space. Note that all these expressions are independent of dimensions and applicable to not just three-dimensional space. These expressions also show that, for Euclidean space,

$$\text{Tr}(\mathbf{g}) = \sum_{i=1}^D \mathbf{e}_i \cdot \mathbf{e}^i = \sum_{i=1}^D \delta_i^i = D, \quad (\text{A.21})$$

where D is the dimension of the space.

Now consider any vector \mathbf{u} and write

$$u^i = \mathbf{u} \cdot \mathbf{e}^i = (\mathbf{u} \cdot \mathbf{e}_j)(\mathbf{e}^j \cdot \mathbf{e}^i) = g^{ij} u_j. \quad (\text{A.22})$$

Similarly, we have

$$u_i = \mathbf{u} \cdot \mathbf{e}_i = (\mathbf{u} \cdot \mathbf{e}^j)(\mathbf{e}_j \cdot \mathbf{e}_i) = g_{ij} u^j. \quad (\text{A.23})$$

This process is sometimes called raising and lowering of indices, and extends to tensors of any rank. In fact, we can also easily show that

$$\mathbf{e}^i = g^{ij} \mathbf{e}_j, \quad (\text{A.24})$$

$$\mathbf{e}_i = g_{ij} \mathbf{e}^j. \quad (\text{A.25})$$

These expressions are useful to replace the basis vectors for their reciprocals (and *vice versa*).

Note that we must distinguish between a tensor \mathbf{T} , its definition, for example, $\mathbf{T} = \mathbf{u} \otimes \mathbf{v}$, and its evaluation $\mathbf{T}(\mathbf{a}, \mathbf{b})$. It is helpful to think of tensors as functions in a programming language: there, also one must distinguish between the name, the definition, and its evaluation.

Finally, we remark that tensors are a very special, but important, class amongst general scalar-valued functions. In general, an arbitrary function $f: \mathcal{V} \rightarrow \mathbb{R}$ need not be linear. For example, $f(\mathbf{u}) = \mathbf{u} \cdot \mathbf{u}$ is a quadratic function of its input vector and, hence, is not a tensor.

Second-order tensors, also called dyads, appear frequently in mathematical physics. We define a dyadic product as follows. Let \mathbf{T} be a second-order tensor and \mathbf{u} and \mathbf{v} be vectors. Then the dyadic product is denoted by the ‘ \otimes ’ symbol and is defined as

$$\mathbf{T} : \mathbf{u} \otimes \mathbf{v} \equiv \mathbf{T}(\mathbf{u}, \mathbf{v}). \quad (\text{A.26})$$

In particular, if $\mathbf{T} = \mathbf{a} \otimes \mathbf{b}$ then

$$\mathbf{a} \otimes \mathbf{b} : \mathbf{u} \otimes \mathbf{v} = (\mathbf{a} \cdot \mathbf{u})(\mathbf{b} \cdot \mathbf{v}). \quad (\text{A.27})$$

Now, let \mathbf{T} and \mathbf{G} be two dyads. Then the above definitions can be used to write the dyadic product in term of the dyad representation in a particular basis as

$$\mathbf{T} : \mathbf{G} = \mathbf{T} : G_{ij} \mathbf{e}^i \otimes \mathbf{e}^j = \mathbf{T}(\mathbf{e}^i, \mathbf{e}^j) G_{ij} = T^{ij} G_{ij}. \quad (\text{A.28})$$

This operation also shows that $\mathbf{T} : \mathbf{G} = \mathbf{G} : \mathbf{T}$. The dyadic product is a rank reducing operator: it takes two second-order tensors and produces a scalar.

From the definitions, we can also see that the dyadic product with the metric tensor is particularly simple:

$$\mathbf{g} : \mathbf{T} = \text{Tr}(\mathbf{T}). \quad (\text{A.29})$$

From this result, it follows that $\mathbf{g} : \mathbf{g} = D$, where, as defined before, D is the dimension of the space.

Besides the dot product (valid in a space of any dimension), we can also define the cross-product in three dimensions as follow. The cross-product of two vectors is denoted by $\mathbf{b} \times \mathbf{c}$ and results in a vector. Here we consider a different approach to the cross-product by defining a third-order tensor $\boldsymbol{\varepsilon}(\mathbf{a}, \mathbf{b}, \mathbf{c})$ as

$$\boldsymbol{\varepsilon}(\mathbf{a}, \mathbf{b}, \mathbf{c}) = \mathbf{a} \cdot (\mathbf{b} \times \mathbf{c}). \quad (\text{A.30})$$

The partial evaluation of this tensor with two of its slots filled gives

$$\boldsymbol{\varepsilon}(_, \mathbf{b}, \mathbf{c}) = \mathbf{b} \times \mathbf{c}, \quad (\text{A.31})$$

that is, the resulting vector has the same components as the cross-product of \mathbf{b} and \mathbf{c} . Hence, the second-order tensor that results from filling in the last slot, $\boldsymbol{\varepsilon}(_, _, \mathbf{c})$, has the property that

$$\mathbf{b} \cdot \boldsymbol{\varepsilon}(_, _, \mathbf{c}) = \boldsymbol{\varepsilon}(_, \mathbf{b}, \mathbf{c}) = \mathbf{b} \times \mathbf{c}. \quad (\text{A.32})$$

We have thus written the cross-product as a dot product between a vector and a special second-order tensor. As with the dot product, we can take the cross-product

between tensors. For example, consider the cross-product between a vector \mathbf{u} and a second-order tensor $\mathbf{a} \otimes \mathbf{b}$. We need to specify which of the vectors making up the second-order tensor we wish to cross. For example,

$$\mathbf{u} \times (\check{\mathbf{a}} \otimes \mathbf{b}) = (\mathbf{u} \times \mathbf{a}) \otimes \mathbf{b} \quad (\text{A.33})$$

is the cross-product with the first slot of the tensor and

$$\mathbf{u} \times (\mathbf{a} \otimes \check{\mathbf{b}}) = \mathbf{a} \otimes (\mathbf{u} \times \mathbf{b}) \quad (\text{A.34})$$

is the cross-product with the second slot of the tensor. Applying this operation to a general second-order tensor \mathbf{P} , we can write

$$\mathbf{u} \times \mathbf{P}(\check{},) = P^{mn}(\mathbf{u} \times \mathbf{e}_m) \otimes \mathbf{e}_n. \quad (\text{A.35})$$

Note that the cross-product of a vector with a second-order tensor is a second-order tensor. If \mathbf{P} is symmetric then the second-order tensor

$$\mathbf{u} \times \mathbf{P}(\check{},) + \mathbf{u} \times \mathbf{P}(, \check{}) \quad (\text{A.36})$$

is also symmetric.

Appendix B. Useful relations for Laguerre polynomials

We use normalised Laguerre polynomials, for which the orthogonality relation is

$$\int_0^\infty e^{-x} L_n(x) L_m(x) dx = \delta_{nm}. \quad (\text{B.1})$$

The first few Laguerre polynomials are

$$L_0(x) = 1, \quad (\text{B.2})$$

$$L_1(x) = 1 - x, \quad (\text{B.3})$$

$$L_2(x) = \frac{x^2}{2} - 2x + 1. \quad (\text{B.4})$$

A useful relation is

$$x \frac{dL_n}{dx} = nL_n(x) - nL_{n-1}(x). \quad (\text{B.5})$$

The recurrence relation for the polynomial is

$$(n+1)L_{n+1}(x) = (2n+1-x)L_n(x) - nL_{n-1}(x). \quad (\text{B.6})$$

Appendix C. The agyrotropic terms in the evolution of the gyrotropic distribution function

For completeness, we list below the agyrotropic terms in the evolution of the gyrotropic distribution function. These terms are denoted by AG in (4.15). One would need to include these terms to add the effects of agyrotropy in the lowest-order PKPM system. However, we note that in the examples given in this paper,

we do not include these terms, leaving the implementation of these terms for future work. We have

$$\mathbf{AG} = \nabla_x \cdot \mathbf{M}_\perp + \frac{1}{v_\perp} \frac{\partial}{\partial v_\parallel} \left(v_\perp \frac{1}{2\pi} \int_0^{2\pi} a_a^\parallel \bar{f} d\theta \right) + \frac{1}{v_\perp} \frac{\partial}{\partial v_\perp} \left(v_\perp \frac{1}{2\pi} \int_0^{2\pi} a_a^\perp \bar{f} d\theta \right). \quad (\text{C.1})$$

Here, we have defined

$$\begin{aligned} \frac{1}{2\pi} \int_0^{2\pi} a_a^\parallel \bar{f} d\theta &= \mathbf{M}_\perp \cdot \left[\frac{\partial \mathbf{b}}{\partial t} + (v_\parallel \mathbf{b} + \mathbf{u}) \cdot \nabla_x \mathbf{b} \right] - \mathbf{b} \cdot [\mathbf{M}_\perp \cdot \nabla_x \mathbf{u}] \\ &\quad - \frac{v_\perp^2 \bar{f}_2^c}{4} \mathbf{b} \cdot (\boldsymbol{\tau}_1 \cdot \nabla \boldsymbol{\tau}_1 - \boldsymbol{\tau}_2 \cdot \nabla \boldsymbol{\tau}_2) - \frac{v_\perp^2 \bar{f}_2^s}{4} \mathbf{b} \cdot (\boldsymbol{\tau}_1 \cdot \nabla \boldsymbol{\tau}_2 + \boldsymbol{\tau}_2 \cdot \nabla \boldsymbol{\tau}_1) \end{aligned} \quad (\text{C.2})$$

and

$$\begin{aligned} v_\perp \frac{1}{2\pi} \int_0^{2\pi} a_a^\perp \bar{f} d\theta &= \mathbf{M}_\perp \cdot \left[-v_\parallel \frac{\partial \mathbf{b}}{\partial t} - v_\parallel (v_\parallel \mathbf{b} + \mathbf{u}) \cdot \nabla_x \mathbf{b} + \frac{1}{\rho} \nabla_x \cdot \mathbf{P} - v_\parallel \mathbf{b} \cdot \nabla_x \mathbf{u} \right] \\ &\quad - \left[\frac{v_\perp^2 \bar{f}_2^c}{4} (\boldsymbol{\tau}_1 \otimes \boldsymbol{\tau}_1 - \boldsymbol{\tau}_2 \otimes \boldsymbol{\tau}_2) + \frac{v_\perp^2 \bar{f}_2^s}{4} (\boldsymbol{\tau}_1 \otimes \boldsymbol{\tau}_2 + \boldsymbol{\tau}_2 \otimes \boldsymbol{\tau}_1) \right] \\ &\quad : (v_\parallel \nabla_x \otimes \mathbf{b} + \nabla_x \otimes \mathbf{u}). \end{aligned} \quad (\text{C.3})$$

Note that the first two Fourier harmonics appear in the agyrotropic terms. Hence, to get the lowest-order agyrotropic effects, we would need to evolve additional equations, one for each of the $f_{1,2}^{s,c}$ along with evolution equations for the plane perpendicular to the magnetic field through $\boldsymbol{\tau}_1$ and $\boldsymbol{\tau}_2$. Alternatively, as we argue in the main text, we could evolve a vector equation for \mathbf{M}_\perp and tensor equation for $\mathbf{F}_{\perp\perp}$ to fold in the evolution of $\boldsymbol{\tau}_1$ and $\boldsymbol{\tau}_2$ directly into the evolved quantities. The procedure for obtaining equations for \mathbf{M}_\perp and $\mathbf{F}_{\perp\perp}$ would involve multiplying the Vlasov equation in our transformed coordinates, (3.29), by \mathbf{v}_\perp and $\mathbf{v}_\perp \otimes \mathbf{v}_\perp$ and integrating over the velocity gyroangle. These evolution equations for \mathbf{M}_\perp and $\mathbf{F}_{\perp\perp}$ could then be further expanded in the Laguerre basis in v_\perp to obtain the final coupled system of equations.

Appendix D. The PKPM Dougherty collision operator

For the simulations shown here, we use the Dougherty–Fokker–Planck (D-FPO) collision operator as presented in Lenard & Bernstein (1958), Dougherty (1964) approximates the collisions as a combination of drag and diffusion in velocity space. However, unlike the Rosenbluth–Landau Fokker–Planck collision operator, the collision frequency in the D-FPO is independent of velocity. Though this assumption of velocity-independent collision frequency is an approximation, the essential features of a collision operator, i.e. particle, momentum and energy conservation, an H-theorem, and balance between drag and diffusion, are contained in the D-FPO; see Hakim et al. (2020) and Juno (2020) for the theory of the D-FPO in the context of the numerical discretisation of this operator.

The D-FPO operator for self-collisions is

$$C[f] = \nu \nabla_v \cdot \left[(\mathbf{v} - \mathbf{u}) f + \frac{T}{m} \nabla_v f \right], \quad (\text{D.1})$$

where ν is the velocity-independent collision frequency, usually taken to be a constant or the Spitzer collisionality (Braginskii 1965), and as before, we are suppressing species subscripts. To manipulate this collision operator into a form that can be included in the PKPM model, we first transform the velocity coordinates to the local flow frame,

$$C[\bar{f}] = \nu \nabla_{\mathbf{v}'} \cdot \left[(\mathbf{v}' + \mathbf{u} - \mathbf{u}) \bar{f} + \frac{T}{m} \nabla_{\mathbf{v}'} \bar{f} \right] = \nu \nabla_{\mathbf{v}'} \cdot \left(\mathbf{v}' \bar{f} + \frac{T}{m} \nabla_{\mathbf{v}'} \bar{f} \right). \quad (\text{D.2})$$

Furthermore, if we focus exclusively on the gyrotropic piece of the distribution function, $\ell = 0$, the transformation to $(v_{\parallel}, v_{\perp}, \theta)$ coordinates is also reasonably straightforward,

$$C[\bar{f}] = \nu \frac{\partial}{\partial v_{\parallel}} \left(v_{\parallel} \bar{f} + \frac{T}{m} \frac{\partial \bar{f}}{\partial v_{\parallel}} \right) + \nu \frac{\partial}{\partial \xi} \left(2\xi \left[\bar{f} + \frac{T}{T_{\perp}} \frac{\partial \bar{f}}{\partial \xi} \right] \right), \quad (\text{D.3})$$

where we have transformed the perpendicular velocity derivative to $\xi = mv_{\perp}^2/2T_{\perp}$, the coordinates of the Laguerre expansion. This coordinate transformation in the perpendicular velocity is very similar to the transformation to the coordinate μ utilised in gyrokinetic variations of the D-FPO (Francisquez et al. 2020).

With the orthogonality of Laguerre polynomials, the first term evaluates to simply

$$\begin{aligned} C_{v_{\parallel}}[F_{n,0}] &= \int d\xi \exp(-\xi) \nu \frac{\partial}{\partial v_{\parallel}} \left[v_{\parallel} L_n(\xi) \bar{f} + \frac{T}{m} \frac{\partial}{\partial v_{\parallel}} L_n(\xi) \bar{f} \right], \\ &= \nu \frac{\partial}{\partial v_{\parallel}} \left(v_{\parallel} F_{n,0} + \frac{T}{m} \frac{\partial F_{n,0}}{\partial v_{\parallel}} \right). \end{aligned} \quad (\text{D.4})$$

The second term can be integrated by parts to obtain

$$\begin{aligned} &\nu \int d\xi \exp(-\xi) L_n(\xi) \frac{\partial}{\partial \xi} \left(2\xi \left[\bar{f} + \frac{T}{T_{\perp}} \frac{\partial \bar{f}}{\partial \xi} \right] \right), \\ &= -2\nu \int d\xi \exp(-\xi) \xi \frac{\partial L_n(\xi)}{\partial \xi} \left[\bar{f} + \frac{T}{T_{\perp}} \frac{\partial \bar{f}}{\partial \xi} \right], \\ &= -2\nu \int d\xi \exp(-\xi) (nL_n(\xi) - nL_{n-1}(\xi)) \left[\bar{f} + \frac{T}{T_{\perp}} \frac{\partial \bar{f}}{\partial \xi} \right], \\ &= -2n\nu \left[(F_{n,0} - F_{n-1,0}) - \int d\xi \exp(-\xi) \frac{\partial}{\partial \xi} (L_n(\xi) - L_{n-1}(\xi)) \frac{T}{T_{\perp}} \bar{f} \right], \\ &= -2n\nu \left[(F_{n,0} - F_{n-1,0}) + \frac{T}{T_{\perp}} F_{n-1,0} \right], \end{aligned} \quad (\text{D.5})$$

so that the collision operators for the lowest-order PKPM system are

$$C[F_0] = \nu \frac{\partial}{\partial v_{\parallel}} \left(v_{\parallel} F_0 + \frac{T}{m} \frac{\partial F_0}{\partial v_{\parallel}} \right), \quad (\text{D.6})$$

$$C[\mathcal{G}] = 2\nu \left(\frac{T}{m} F_0 - \mathcal{G} \right) + \nu \frac{\partial}{\partial v_{\parallel}} \left(v_{\parallel} \mathcal{G} + \frac{T}{m} \frac{\partial \mathcal{G}}{\partial v_{\parallel}} \right). \quad (\text{D.7})$$

We can take the $1/2 m v_{\parallel}^2$ moment of (D.6) and the mass-weighted zeroth moment of (D.7) to determine how the collision operators affect the evolution of p_{\parallel} and p_{\perp} ,

$$\frac{1}{2} \frac{\partial p_{\parallel}}{\partial t} = \nu \left(\rho \frac{T}{m} - p_{\parallel} \right), \quad (\text{D.8})$$

$$\frac{\partial p_{\perp}}{\partial t} = 2\nu \left(\rho \frac{T}{m} - p_{\perp} \right), \quad (\text{D.9})$$

which when summed to obtain the total internal energy equation is

$$\frac{\partial}{\partial t} \left(\frac{3}{2} p \right) = \nu \left(3\rho \frac{T}{m} - p_{\parallel} - 2p_{\perp} \right) = \nu (3p - 3p) = 0, \quad (\text{D.10})$$

as expected.

Note that this expression does not imply PKPM lacks viscosity and viscous heating. In the high collisionality limit, the D-FPO in these velocity coordinates will modify the pressure tensor, which then couples to the momentum equation. This equation merely implies that there is no additional heating due to the collision operator in these velocity coordinates, only scattering between p_{\parallel} and p_{\perp} .

We can also include cross-species collision of the form

$$C[f]_{rs} = \nu_{rs} \nabla_{\mathbf{v}} \cdot [(\mathbf{v} - \mathbf{u}_{rs}) f + v_{t,rs}^2 \nabla_{\mathbf{v}} f], \quad (\text{D.11})$$

where the subscript rs denotes the collisions of species s , the species we are evolving, with species r . Here, the intermediate flow \mathbf{u}_{rs} and intermediate thermal velocity squared $v_{t,rs}^2$ are determined from the constraints that energy and momentum are conserved, along with the relaxation rates such as the Morse relaxation rates (Morse 1963). For the purposes of inclusion in the PKPM model, these two parameters can be any of the forms derived in previous works (Greene 1973; Francisquez et al. 2022) and need not be specified at this stage.

Two important changes arise due to the inclusion of cross-species collisions. The first is that cross-species collisions include the effects of momentum exchange between the two species, i.e. the first velocity moment of the cross-species collision operator is

$$\begin{aligned} \int m_s \mathbf{v} C[f]_{rs} d^3 \mathbf{v} &= \int m_s \mathbf{v} \nu_{rs} \nabla_{\mathbf{v}} \cdot [(\mathbf{v} - \mathbf{u}_{rs}) f + v_{t,rs}^2 \nabla_{\mathbf{v}} f] d^3 \mathbf{v}, \\ &= \nu_{rs} (\rho_s \mathbf{u}_{rs} - \rho_s \mathbf{u}). \end{aligned} \quad (\text{D.12})$$

Thus, in the boost to the local flow frame, the previous substitution of the pressure forces must be modified to

$$\frac{q}{m} (\mathbf{E} + \mathbf{u} \times \mathbf{B}) - \frac{\partial \mathbf{u}}{\partial t} - \mathbf{u} \cdot \nabla \mathbf{u} = \frac{1}{\rho} \nabla \cdot \mathbf{P} - \nu_{rs} (\mathbf{u}_{rs} - \mathbf{u}). \quad (\text{D.13})$$

In addition, this collision operator's velocity coordinates also need to be transformed to the local flow frame,

$$C[f]_{rs} = \nu_{rs} \nabla_{\mathbf{v}'} \cdot [(\mathbf{v}' + \mathbf{u} - \mathbf{u}_{rs}) \bar{f} + v_{t,rs}^2 \nabla_{\mathbf{v}'} \bar{f}]. \quad (\text{D.14})$$

Thus, there is a cancellation of the forces arising due to the momentum exchange such that

$$\begin{aligned}\nabla_{\mathbf{v}'} \cdot \left[\left(\frac{1}{\rho_s} \nabla \cdot \mathbf{P} - v_{rs} \{ \mathbf{u}_{rs} - \mathbf{u} \} \right) \bar{f} \right] &= v_{rs} \nabla_{\mathbf{v}'} \cdot \left[(\mathbf{v}' + \mathbf{u} - \mathbf{u}_{rs}) \bar{f} + v_{t,rs}^2 \nabla_{\mathbf{v}'} \bar{f} \right], \\ \nabla_{\mathbf{v}'} \cdot \left[\left(\frac{1}{\rho_s} \nabla \cdot \mathbf{P} \right) f \right] &= v_{rs} \nabla_{\mathbf{v}'} \cdot (\mathbf{v}' f + v_{t,rs}^2 \nabla_{\mathbf{v}'} f). \end{aligned} \quad (\text{D.15})$$

The inclusion of cross-species collisions using the D-FPO only requires the sum over collision frequencies and intermediate thermal velocities. The same substitution of the divergence of the pressure tensor cancels the momentum exchange, and therefore, as we expect, the momentum exchange from cross-species collisions is contained solely in the momentum evolution.

REFERENCES

- ABEL, I. G., PLUNK, G. G., WANG, E., BARNES, M., COWLEY, S. C., DORLAND, W. & SCHEKOCHIHIN, A. A. 2013 Multiscale gyrokinetics for rotating tokamak plasmas: fluctuations, transport and energy flows. *Rep. Prog. Phys.* **76**, 116201.
- ALLMANN-RAHN, F., LAUTENBACH, S., DEISENHOFER, M. & GRAUER, R. 2024 The muphyii code: multiphysics plasma simulation on large hpc systems. *Comp. Phys. Comm.* **296**, 109064.
- ALLMANN-RAHN, F., LAUTENBACH, S., GRAUER, R. & SYDORA, R. D. 2021 Fluid simulations of three-dimensional reconnection that capture the lower-hybrid drift instability. *J. Plasma Phys.* **87**, 905870115.
- ALLMANN-RAHN, F., TROST, T. & GRAUER, R. 2018 Temperature gradient driven heat flux closure in fluid simulations of collisionless reconnection. *J. Plasma Phys.* **84**, 905840307.
- ANAGNOSTOPOULOS, G. C. & KALIABETSOS, G. D. 1994 Shock drift acceleration of energetic (E greater than or equal to 50 keV) protons and (E greater than or equal to 37 keV/n) alpha particles at the Earth's bow shock as a source of the magnetosheath energetic ion events. *J. Geophys. Res.* **99**, 2335–2349.
- ANAGNOSTOPOULOS, G. C., RIGAS, A. G., SARRIS, E. T. & KRIMIGIS, S. M. 1998 Characteristics of upstream energetic (E ≥ 50 keV) ion events during intense geomagnetic activity. *J. Geophys. Res.* **103**, 9521–9534.
- ANAGNOSTOPOULOS, G. C., TENENTES, V. & VASSILIADIS, E. S. 2009 MeV ion event observed at 0950 UT on 4 May 1998 at a quasi-perpendicular bow shock region: new observations and an alternative interpretation on its origin. *J. Geophys. Res.* **114**, A09101.
- ANTONSEN, T.M.Jr. & LANE, B. 1980 Kinetic equations for low frequency instabilities in inhomogeneous plasmas. *Phys. Fluids* **23**, 1205–1214.
- ARNOLD, H., DRAKE, J. F., SWISDAK, M. & DAHLIN, J. 2019 Large-scale parallel electric fields and return currents in a global simulation model. *Phys. Plasmas* **26**, 102903.
- ARNOLD, H., DRAKE, J. F., SWISDAK, M., GUO, F., DAHLIN, J. T., CHEN, B., FLEISHMAN, G., GLESENER, L., KONTAR, E., PHAN, T. & SHEN, C. 2021 Electron acceleration during macroscale magnetic reconnection. *Phys. Rev. Lett.* **126**, 135101.
- ARNOLD, H., DRAKE, J. F., SWISDAK, M., GUO, F., DAHLIN, J. T. & ZHANG, Q. 2022 Slow shock formation upstream of reconnecting current sheets. *Astrophys. J.* **926**, 24.
- The Event Horizon Telescope Collaboration *et al.* 2019a First m87 event horizon telescope results. i. the shadow of the supermassive black hole. *Astrophys. J. Lett.* **875**, L1.
- The Event Horizon Telescope Collaboration 2019b First M87 Event Horizon Telescope Results. VI. The Shadow and Mass of the Central Black Hole. *Astrophys. J. Lett.* **875**, L6.
- Astrophys. J. Lett. The event horizon telescope, collaboration *et al.*, 2021 first M87 event horizon telescope results. VIII. Magnetic field structure near the event horizon, **910**, 43.

- BACCHINI, F., RIPPERDA, B., PHILIPPOV, A.A. & PARFREY, K. 2020 A coupled guiding center–boris particle pusher for magnetized plasmas in compact-object magnetospheres. *Astrophys. J. Supp.* **251**, 10.
- BALE, S. D., KASPER, J. C., HOWES, G. G., QUATAERT, E., SALEM, C. & SUNDKVIST, D. 2009 Magnetic fluctuation power near proton temperature anisotropy instability thresholds in the solar wind. *Phys. Rev. Lett.* **103**, 211101.
- BALL, L. & MELROSE, D. B. 2001 Shock drift acceleration of electrons. *Publ. Astron. Soc. Aust.* **18**, 361–373.
- BERLOK, T., PAKMOR, R. & PFROMMER, C. 2019 Braginskii viscosity on an unstructured, moving mesh accelerated with super-time-stepping. *Mon. Not. Roy. Astron. Soc.* **491**, 2919–2938.
- BIRN, J., DRAKE, J. F., SHAY, M. A., ROGERS, B. N., DENTON, R. E., HESSE, M., KUZNETSOVA, M., MA, Z. W., BHATTACHARJEE, A., OTTO, A. & PRITCHETT, P. L. 2001 Geospace environmental modeling (gem) magnetic reconnection challenge. *J. Geophys. Res.* **106**, 3715–3719.
- BLANDFORD, R. & EICHLER, D. 1987 Particle acceleration at astrophysical shocks: a theory of cosmic ray origin. *Phys. Rep.* **154**, 1–75.
- BLANDFORD, R. D. & OSTRICKER, J. P. 1978 Particle acceleration by astrophysical shocks. *Astrophys. J.* **221**, L29–L32.
- BOROVSKY, J. E. & VALDIVIA, J. A. 2018 The earth’s magnetosphere: a systems science overview and assessment. *Surv. Geophys.* **39**, 817–859.
- BOTT, A. F. A., ARZAMASSKIY, L., KUNZ, M. W., QUATAERT, E. & SQUIRE, J. 2021 Adaptive critical balance and firehose instability in an expanding, turbulent, collisionless plasma. *Astrophys. J.* **922**, L35.
- BOTT, A. F. A., KUNZ, M. W., QUATAERT, E., SQUIRE, J. & ARZAMASSKIY, L. 2025 Thermodynamics and collisionality in firehose-susceptible high- β plasmas.
- BRAGINSKII, S. I. 1965 *Reviews of Plasma Physics*. Vol. 1. Consultants Bureau.
- BRESLAU, J., FERRARO, N. & JARDIN, S. 2009 Some properties of the M3D-C1 form of the three-dimensional magnetohydrodynamics equations. *Phys. Plasmas* **16**, 092503.
- BRIZARD, A. J. & HAHM, T. S. 2007 Foundations of nonlinear gyrokinetic theory. *Rev. Mod. Phys.* **79**, 421–468.
- CAGAS, P., JUNO, J., HAKIM, A., LAJOIE, A., CHU, F., LANGENDORF, S. & SRINIVASAN, B. 2023 An investigation of shock formation vs shock mitigation of colliding plasma jets. *Phys. Plasmas* **30**, 053903.
- CARY, J. & BRIZARD, A. 2009 Hamiltonian theory of guiding-center motion. *Rev. Mod. Phys.* **81**, 693–738.
- CASSAK, P. A., BAYLOR, R. N., FERMO, R. L., BEIDLER, M. T., SHAY, M. A., SWISDAK, M., DRAKE, J. F. & KARIMABADI, H. 2015 Fast magnetic reconnection due to anisotropic electron pressure. *Phys. Plasmas* **22**, 020705.
- CASSAK, P. A., LIU, Y.-H. & SHAY, M. A. 2017 A review of the 0.1 reconnection rate problem. *J. Plasma Phys.* **83**, 715830501.
- CATTO, P. J., TANG, W. M. & BALDWIN, D. E. 1981 Generalized gyrokinetics. *Plasma Phys.* **23**, 639.
- CHEN, C. H. K., MATTEINI, L., SCHEKOCHIHIN, A. A., STEVENS, M. L., SALEM, C. S., MARUCA, B. A., KUNZ, M. W. & BALE, S. D. 2016 Multi-species measurements of the firehose and mirror instability thresholds in the solar wind. *Astrophys. J. Lett.* **825**, L26.
- CHEW, G. F., GOLDBERGER, M. L. & LOW, F. E. 1956 The Boltzmann equation and the one-fluid hydromagnetic equations in the absence of particle collisions. *Proc. Roy. Soc.* **236**, 112–118.
- COCKBURN, B. & SHU, C.-W. 1998 The Runge–Kutta discontinuous Galerkin method for conservation laws V: multidimensional systems. *J. Comp. Phys.* **141**, 199–224.
- COCKBURN, B. & SHU, C.-W. 2001 Runge–Kutta discontinuous Galerkin methods for convection-dominated problems. *J. Sci. Comput.* **16**, 173–261.
- CONLEY, S. A., JUNO, J., TENBARGE, J. M., BARBHUIYA, M. H., CASSAK, P. A., HOWES, G. G. & LICHKO, E. 2024 The kinetic analog of the pressure–strain interaction. *Phys. Plasmas* **31**, 122117.
- COX, D. P. 2005 The three-phase interstellar medium revisited. *Ann. Rev. Astron. Astrophys.* **43**, 337–385.
- DECKER, R. B. 1988 The role of drifts in diffusive shock acceleration. *Astrophys. J.* **324**, 566–573.
- DELZANNO, G. L. 2015 Multi-dimensional, fully-implicit, spectral method for the vlasov–maxwell equations with exact conservation laws in discrete form. *J. Comp. Phys.* **301**, 338–356.

- DONG, C., WANG, L., HAKIM, A., BHATTACHARJEE, A., SLAVIN, J.A., DiBRACCIO, G.A. & GERMASCHESKI, K. 2019 Global ten-moment multifluid simulations of the solar wind interaction with mercury: from the planetary conducting core to the dynamic magnetosphere. *Geophys. Res. Lett.* **46**, 11584–11596.
- DORLAND, W. & HAMMETT, G. W. 1993 Gyrofluid turbulence models with kinetic effects. *Phys. Fluids B* **5**, 812–835.
- DOUGHERTY, J. P. 1964 Model Fokker–Planck equation for a plasma and its solution. *Phys. Fluids* **7**, 1788–1799.
- DRAKE, J. F., ARNOLD, H., SWISDAK, M. & DAHLIN, J. T. 2019 A computational model for exploring particle acceleration during reconnection in macroscale systems. *Phys. Plasmas* **26**, 012901.
- EGEDAL, J. 2002 A drift kinetic approach to stationary collisionless magnetic reconnection in an open cusp plasma. *Phys. Plasmas* **9**, 1095–1103.
- EGEDAL, J., LE, A. & DAUGHTON, W. 2013 A review of pressure anisotropy caused by electron trapping in collisionless plasma, and its implications for magnetic reconnection. *Phys. Plasmas* **20**, 061201.
- ELLISON, D. C. 1983 Diffusive first-order Fermi acceleration at quasi-parallel interplanetary shocks - Injection of thermal ions. *Proc. 18th Intl. Cosmic Ray Conf.* **10**, 108–111.
- FABIAN, A. C. 1994 Cooling flows in clusters of galaxies. *Ann. Rev. Astron. Astrophys.* **32**, 277–318.
- FERMI, E. 1949 On the origin of the cosmic radiation. *Phys. Rev* **75**, 1169–1174.
- FERMI, E. 1954 Galactic magnetic fields and the origin of cosmic radiation. *Astrophys. J.* **119**, 1.
- FERMO, R. L., DRAKE, J. F. & SWISDAK, M. 2012 Secondary magnetic islands generated by the Kelvin–Helmholtz instability in a reconnecting current sheet. *Phys. Rev. Lett.* **108**, 255005.
- FERRARO, N. M. & JARDIN, S. C. 2006 Finite element implementation of Braginskii’s gyroviscous stress with application to the gravitational instability. *Phys. Plasmas* **13**, 092101.
- FORSLUND, D. W. & SHONK, C. R. 1970 Formation and structure of electrostatic collisionless shocks. *Phys. Rev. Lett.* **25**, 1699–1702.
- FRANCISQUEZ, M., BERNARD, T. N., MANDELL, N. R., HAMMETT, G. W. & HAKIM, A. 2020 Conservative discontinuous galerkin scheme of a gyro-averaged dougherty collision operator. *Nucl. Fusion* **60**, 096021.
- FRANCISQUEZ, M., JUNO, J., HAKIM, A., HAMMETT, G.W. & ERNST, D.R. 2022 Improved multispecies dougherty collisions. *J. Plasma Phys.* **88**, 905880303.
- FREI, B. J., HOFFMANN, A. C. D., RICCI, P., BRUNNER, S. & TECCHIOLL, Z. 2023a Moment-based approach to the flux-tube linear gyrokinetic model. *J. Plasma Phys.* **89**, 905890414.
- FREI, B. J., JORGE, R. & RICCI, P. 2020 A gyrokinetic model for the plasma periphery of tokamak devices. *J. Plasma Phys.* **86**, 905860205.
- FREI, B. J., MENCKE, J. & RICCI, P. 2023b Full-f turbulent simulation in a linear device using a gyro-moment approach
- FREI, B. J., ULBL, P., TRILAKSONO, J. & JENKO, F. 2024 Spectrally accelerated edge and scrape-off layer gyrokinetic turbulence simulations.
- FRIEMAN, E. A. & CHEN, L. 1982 Nonlinear gyrokinetic equations for low-frequency electromagnetic waves in general plasma equilibria. *Phys. Fluids* **25**, 502–508.
- FRIEMAN, E., DAVIDSON, R. & LANGDON, B. 1966 Higher-order corrections to the chew-goldberger-low theory. *Phys. Fluids* **9**, 1475–1482.
- FURTH, H. P. 1975 Tokamak research. *Nucl. Fusion* **15**, 487.
- GARY, S.P., SKOUG, R.M., STEINBERG, J.T. & SMITH, C.W. 2001 Proton temperature anisotropy constraint in the solar wind: ace observations. *Geophys. Res. Lett.* **28**, 2759–2762.
- GRAD, H. 1949 On the kinetic theory of rarefied gases. *Commun. Pure Appl. Math.* **2**, 331–407.
- GREENE, J.M. 1973 Improved Bhatnaga–Gross–Krook model of electron-ion collisions. *Phys. Fluids* **16**, 2022–2023.
- GÜNTER, S., LACKNER, K. & TICHMANN, C. 2007 Finite element and higher order difference formulations for modelling heat transport in magnetised plasmas. *J. Comput. Phys.* **226**, 2306–2316.
- GÜNTER, S., YU, Q., KRÜGER, J. & LACKNER, K. 2005 Modelling of heat transport in magnetised plasmas using non-aligned coordinates. *J. Comput. Phys.* **209**, 354–370.

- HAGGERTY, C.C., SHAY, M.A., CHASAPIS, A., PHAN, T.D., DRAKE, J.F., MALAKIT, K., CASSAK, P.A. & KIEOKAEW, R. 2018 The reduction of magnetic reconnection outflow jets to sub-alfvénic speeds. *Phys. Plasmas* **25**, 102120.
- HAKIM, A. 2008 Extended MHD modelling with the ten-moment equations. *J. Fusion Energy* **27**, 36–43.
- HAKIM, A., LOVERICH, J. & SHUMLAK, U. 2006 A high resolution wave propagation scheme for ideal two-fluid plasma equations. *J. Comput. Phys.* **219**, 418–442.
- HAKIM, A., FRANCISQUEZ, M., JUNO, J. & HAMMETT, G.W. 2020 Conservative discontinuous Galerkin schemes for nonlinear Dougherty–Fokker–Planck collision operators. *J. Plasma Phys.* **86**, 905860403.
- HAKIM, A. & JUNO, J. 2020 Alias-free, matrix-free, and quadrature-free discontinuous galerkin algorithms for (plasma) kinetic equations. In *Proceedings of the International Conference for High Performance Computing, Networking, Storage and Analysis*. IEEE Press.
- HAMMETT, G. W., DORLAND, W. & PERKINS, F.W. 1992 Fluid models of phase mixing, landau damping, and nonlinear gyrokinetic dynamics. *Phys. Fluids B* **4**, 2052.
- HAMMETT, G.W. & PERKINS, F.W. 1990 Fluid moment models for landau damping with application to the ion-temperature-gradient instability. *Phys. Rev. Lett.* **64**, 3019.
- HELLINGER, P., TRÁVNÍČEK, P., KASPER, J. C. & LAZARUS, A. J. 2006 Solar wind proton temperature anisotropy: linear theory and WIND/SWE observations. *Geophys. Res. Lett.* **33**, 9101.
- HÉNON, M. 1982 Vlasov equation. *ASAP* **114**, 211.
- HESSE, M., LIU, Y.-H., CHEN, L.-J., BESSHO, N., WANG, S., BURCH, J. L., MORETTO, T., NORGREN, C., GENESTRETI, K. J., PHAN, T. D. & TENFJORD, P. 2018 The physical foundation of the reconnection electric field. *Phys. Plasmas* **25**, 032901.
- HESTHAVEN, J. S. & WARBURTON, T. 2007 *Nodal Discontinuous Galerkin Methods: Algorithms, Analysis, and Applications*. Springer Science & Business Media.
- HINTON, F. L. & WONG, S. K. 1985 Neoclassical ion transport in rotating axisymmetric plasmas. *Phys. Fluids* **28**, 3082–3098.
- HOFFMANN, A. C. D., BALESTRI, A. & RICCI, P. 2024 Investigation of triangularity effects on tokamak edge turbulence through multi-fidelity gyrokinetic simulations. *Plasma Phys. Contol. Fusion* **67**, 015031.
- HOFFMANN, A. C. D., FREI, B. J. & RICCI, P. 2023a Gyrokinetic moment-based simulations of the dimits shift. *J. Plasma Phys.* **89**, 905890611.
- HOFFMANN, A. C. D., FREI, B. J. & RICCI, P. 2023b Gyrokinetic simulations of plasma turbulence in a z-pinch using a moment-based approach and advanced collision operators. *J. Plasma Phys.* **89**, 905890214.
- HOLLOWAY, J.P. 1996 Spectral velocity discretizations for the Vlasov–Maxwell equations. *Trans. Theory Stat. Phys.* **25**, 1–32.
- HOPKINS, P.F. 2016 Anisotropic diffusion in mesh-free numerical magnetohydrodynamics. *Mon. Not. Roy. Astron. Soc.* **466**, 3387–3405.
- HOWES, G.G., COWLEY, S.C., DORLAND, W., HAMMETT, G.W., QUATAERT, E. & SCHEKOCHIHIN, A.A. 2006 Astrophysical gyrokinetics: basic equations and linear theory. *Astrophys. J.* **651**, 590.
- HUMPHREY, P.J., BUOTE, D.A., CANIZARES, C.R., FABIAN, A.C. & MILLER, J.M. 2011 A census of baryons and dark matter in an isolated, milky way sized elliptical galaxy. *Astrophys. J.* **729**, 53.
- IMBERT-GERARD, L.-M., PAUL, E.J. & WRIGHT, A.M. 2020 An introduction to stellarators: from magnetic fields to symmetries and optimization.
- ISSAN, O., KOSHKAROV, O., HALPERN, F.D., KRAMER, B. & DELZANNO, G.L. 2024 Anti-symmetric and positivity preserving formulation of a spectral method for Vlasov–Poisson equations. *J. Comput. Phys.* **514**, 113263.
- JUNO, J. 2020 A deep dive into the distribution function: understanding phase space dynamics with continuum Vlasov–Maxwell simulations *PhD thesis*. University of Maryland.
- JUNO, J., HAKIM, A., TENBARGE, J., SHI, E. & DORLAND, W. 2018 Discontinuous Galerkin algorithms for fully kinetic plasmas. *J. Comput. Phys.* **353**, 110–147.
- KASPER, J. C., LAZARUS, A. J. & GARY, S. P. 2002 Wind/SWE observations of firehose constraint on solar wind proton temperature anisotropy. *Geophys. Res. Lett.* **29**, 20–21.

- KEMPSKI, P., QUATAERT, E., SQUIRE, J. & KUNZ, M.W. 2019 Shearing-box simulations of MRI-driven turbulence in weakly collisional accretion discs. *Mon. Not. Roy. Astron. Soc.* **486**, 4013–4029.
- KOMAROV, S., SCHEKOCHIHIN, A. A., CHURAZOV, E. & SPITKOVSKY, A. 2018 Self-inhibiting thermal conduction in a high- β , whistler-unstable plasma. *J. Plasma Phys.* **84**, 905840305.
- KOMAROV, S. V., CHURAZOV, E. M., KUNZ, M. W. & SCHEKOCHIHIN, A. A. 2016 Thermal conduction in a mirror-unstable plasma. *Mon. Not. Roy. Astron. Soc.* **460**, 467–477.
- KOSHKAROV, O., MANZINI, G., DELZANNO, G. L., PAGLIANTINI, C. & ROYTERSHTEYN, V. 2021 The multi-dimensional hermite-discontinuous galerkin method for the Vlasov–Maxwell equations. *Comput. Phys. Commun.* **264**, 107866.
- KROMMES, J.A. 2012 The gyrokinetic description of microturbulence in magnetized plasmas. *Annu. Rev. Fluid Mech.* **44**, 175–201.
- KULDINOW, D.A., YAMASHITA, Y. & HARA, K. 2024a Ten-moment fluid model for low-temperature magnetized plasmas. *Phys. Plasmas* **31**, 123506.
- KULDINOW, D.A., YAMASHITA, Y., MANSOUR, A.R. & HARA, K. 2024b Ten-moment fluid model with heat flux closure for gasdynamic flows. *J. Comput. Phys.* **508**, 113030.
- KULSRUD, R.M. 1964 *Teoria Dei Plasmii*. Academic.
- KULSRUD, R.M. 1983 Mhd description of plasma. *Handb. Plasma Phys.* **1**, 115.
- KUNZ, M.W., JONES, T.W. & ZHURAVLEVA, I. 2022 *Plasma Physics of the Intracluster Medium*, pp. 1–42. Springer Nature.
- KUNZ, M.W., SCHEKOCHIHIN, A.A. & STONE, J.M. 2014 Firehose and mirror instabilities in a collisionless shearing plasma. *Phys. Rev. Lett.* **112**, 205003.
- KUNZ, M.W., STONE, J.M. & QUATAERT, E. 2016 Magnetorotational turbulence and dynamo in a collisionless plasma. *Phys. Rev. Lett.* **117**, 235101.
- LE, A., EGEDAL, J., DAUGHTON, W., FOX, W. & KATZ, N. 2009 Equations of state for collisionless guide-field reconnection. *Phys. Rev. Lett.* **102**, 085001.
- LE, A., EGEDAL, J., OHIA, O., DAUGHTON, W., KARIMABADI, H. & LUKIN, V. S. 2013 Regimes of the electron diffusion region in magnetic reconnection. *Phys. Rev. Lett.* **110**, 135004.
- LENARD, A. & BERNSTEIN, I.B. 1958 Plasma oscillations with diffusion in velocity space. *Phys. Rev.* **112**, 1456–1459.
- LI, X. & HABBAL, S.R. 2000 Electron kinetic firehose instability. *J. Geophys. Res.* **105**, 27377–27385.
- LIU, Y.-H., CASSAK, P., LI, X., HESSE, M., LIN, S.-C. & GENESTRETI, K. 2022 First-principles theory of the rate of magnetic reconnection in magnetospheric and solar plasmas. *Commun. Phys.* **5**, 97.
- LIU, Y.-H., HESSE, M., GUO, F., DAUGHTON, W., LI, H., CASSAK, P. A. & SHAY, M. A. 2017 Why does steady-state magnetic reconnection have a maximum local rate of order 0.1? *Phys. Rev. Lett.* **118**, 085101.
- LIU, Y.-H., HESSE, M., GENESTRETI, K., NAKAMURA, R., BURCH, J.L., CASSAK, P.A., BESSHO, N., EASTWOOD, J.P., PHAN, T., SWISDAK, M., TOLEDO-REDONDO, S., HOSHINO, M., NORGREN, C., JI, H. & NAKAMURA, T.K.M. 2025 Ohm's law, the reconnection rate, and energy conversion in collisionless magnetic reconnection. *Space Sci. Rev.* **221**, 16.
- LOUREIRO, N. F., DORLAND, W., FAZENDEIRO, L., KANEKAR, A., MALLET, A., VILELAS, M. S. & ZOCCO, A. 2016 Viriato: a fourier–hermite spectral code for strongly magnetized fluid–kinetic plasma dynamics. *Comput. Phys. Comm.* **206**, 45–63.
- LOUREIRO, N. F., SCHEKOCHIHIN, A. A. & ZOCCO, A. 2013 Fast collisionless reconnection and electron heating in strongly magnetized plasmas. *Phys. Rev. Lett.* **111**, 025002.
- MALKOV, M. A. & DRURY, L. O. 2001 Nonlinear theory of diffusive acceleration of particles by shock waves. *Rep. Prog. Phys.* **64**, 429–481.
- MALLET, A., ERIKSSON, S., SWISDAK, M. & JUNO, J. 2025a The effect of shear flow on the resistive tearing instability.
- MALLET, A., ERIKSSON, S., SWISDAK, M. & JUNO, J. 2025b Suppression of the collisionless tearing mode by flow shear: implications for reconnection onset in the alfvénic solar wind. *J. Plasma Phys.* **91**.
- MANDELL, N. R., DORLAND, W., ABEL, I., GAUR, R., KIM, P., MARTIN, M. & QIAN, T. 2024 Gx: a GPU-native gyrokinetic turbulence code for tokamak and stellarator design. *J. Plasma Phys.* **90**, 905900402.

- MANDELL, N. R., DORLAND, W. & LANDREMAN, M. 2018 Laguerre–hermite pseudo-spectral velocity formulation of gyrokinetics. *J. Plasma Phys.* **84**, 905840108.
- MANDELL, N. R., HAKIM, A., HAMMETT, G. W. & FRANCISQUEZ, M. 2020 Electromagnetic full-f gyrokinetics in the tokamak edge with discontinuous Galerkin methods. *J. Plasma Phys.* **86**.
- MARSCH, E., MÜHLHÄUSER, K.-H., SCHWENN, R., ROSENBAUER, H., PILIPP, W. & NEUBAUER, F. M. 1982 Solar wind protons: three-dimensional velocity distributions and derived plasma parameters measured between 0.3 and 1 au. *J. Geophys. Res.* **87**, 52–72.
- MARSCH, E. 2006 Kinetic physics of the solar corona and solar wind. *Living Rev. Sol. Phys.* **3**, 1.
- MEIER, E. T., LUKIN, V. S. & SHUMLAK, U. 2010 Spectral element spatial discretization error in solving highly anisotropic heat conduction equation. *Comput. Phys. Commun.* **181**, 837–841.
- MELVILLE, S., SCHEKOCHIHIN, A. A. & KUNZ, M. W. 2016 Pressure-anisotropy-driven microturbulence and magnetic-field evolution in shearing, collisionless plasma. *Mon. Not. Roy. Astron. Soc.* **459**, 2701–2720.
- MILLER, S. T. & SHUMLAK, U. 2016 A multi-species 13-moment model for moderately collisional plasmas. *Phys. Plasmas* **23**, 082303.
- MORSE, T. F. 1963 Energy and momentum exchange between nonequipartition gases. *Phys. Fluids* **6**, 1420–1427.
- MUÑOZ, P. A., TOLD, D., KILIAN, P., BÜCHNER, J. & JENKO, F. 2015 Gyrokinetic and kinetic particle-in-cell simulations of guide-field reconnection. i. macroscopic effects of the electron flows. *Phys. Plasmas* **22**, 082110.
- NG, J., HAKIM, A., JUNO, J. & BHATTACHARJEE, A. 2019 Drift instabilities in thin current sheets using a two-fluid model with pressure tensor effects. *J. Geophys. Res.* **124**, 3331–3346.
- NG, J., HUANG, Y.-M., HAKIM, A., BHATTACHARJEE, A., STANIER, A., DAUGHTON, W., WANG, L. & GERMASCHESKI, K. 2015 The island coalescence problem: scaling of reconnection in extended fluid models including higher-order moments. *Phys. Plasmas* **22**, 112104.
- NG, J., HAKIM, A., WANG, L. & BHATTACHARJEE, A. 2020 An improved ten-moment closure for reconnection and instabilities. *Phys. Plasmas* **27**, 082106.
- NG, J., HAKIM, A. & BHATTACHARJEE, A. 2018 Using the maximum entropy distribution to describe electrons in reconnecting current sheets. *Phys. Plasmas* **25**, 082113.
- NICASTRO, F., MATHUR, S., ELVIS, M., DRAKE, J., FANG, T., FRUSCIONE, A., KRONGOLD, Y., MARSHALL, H., WILLIAMS, R. & ZEAS, A. 2005 The mass of the missing baryons in the x-ray forest of the warm–hot intergalactic medium. *Nature* **433**, 495–498.
- NORTHROP, T. G. 1961 The guiding center approximation to charged particle motion. *Ann. Phys.* **15**, 79–101.
- NORTHROP, T. G. 1963 Adiabatic charged-particle motion. *Rev. Geophys.* **1**, 283–304.
- OHIA, O., EGEDAL, J., LUKIN, V. S., DAUGHTON, W. & LE, A. 2012 Demonstration of anisotropic fluid closure capturing the kinetic structure of magnetic reconnection. *Phys. Rev. Lett.* **109**, 115004.
- OHIA, O., EGEDAL, J., LUKIN, V. S., DAUGHTON, W. & LE, A. 2015 Scaling laws for magnetic reconnection, set by regulation of the electron pressure anisotropy to the firehose threshold. *Geophys. Res. Lett.* **42**, 10,549–10,556.
- PAGLIANTINI, C., MANZINI, G., KOSHKAROV, O., DELZANNO, G. L. & ROYTERSHEYN, V. 2023 Energy-conserving explicit and implicit time integration methods for the multi-dimensional hermite-dg discretization of the vlasov-maxwell equations. *Comput. Phys. Commun.* **284**, 108604.
- PARKER, J. T., HIGHCOCK, E. G., SCHEKOCHIHIN, A. A. & DELLAR, P. J. 2016 Suppression of phase mixing in drift-kinetic plasma turbulence. *Phys. Plasmas* **23**, 070703.
- PARKER, J. T. & DELLAR, P. J. 2015 Fourier–hermite spectral representation for the vlasov–poisson system in the weakly collisional limit. *J. Plasma Phys.* **81**, 305810203.
- PASCHMANN, G., SCKOPKE, N., BAME, S. J. & GOSLING, J. T. 1982 Observations of gyrating ions in the foot of the nearly perpendicular bow shock. *Geophys. Res. Lett.* **9**, 881–884.
- PETERSON, J. R. & FABIAN, A. C. 2006 X-ray spectroscopy of cooling clusters. *Phys. Rep.* **427**, 1–39.
- PEZZI, O., COZZANI, G., CALIFANO, F., VALENTINI, F., GUARRASI, M., CAMPOREALE, E., BRUNETTI, G., RETINÒ, A. & VELTRI, P. 2019 Vida: a vlasov–darwin solver for plasma physics at electron scales. *J. Plasma Phys.* **85**, 905850506.

- PHILIPPOV, A. & KRAMER, M. 2022 Pulsar magnetospheres and their radiation. *Annu. Rev. Astron. Astr.* **60**, 495–558.
- QUATAERT, E. 2001 Low radiative-efficiency accretion flows. In *Probing the Physics of Active Galactic Nuclei* (ed. B.M. PETERSON, R.W. POGGE & R.S. POLIDAN), vol. **224**, p. 71. Astronomical Society of the Pacific Conference Series.
- RAMOS, J. J. 2003 Dynamic evolution of the heat fluxes in a collisionless magnetized plasma. *Phys. Plasmas* **10**, 3601–3607.
- RAMOS, J. J. 2005 Fluid formalism for collisionless magnetized plasmas. *Phys. Plasmas* **12**, 052102.
- RAMOS, J. J. 2008 Finite-Larmor-radius kinetic theory of a magnetized plasma in the macroscopic flow reference frame. *Phys. Plasmas* **15**, 082106.
- RAMOS, J. J. 2016 On stability criteria for kinetic magnetohydrodynamics. *J. Plasma Phys.* **82**, 905820607.
- REED, W. H. & HILL, T. R. 1973 *Triangular Mesh Methods for the Neutron Transport Equation*. Los Alamos National Laboratory
- RICHARDSON, J. D., BURLAGA, L. F., ELLIOTT, H., KURTH, W. S., LIU, Y. D. & VON STEIGER, R. 2022 Observations of the outer heliosphere, heliosheath, and interstellar medium. *Space Sci. Rev.* **218**, 35.
- RIPPERDA, B., BACCHINI, F., TEUNISSEN, J., XIA, C., PORTH, O., SIRONI, L., LAPENTA, G. & KEPPENS, R. 2018 A comprehensive comparison of relativistic particle integrators. *Astrophys. J. Supp.* **235**, 21.
- RIQUELME, M.A., QUATAERT, E. & VERSCHAREN, D. 2016 Pic simulations of the effect of velocity space instabilities on electron viscosity and thermal conduction. *Astrophys. J.* **824**, 123.
- ROBERG-CLARK, G. T., DRAKE, J. F., REYNOLDS, C. S. & SWISDAK, M. 2016 Suppression of electron thermal conduction in the high β intracluster medium of galaxy clusters. *Astrophys. J. Lett.* **830**.
- ROBERG-CLARK, G. T., DRAKE, J. F., REYNOLDS, C. S. & SWISDAK, M. 2018 Suppression of electron thermal conduction by whistler turbulence in a sustained thermal gradient. *Phys. Rev. Lett.* **120**, 035101.
- ROSIN, M. S., SCHEKOCHIHIN, A. A., RINCON, F. & COWLEY, S. C. 2011 A non-linear theory of the parallel firehose and gyrothermal instabilities in a weakly collisional plasma. *Mon. Not. Roy. Astron. Soc.* **413**, 7–38.
- ROWAN, M.E., SIRONI, L. & NARAYAN, R. 2019 Electron and proton heating in transrelativistic guide field reconnection. *Astrophys. J.* **873**, 2.
- ROYTERSHEYN, V., BOLDYREV, S., DELZANNO, G.L., CHEN, C.H.K., GROŠELJ, D. & LOUREIRO, N.F. 2019 Numerical study of inertial kinetic-Alfvén turbulence. *Astrophys. J.* **870**, 103.
- ROYTERSHEYN, V. & DELZANNO, G.L. 2018 Spectral approach to plasma kinetic simulations based on hermite decomposition in the velocity space. *Frontiers in Astron. Space Sci.* **5**, 27.
- SCHEKOCHIHIN, A. A. & COWLEY, S. C. 2006 Turbulence, magnetic fields, and plasma physics in clusters of galaxies. *Phys. Plasmas* **13**, 056501.
- SCHEKOCHIHIN, A. A., COWLEY, S. C., DORLAND, W., HAMMETT, G. W., HOWES, G. G., QUATAERT, E. & TATSUNO, T. 2009 Astrophysical gyrokinetics: kinetic and fluid turbulent cascades in magnetized weakly collisional plasmas. *Astrophys. J. Supp.* **182**, 310.
- SCHEKOCHIHIN, A. A., COWLEY, S. C., KULSRUD, R. M., ROSIN, M. S. & HEINEMANN, T. 2008 Nonlinear growth of firehose and mirror fluctuations in astrophysical plasmas. *Phys. Rev. Lett.* **100**, 081301.
- SCHMITZ, H. & GRAUER, R. 2006 Darwin–vlasov simulations of magnetised plasmas. *J. Comput. Phys.* **214**, 738–756.
- SCHWEEN, N.W. & REVILLE, B. 2024 Using spherical harmonics to solve the Boltzmann equation: an operator-based approach. *Mon. Not. Roy. Astron. Soc.* **529**, 1970–1988.
- SCHWEEN, N.W., SCHULZE, F. & REVILLE, B. 2025 Sapphire++: a particle transport code combining a spherical harmonic expansion and the discontinuous galerkin method. *J. Comput. Phys.* **523**, 113690.
- SKOPKE, N., PASCHMANN, G., BAME, S. J., GOSLING, J. T. & RUSSELL, C. T. 1983 Evolution of ion distributions across the nearly perpendicular bow shock - specularly and non-specularly reflected-gyrating ions. *J. Geophys. Res.* **88**, 6121–6136.

- SHARMA, P., HAMMETT, G.W., QUATAERT, E. & STONE, J.M. 2006 Shearing box simulations of the MRI in a collisionless plasma. *Astrophys. J.* **637**, 952.
- SHAY, M. A., DRAKE, J. F., ROGERS, B. N. & DENTON, R. E. 1999 The scaling of collisionless, magnetic reconnection for large systems. *Geophys. Res. Lett.* **26**, 2163–2166.
- SHAY, M. A., HAGGERTY, C. C., PHAN, T. D., DRAKE, J. F., CASSAK, P. A., WU, P., OIEROSET, M., SWISDAK, M. & MALAKIT, K. 2014 Electron heating during magnetic reconnection: a simulation scaling study. *Phys. Plasmas* **21**, 122902.
- SHU, C.-W. 2002 A survey of strong stability preserving high order time discretizations. *Collect. Lect. Preserv. Stab. Under Discret.* **109**, 51–65.
- SHUKLA, A., ROELTGEN, J., KOTSCHENREUTHER, M., JUNO, J., BERNARD, T. N., HAKIM, A., HAMMETT, G. W., HATCH, D. R., MAHAJAN, S. M. & FRANCISQUEZ, M. 2025 Direct comparison of gyrokinetic and fluid scrape-off layer simulations.
- SNYDER, P. B., HAMMETT, G. W. & DORLAND, W. 1997 Landau fluid models of collisionless magnetohydrodynamics. *Phys. Plasmas* **4**, 3974.
- SORASIO, G., MARTI, M., FONSECA, R. & SILVA, L. O. 2006 Very high mach-number electrostatic shocks in collisionless plasmas. *Phys. Rev. Lett.* **96**, 045005.
- SOVINEC, C.R., GLASSER, A.H., GIANAKON, T.A., BARNES, D.C., NEBEL, R.A., KRUGER, S.E., SCHNACK, D.D., PLIMPTON, S.J., TARDITI, A., CHU, M.S. 2004 Nonlinear magnetohydrodynamics with high-order finite elements. *J. Comput. Phys.* **195**, 355.
- SPITZER, L., Jr 1958 The stellarator concept. *Phys. Fluids* **1**, 253–264.
- SQUIRE, J., KUNZ, M. W., ARZAMASSKIY, L., JOHNSTON, Z., QUATAERT, E. & SCHEKOCHIHIN, A. A. 2023 Pressure anisotropy and viscous heating in weakly collisional plasma turbulence. *J. Plasma Phys.* **89**, 905890417.
- SQUIRE, J., QUATAERT, E. & SCHEKOCHIHIN, A. A. 2016 A stringent limit on the amplitude of alfvénic perturbations in high-beta low-collisionality plasmas. *Astrophys. J. Lett.* **830**, L25.
- SQUIRE, J., KUNZ, M. W., QUATAERT, E. & SCHEKOCHIHIN, A. A. 2017a Kinetic simulations of the interruption of large-amplitude shear-alfvén waves in a high- β plasma. *Phys. Rev. Lett.* **119**, 155101.
- SQUIRE, J., SCHEKOCHIHIN, A. A. & QUATAERT, E. 2017b Amplitude limits and nonlinear damping of Shear-Alfvén waves in high-beta low-collisionality plasmas. *New J. Phys.* **19**, 055005.
- SQUIRE, J., SCHEKOCHIHIN, A. A., QUATAERT, E. & KUNZ, M. W. 2019 Magneto-immutable turbulence in weakly collisional plasmas. *J. Plasma Phys.* **85**, 905850114.
- ST-ONGE, D. A., KUNZ, M. W., SQUIRE, J. & SCHEKOCHIHIN, A. A. 2020 Fluctuation dynamo in a weakly collisional plasma. *J. Plasma Phys.* **86**, 905860503.
- STONE, J.M., TOMIDA, K., WHITE, C.J. & FELKER, K.G. 2020 The athena++ adaptive mesh refinement framework: design and magnetohydrodynamic solvers. *Astrophys. J. Supp.* **249**, 4.
- SWISDAK, M., DRAKE, J. F., SHAY, M. A. & MCILHARGEY, J. G. 2005 Transition from antiparallel to component magnetic reconnection. *J. Geophys. Res.* **110**.
- TATSUNO, T., DORLAND, W., SCHEKOCHIHIN, A. A., PLUNK, G. G., BARNES, M., COWLEY, S. C. & HOWES, G. G. 2009 Nonlinear phase mixing and phase-space cascade of entropy in gyrokinetic plasma turbulence. *Phys. Rev. Lett.* **103**, 015003.
- TENBARGE, J. M., DAUGHTON, W., KARIMABADI, H., HOWES, G. G. & DORLAND, W. 2014 Collisionless reconnection in the large guide field regime: gyrokinetic versus particle-in-cell simulations. *Phys. Plasmas* **21**, 020708.
- TENBARGE, J. M., NG, J., JUNO, J., WANG, L., HAKIM, A. H. & BHATTACHARJEE, A. 2019 An extended mhd study of the 16 October 2015 mms diffusion region crossing. *J. Geophys. Res.* **124**, 8474–8487.
- THORNE, K.S. & BLANFORD, R.D. 2017 *Modern Classical Physics*. Princeton University Press.
- TRENT, T., CHRISTIAN, P., CHAN, C.-KWAN, PSALTIS, D. & ÖZEL, F. 2023 A new covariant formalism for kinetic plasma simulations in curved spacetimes. *Astrophys. J. Lett.* **959**, L6.
- TRENT, T., ROLEY, K., GOLDEN, M., PSALTIS, D. & ÖZEL, F. 2024 Covariant guiding center equations for charged particle motions in general relativistic spacetimes.
- TUMLINSON, J., PEEPLES, M.S. & WERK, J.K. 2017 The circumgalactic medium. *Ann. Rev. Astron. Astrophys.* **55**, 389–432.

- VANDERVOORT, P.O. 1960 The relativistic motion of a charged particle in an inhomogeneous electromagnetic field. *Ann. Phys.* **10**, 401–453.
- VASYLIUNAS, V.M. 1975 Theoretical models of magnetic field line merging. *Rev. Geophys.* **13**, 303–336.
- VEGA, C., ROYTERTSHTYEN, V., DELZANNO, G.L. & BOLDYREV, S. 2023 Electron-scale current sheets and energy dissipation in 3D kinetic-scale plasma turbulence with low electron beta. *Mon. Not. Roy. Astron. Soc.* **524**, 1343–1351.
- VENCELS, J., DELZANNO, G.L., MANZINI, G., MARKIDIS, S., PENG, I.B. & V., ROYTERTSHTYEN SpectralPlasmaSolver: a spectral code for multiscale simulations of collisionless, magnetized plasmas. *J. Phys. Confer. Ser.* **719**, 012022.
- WALTERS, J., KLEIN, K.G., LICHKO, E., JUNO, J. & TENBARGE, J.M. 2024 Electron influence on the parallel proton firehose instability in 10-moment, multifluid simulations. *Astrophys. J.* **975**, 290.
- WANG, L., HAKIM, A. H., BHATTACHARJEE, A. & GERMASCHEWSKI, K. 2015 Comparison of multi-fluid moment models with particle-in-cell simulations of collisionless magnetic reconnection. *Phys. Plasmas* **22**, 012108.
- WANG, L., HAKIM, A. H., NG, J., DONG, C. & GERMASCHEWSKI, K. 2020 Exact and locally implicit source term solvers for multifluid-Maxwell systems. *J. Comput. Phys.* **415**, 109510.
- WANG, L., GERMASCHEWSKI, K., HAKIM, A., DONG, C., RAEDER, J. & BHATTACHARJEE, A. 2018 Electron physics in 3d two-fluid ten-moment modeling of Ganymede's magnetosphere. *J. Geophys. Res.*
- WESSON, J. 2011 *Tokamaks*. Oxford University Press.
- ZOCCO, A., LOUREIRO, N. F., DICKINSON, D., NUMATA, R. & ROACH, C. M. 2015 Kinetic microtearing modes and reconnecting modes in strongly magnetised slab plasmas. *Plasma Phys. Control. Fusion* **57**, 065008.
- ZOCCO, A. & SCHEKOCHIHIN, A.A. 2011 Reduced fluid-kinetic equations for low-frequency dynamics, magnetic reconnection, and electron heating in low-beta plasmas. *Phys. Plasmas* **18**, 102309.